Università degli Studi Di Napoli Federico II

Scuola Politecnica e delle Scienze di Base

Dipartimento di Ingegneria Industriale

Tesi di Dottorato in Ingegneria Aerospaziale, Navale

e della Qualità

KRISTINA: Kinematic RIb based STructural system for INnovative Adaptive trailing edges

RELATORI

CANDIDATO:

Ch.mo Prof. Leonardo Lecce

Magnifico Marco

Ch.mo Prof. Rosario Pecora

Ch-mo Prof. Francesco Amoroso

Page left intentionally blank

Table of Contents

Acronyms:

1D	One-dimensional
2D	Bi-dimensional
3D	Three-dimensional
A/C	Aircraft
$A_{eq(f)/(r)}$	Front/rear spar equivalent areas
AIC	Aerodynamic Influence Coefficients
(A)TE	(Adaptive) Trailing Edge
b	number of blocks
B_i	i-th block (of the rib)
$BM_{i(f)} / BM_{i(r)}$	Amount of $BM_{i(U)}$ absorbed by (front/rear) spar caps
$BM_{i(U)}$	Ultimate bending moment at S_i
c (/c*)	wing chord (/trailing edge chord)
CAD	Computer aided drawing
C_D	Drag coefficient
CFD	Computational fluid dynamics
C_L	Lift coefficient
CONM2	Lumped mass element (see MSC-NASTRAN® user manual)
C_P	Pressure coefficient
D	Drag
DLM	Doublet Lattice Method
DMIG	Direct Input Matrix Generalized (see MSC-NASTRAN® user manual)
dof(s)	Degree(s) of freedom
E_{SMA}	SMA element (equivalent) Young Modulus
F	Force
FE (/FEM)	Finite elements (/Finite elements method)
g	Mechanism kernel function
GRS	Global Reference System
GVT	Ground Vibration Test
$h_{i(f)} / h_{i(r)}$	Height of (front / rear) spar web at S_i
K	Active degrees of freedom of a kinematic chain
l	number of links
L	Lift
$l_{i(sk)}$	Chordwise length of the (upper/lower) skin panel at S_i
LE	Leading Edge
LH	Left Hand
MAC	Mean Aerodynamic Chord

$\mathbf{MRF}$	Magneto-rheological fluids
$\mathbf{P_i}$	Perimeter of the box cell at S_i
$\mathbf{q_i}$	Cell's shear flow at S_i
$\mathbf{q_{i(fw)/(rw)/(sk)}}$	Shear flow along the front spar web / rear spar web / skin panels at S_i
$\mathbf{RBE2}$	Rigid Body Element (see MSC-NASTRAN® user manual)
$\mathbf{RH}$	Right Hand
$\mathbf{S_i}$	i-th cross section (of the trailing edge box)
$\mathbf{S_{i(U)}}$	Ultimate shear at S_i
$\mathbf{SRS}$	(trailing edge) Section reference system
$\mathbf{t_{i(fw)/(rw)/(sk)}}$	Thickness of the front spar web / rear spar web / skin panels at S_i
$\mathbf{TM_{i(U)}}$	Ultimate torque at S_i
$\mathbf{TRL}$	Technology readiness level
$\mathbf{Xsc_i}$	Chordwise position of the shear center at S_i
$\mathbf{\Gamma}$	Iteration function
$\mathbf{\Omega_i}$	Area enclosed by the box cell at S_i
$\mathbf{\sigma_{ref}}$	Allowable stress (in tension or compression)
$\mathbf{\sigma_{tU}}$	Failure stress in tension or compression
$\mathbf{\tau_{ref}}$	Allowable stress (in shear)

FOREWORD

"About 3 billion people every year use air transports to realize their business and leisure needs, whereas about 5 trillion Euros worth of goods are transported by air. And these figures are on the rise: Annual passengers are expected to reach over 6 billion by 2030, according to current projections. As the number of flights increases, pollution and noise from air travel impose significant challenges on the industry. This is why airlines, aircraft manufacturers, and researchers are constantly searching for new ways to make their planes lighter, with increased aerodynamic performance, achieving at the same time greater fuel efficiency and thereby reduce the environmental footprint of air travel.

Coordinated by Airbus, the Smart Intelligent Aircraft Structures (SARISTU) project brought together 64 partners from 16 countries with a common goal: to demonstrate the feasibility of reducing aircraft weight and operational costs, as well as improving the flight profile-specific aerodynamic performance. During the four years of project implementation (September 2011–August 2015), the synergy of leading entities participating in this ambitious venture has succeeded to achieve some major breakthroughs in a number of technological fields.

Firstly, developments with respect to conformal morphing, in other words the gap- and kink-less change of the shape of aerodynamic surfaces, validated not only a suitable skin material, but even the ability to integrate additional functionalities such as heating and environmental protection. Furthermore, the technical feasibility of <u>trailing edge morphing</u> and the ability to consider active winglet control were investigated.

Secondly, developments in the wide area of structural health monitoring covered analysis methods, physical system integration at part manufacturing level, the combination of different measurement and analysis techniques on single areas of the aircraft, and a screening program for fundamental approaches to passive damage indicating surfaces.

Thirdly, multi-functional structure developments highlighted the ability to upscale nanocomposite improvements from the basic resin all the way up to industrially relevant laminates of complex and large geometries, as well as opening development routes to further improvement. This also includes electrically conductive nanocomposites and the investigation of possibilities for metallic co-bonding. Finally, these technologies have been verified at assembly level on major demonstrators.

All in all, SARISTU represents a major step forward in successfully integrating smart intelligent structural concepts into traditional aircraft design and reflects the potential of nanotechnology in aircraft manufacturing applications. Furthermore, the project has shown that incremental improvements taken together can lead to significant weight and operational cost reductions and lead to improved aerodynamic performance.[1]"

---

[1] *(SARISTU - Smart Intelligent Aircraft Structures, editors P.C. Woelcken,M. Papadopoulos, Springer International Publishing AG, Switzerland, 2015).*

CHAPTER 1

Sizing of the ATE

The design process of the adaptive trailing edge (ATED) addressed by SARISTU is here outlined, from the conceptual definition of the camber-morphing architecture up to the assessment of the device executive layout. Rational design criteria were implemented in order to preliminarily define ATED structural layout and the general configuration of the embedded mechanisms enabling morphing under the action of aerodynamic loads. Aeroelastic stability issues were duly taken in account in order to safely assess inertial and stiffness distributions of the primary structure as well as to provide requirements for the actuation systems harmonics. Advanced FE analyses were then carried out and the robustness of adopted structural arrangements was proven in compliance with applicable airworthiness requirements.

1.1 ADAPTIVE TRAILING EDGE: SCOPE AND REFERENCE GEOMETRIES

The adaptive trailing edge device (ATE) is aimed at maximizing wing aerodynamic performance in cruise condition with the ultimate goal of a 3% reduction in fuel consumption.

By properly morphing specific trailing edge regions, the wing shape is controlled during cruise in order to compensate the weight reduction due to the fuel burning, thus allowing the trimmed configuration to remain optimal in terms of efficiency (L/D ratio) or minimal drag (D).

Parametric aerodynamic studies were carried out to evaluate the optimal dimensions and locations of trailing edge portions interested by morphing as well as the target morphed shapes to be implemented.

The optimized geometry of ATE device resulted characterized by two regions (Fig. 1):

- **inboard ATE**,   untapered, chordwise extension: 0.35 m, spanwise extension: 3.0 m;
- **outboard ATE**, untapered, chordwise extension: 0.35 m, spanwise extension: 7.3 m.
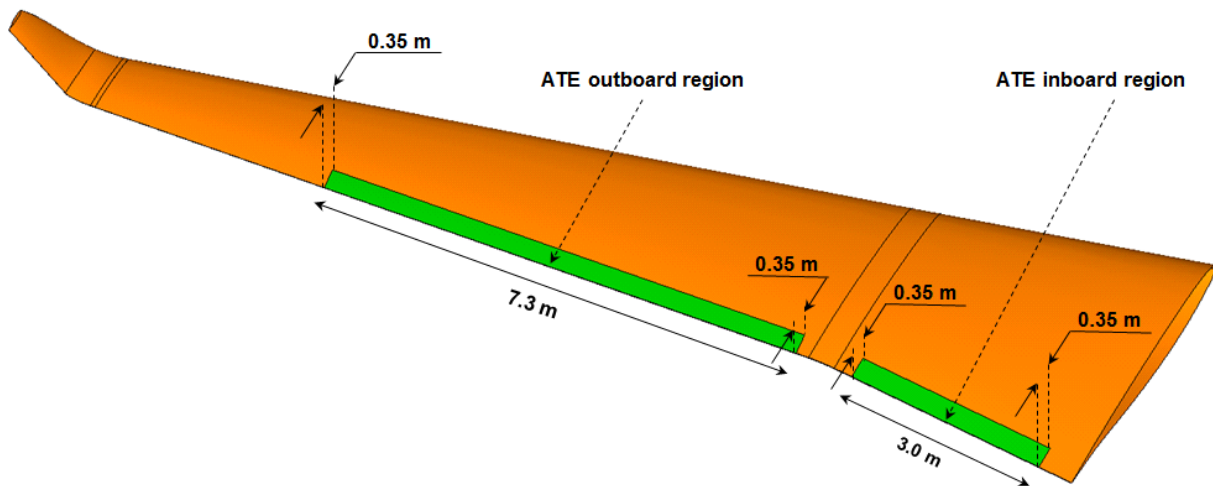

Fig. 1: ATE regions (LH wing).

The cutting plane defining the root section of the inboard (/outboard) region was chosen to be perpendicular to the wing trailing edge line at a distance of 2.28 m (/6.22 m) from the XZ plane of the global reference system (GRS) defined as follows (Fig. 2):

- Origin (O) at the intersection point between wing leading edge and A/C symmetry plane (π);
- *X* axis passing through the intersection point (P) between A/C symmetry plane and wing trailing edge line, oriented from O to P;
- *Y* axis perpendicular to the A/C symmetry plane and oriented towards the RH wing tip;
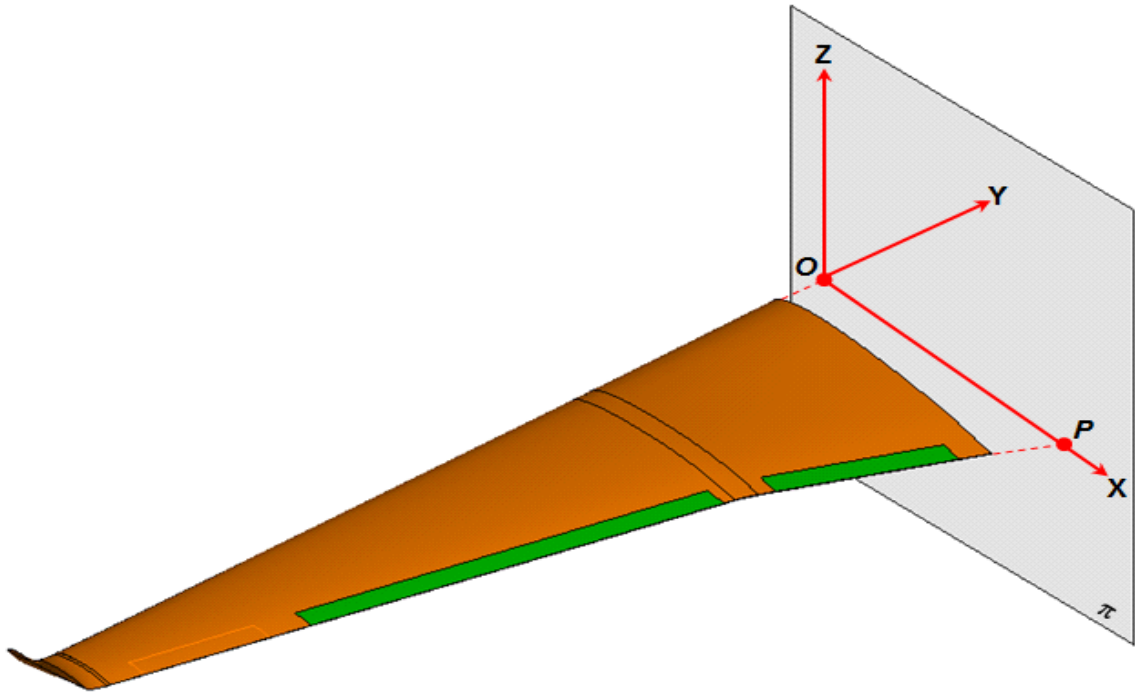- *Z* axis perpendicular to XY plane and upwards oriented.

Fig. 2: LH wing and Global Reference System (GRS)

Target morphed shapes for ATE cross sections were determined under the following constraints:

- Airfoil thickness distribution unaffected by morphing;

- Maximum allowed skin deformation equal to 2%;

- Airfoil camber morphing such that the airfoil tip is forced to rotate, by an angle β, around a virtual hinge located on airfoil camber line at the most forward chordwise position (Fig. 3).
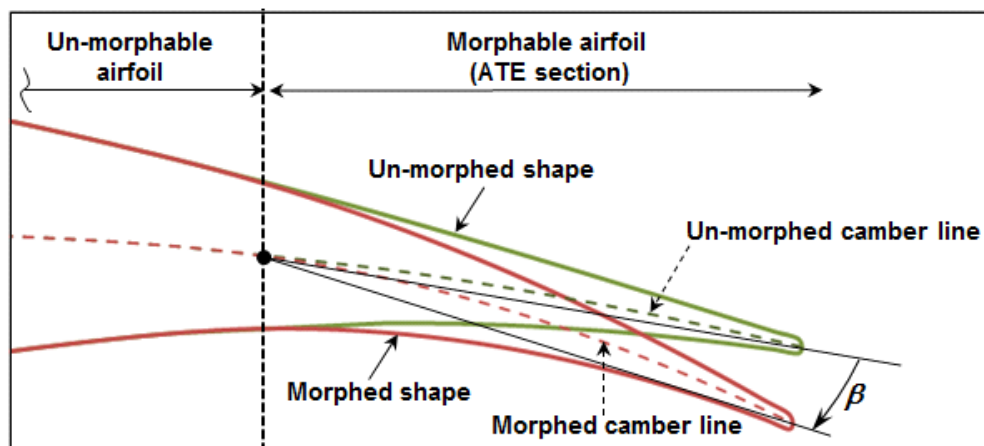

Fig. 3: ATE generic section, un-morphed and morphed shapes

Optimal values of β angle were found to be included in the range [-5°:+5°], where negative values indicates upwards morphing. In other terms, the aerodynamic efficiency of the wing was proved to be optimized during cruise, if each ATE section is enabled to change its shape in compliance with target tip deflections ranging from -5° up to +5°.

Limit target shapes for the cross sections bounding ATE regions have been plotted in Fig. 5 - Fig. 8, referring to local coordinate systems defined as follows (Fig. 4) :

- *xz* plane perpendicular to the trailing edge line and containing the generic ATE section;
- origin (o) at the intersection between *xz* plane and wing leading edge;
- *x* axis collinear to the chord of the un-morphed wing section;
- *y* axis perpendicular to *xz* plane and oriented towards the RH wing;
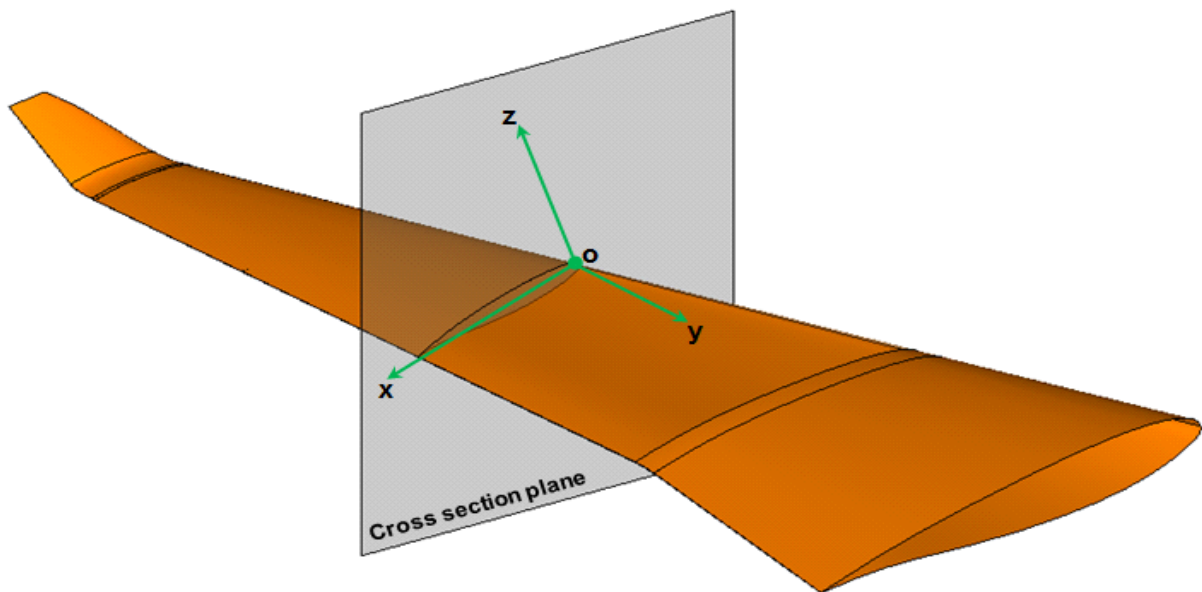- *z* axis upwards oriented.

Fig. 4: wing and local section reference system (SRS)

The above defined reference systems will be indicated as SRS, where the acronym SRS stands for *Section Reference System*. The chord of the (un-morphed) wing section individuated by the *xz* plane of the generic SRS will be denoted with c*.
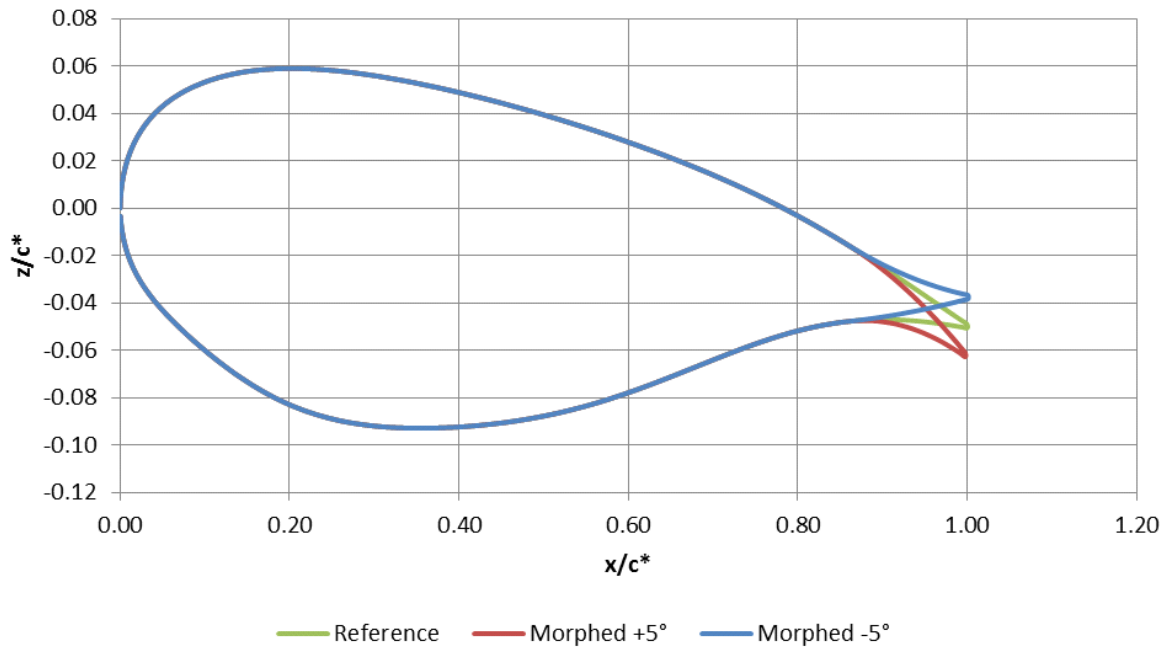
4

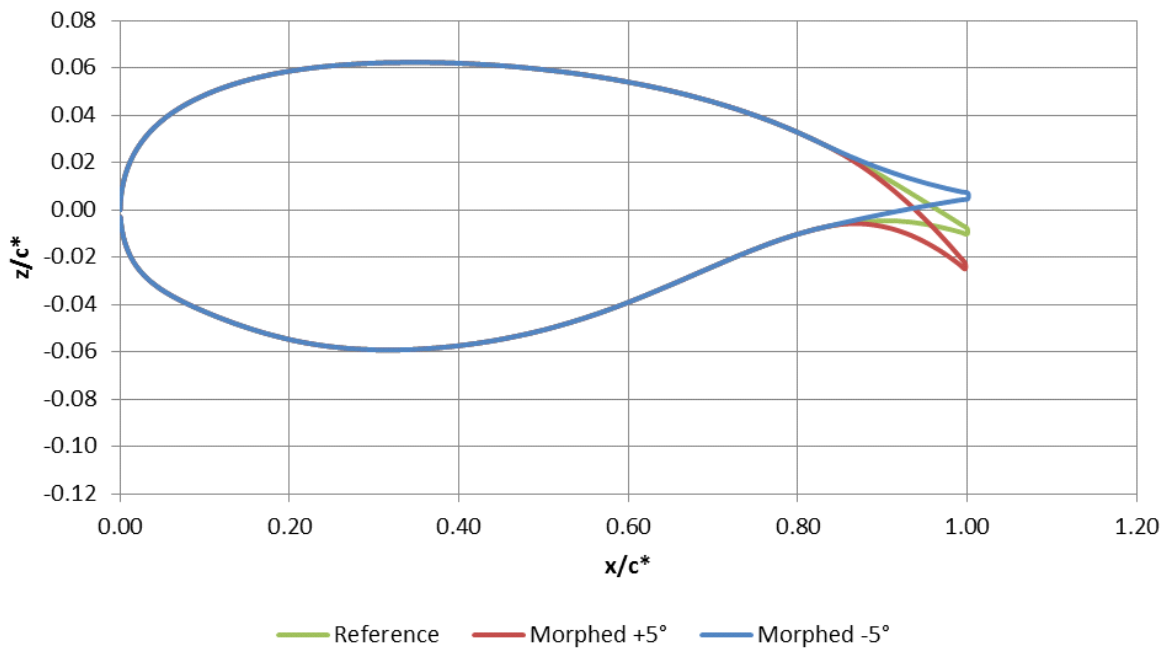**Fig. 5: Inboard ATE, root section – reference and limit target shapes**

Fig. 6: Inboard ATE, tip section – reference and limit target shapes

5
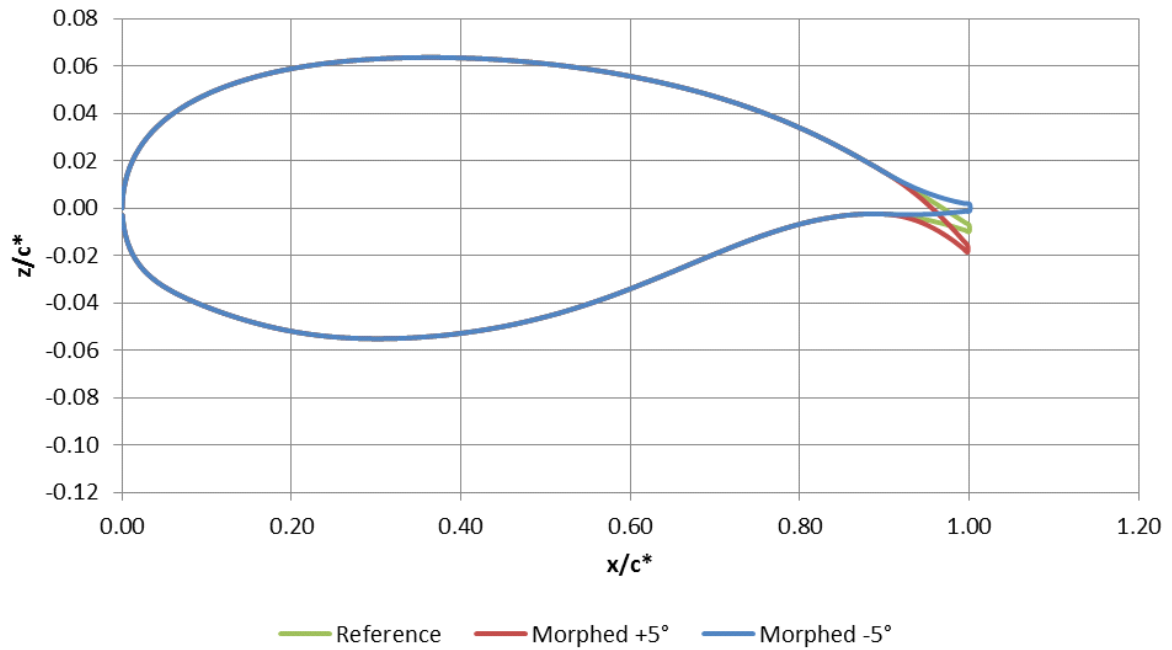
Fig. 7: Outboard ATE, root section – reference and limit target shapes
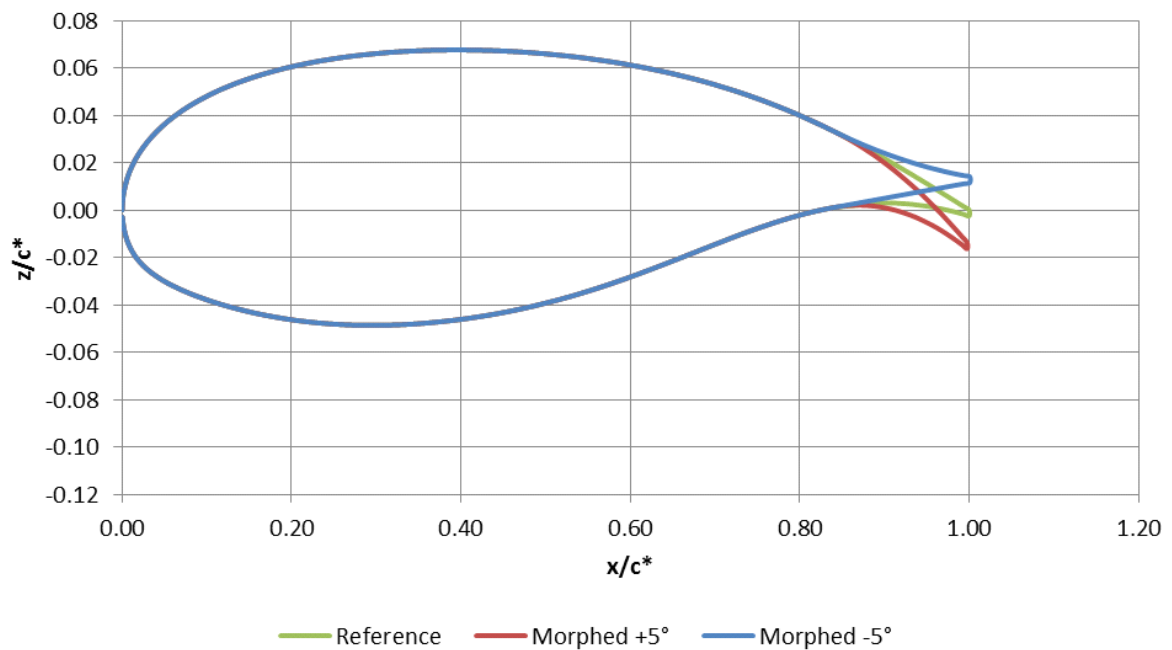
Fig. 8: Outboard ATE, tip section – reference and limit target shapes

1.2   THE MORPHING RIB CONCEPT

In order to enable the transition of the ATE sections from the reference (baseline) shape to the target limit ones, a morphing structural concept was developed for ATE ribs.

Each rib (Fig. 9) was assumed to be segmented into four consecutive blocks (B0,B1,B2,B4) connected to each other by means of hinges located on the airfoil camber line (A,B,C). Block B0 is rigidly connected to the

rest of the wing structure, while all the other blocks are free to rotate around the hinges on the camber line, thus physically turning the camber line into an articulated chain of consecutive segments. Rod elements (L1, L2) -hinged on not adjacent blocks- force the camber line segments to rotate according to specific gear ratios.

Linking rod elements make each rib equivalent to a single-DOF mechanism: if the rotation of any of the blocks is prevented, no change in shape can be obtained; on the other hand, if an actuator moves any of the blocks, all the other blocks follow the movement accordingly.
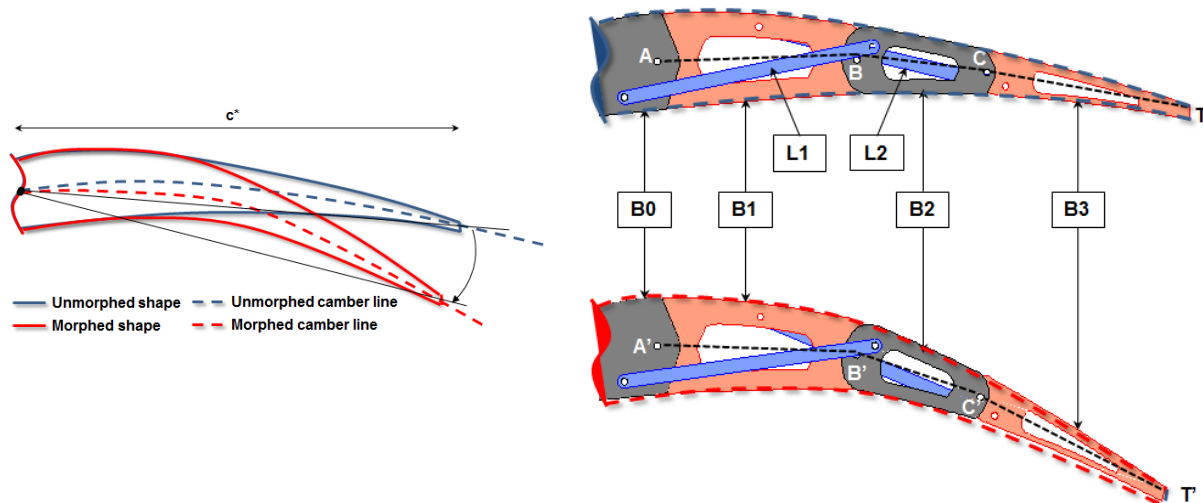

Fig. 9: Morphing rib segmentation

The introduced segmentation turns the airfoil camber line into an articulated polygonal line which can assume different shapes depending on the relative rotation between adjacent blocks. The number of blocks and their chordwise extension are commonly defined in order to satisfactorily match the camber line in both baseline and morphed configurations while lowering the structural complexity as much as possible. A big number of small blocks surely assure more accurate reproduction of un-morphed/morphed camber lines; on the other hand it may bring to considerable impacts on the feasibility of the structural arrangement as well as on its manufacturing and maintenance costs (high number of parts). Conversely a small number of large blocks leads to very simple structural layout but may result inadequate to enable morphing in compliance with high-fidelity shape reproduction requirements. To make a parallel, the issue is the same occurring when defining the mesh size in a given structural problem; refined meshes may produce accurate results but need for more computational time while coarse meshes speed up the analysis run but may prohibitively decrease the quality of the analysis outcomes.

The right solution stays in properly balancing needs and requirements in order to come out with an optimal compromise which works well for the specific problem to be addressed.

In our specific case, the process leading to the optimal number and size of blocks is referred as ***shape transition analysis***. Basically an iterative analysis is carried out involving aerodynamic computations at each loop. A first

trial is made on block number and length: in automated algorithms this action may be easily performed referring to a configuration vector $\underline{C}$ =[c_1,c_2,..,c_b] whose size, *b*, represents the number of blocks and whose generic component c_i stands for the chordwise extension of the i-th block.

For each component c_i a specific range R_i is defined coherently to structural constraints and feasibility considerations. A starting value $\underline{C_0}$ is assumed for $\underline{C}$ in compliance with the above mentioned ranges.

Morphed airfoil shape is then re-built by considering the polygonal line defined by $\underline{C_0}$ and aerodynamic analysis is carried out to evaluate the degradation (γ) of the target performance due to the adoption of the trial segmented solution; such degradation can be measured for instance as the difference between the C_L, C_D or C_L/C_D of the target morphed shape and those related to the airfoil shape approximated by $\underline{C_0}$. A new set of components is then assumed for $\underline{C}$ and the process is repeated until all ranges R_i are fully mapped. Optimal configuration vector is then obtained as the one minimizing the function $\gamma = \gamma(c_1,c_2,..,c_b)$ over the variable ranges $R_1,R_2,.., R_b$.

The shape transition analysis gives as a direct result the position of camber lines hinges and, as indirect result, the amount of rotation required to each camber line segment to suitably fit the target morphed shape.

Let us now assume that the outcomes of the analysis are those sketched in Fig. 9, in terms of number of blocks and hinges positions along camber line in both un-morphed (A,B,C) and morphed (A', B', C) configurations. The indirect results are represented by the rotations that the segments AB, BC, CT, have to make around A, B, C to turn the polygonal line ABCT into A'B'C'T'.

In order to physically implement these rotations, further linkages between not-adjacent blocks are clearly necessary[2]. The number of additional links (*l*) is defined on the basis of the active degrees of freedom to be assigned to the rib mechanism; if *K* denotes the active dofs of the rib mechanism, it results:

$$K = b - (l+1) \tag{1}$$

where *b* is the number of rib bocks.

Since the rib has to be at least intrinsically isostatic, *K* is equal to the number of actuators that should be installed to suppress (and control) the active degrees of freedom of the mechanism.

In the example of Fig. 9, *l* is equal to 2, *b* is equal to 4 and the mechanism has clearly one single degree of freedom.

Linking rod L1 and L2 hinged to not-adjacent blocks, force the camber line segments to rotate according to specific gear ratios; if the rotation of any of the blocks is prevented, no change in shape can be obtained; on the other hand, if one single actuator moves any of the blocks, all the other blocks follow the movement according to the above mentioned gear ratios.

The position of the linking rod hinges is finally determined on the base of the specific rotation each segment has to perform to enable the transition from the baseline to the target morphed shape. The indirect results of the

---

[2] Linkages cannot be placed between adjacent blocks since they would prevent their relative rotation and therefore disable the shape transition.

shape transition analysis feed therefore the process finalized to the definition of the linking elements hinges; this process is here referred as **_mechanization of the kinematic chain_** and involves the solution of an *inverse kinematic* problem.

The positions of the hinges along the camber line (both in un-morphed and morphed configurations) are the input data of the problem, the positions of the links are the unknown variables to be determined.

Let's always recall the example case of Fig. 9 to better explain how the problem can be solved.

Since the position of each link is univocally determined in a generic section reference system (SRS) by the coordinates of its tip hinges, the number of unknown variables is equal to 8 (2 links and 2 coordinates for each tip hinge). Referring to the equivalent representation of the rib mechanism reported in Fig. 10 and to the symbols therein adopted, the mathematical formulation of the problem consists in finding the vector $\vec{v}$ (=[$x_{L1\text{-}1}$, $z_{L1\text{-}1}$, $x_{L1\text{-}2}$, $z_{L1\text{-}2}$, $x_{L2\text{-}1}$, $z_{L2\text{-}1}$, $x_{L2\text{-}2}$, $z_{L2\text{-}2}$]) defined over the domain $\mathcal{D}$ and satisfying the equation:

$$\vec{w}_m = g(\vec{w}, \vec{v}) \qquad\qquad (2)$$

where:

$\mathcal{D}$ is the region delimited by the un-morphed airfoil ;

$\vec{w}$ = [x_A, z_A, x_B, z_B, x_C, z_C, x_T, z_T], is the vector defining the positions (in SRS) of the hinges A,B,C and of the airfoil tip point (T) in un-morphed configuration;

$\vec{w}_m$ = [x_A', z_A', x_B', z_B', x_C', z_C', x_T', z_T'], is the vector defining the positions (in SRS) of the hinges A,B,C and of the airfoil tip point in morphed configuration;

$\vec{w}_d$ = [x_A'', z_A'', x_B'', z_B'', x_C'', z_C'', x_T'', z_T''], is the vector defining the positions (in the SRS) of the hinges A,B,C and of the airfoil tip point in downwards-morphed configuration;

g Is the mechanism *kernel functions*, governing morphing kinematics. Such function is generally non-linear and not-invertible with respect to the variable $\vec{v}$.
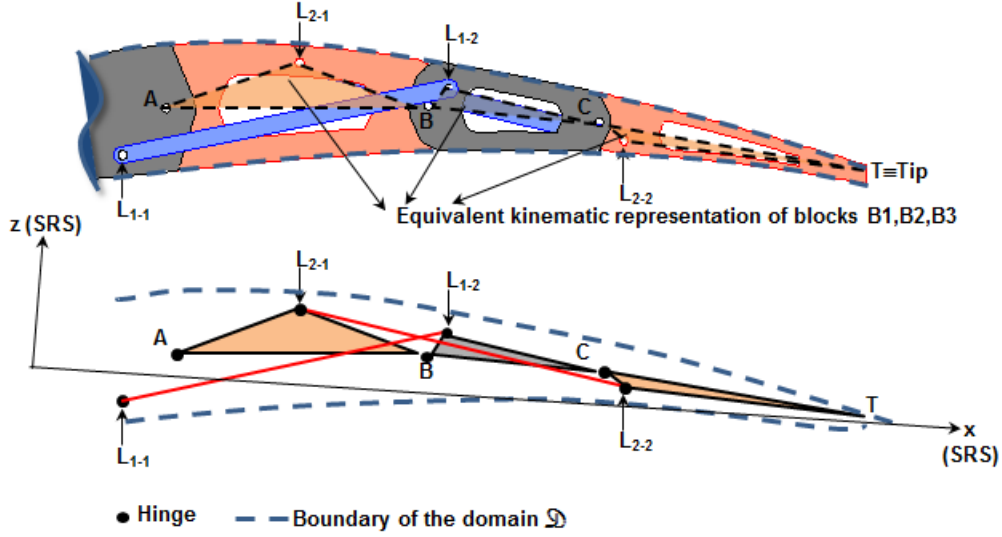
Fig. 10: Mechanization of the kinematic chain

The space of the solutions of (2) can be found through a methodology consisting of three main steps.

Step 1. _Forced reduction of the unknown variables_

The positions of the hinges L_{1-2} and L_{2-2} are arbitrarily imposed in the domain $\mathcal{D}$. The unknown vector $\vec{v}$ is then replaced by the following summation:

$$\vec{v} = \vec{v}_1^* + \vec{v}_2^* + \vec{t} \qquad (3)$$

where:

$\vec{t}$ $= [0,0,x_{L1-2},z_{L1-2},0,0,x_{L2-2},z_{L2-2}]$ is the vector defining the (imposed) positions of the hinges L_{1-2} and L_{2-2};

$\vec{v}_1^*$ $= [x_{L1-1},z_{L1-1},0,0,0,0,0,0]$ is the vector defining the unknown position of the hinges L_{1-1};

$\vec{v}_2^*$ $= [0,0,0,0,x_{L2-1},z_{L2-1},0,0]$ is the vector defining the unknown position of the hinge L_{2-1}.

Step 2. _Solution of the linearized morphing equations_

In force of (3), the equations governing the morphing kinematics changes into:

$$\vec{w}_m = g(\vec{w},\vec{t}) + g^*(\vec{v}_1^*) + g^*(\vec{v}_2^*) \qquad (4)$$

where the kernel functions result decomposed into a non-linear and not-invertible part depending on variables $\vec{w},\vec{t}$ and into a linear and invertible part (marked with the apex "*") depending on variables $\vec{v}_1^*$ and $\vec{v}_2^*$. Since the terms, $\vec{w}_m$ and $g(\vec{w},\vec{t})$ are all known vectors defined in $\Re^8$, the equation (4) may be algebraically solved to determine the unknowns $\vec{v}_1^*$ and $\vec{v}_2^*$.

Step 3. _Iteration_

10

A new value for $\vec{t}$ is imposed, and step 1,2 are repeated.

The iteration may be conceptually regarded as a function Γ operating on the variable $\vec{t}$ (coordinates of hinges L_{1-2} and L_{2-2}) and providing as output the vectors $\vec{v}_1^*$ and $\vec{v}_2^*$ (coordinates of hinges L_{1-1} and L_{2-1}):

$$\Gamma: \forall \, \vec{t} \in D \subset \mathfrak{R}^8 \longrightarrow (\vec{v}_1^*, \vec{v}_2^*) = \Gamma(\vec{t}) \in D \subset \mathfrak{R}^8 \qquad (5)$$

The function Γ (i.e. the iteration of the first two steps) allows for the evaluation of the locus described by the hinges L_{1-1} and L_{2-1} while the positions of the hinges L_{1-2} and L_{2-2} range in the domain of the airfoil section.

A graphical representation of the hinges' locus obtained for the TE section of Fig. 9, has been reported (as explanatory example) in Fig. 11.
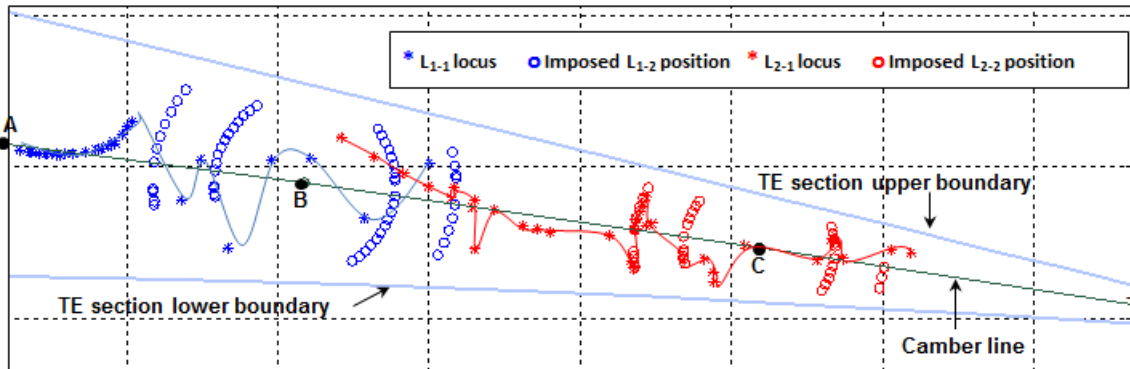

Fig. 11: Hinge locus

In order to find the best position of hinges L_{1-1}, L_{1-2}, L_{2-1}, L_{2-2}, practical considerations, addressing the feasibility of the mechanism, are *translated* into an automatic selection algorithm implemented on suitable software tools. More in detail, two *control parameters* are defined for each hinge: the distance h from the camber line, the distance k from the closest airfoil boundary (either upper or lower).

The best position of hinges L_{1-1}, L_{1-2}, L_{2-1}, L_{2-2}, is then evaluated by selecting among all vectors $\vec{v}_1^*, \vec{v}_2^*, \vec{t}$ satisfying the relation $(\vec{v}_1^*, \vec{v}_2^*) = \Gamma(\vec{t})$, the ones whose components maximize the values of the control parameters h an k.

In other terms, the best position of the hinges is considered to be the one assuring the:

- highest clearance from the camber line, thus avoiding dangerous alignment between links L1,L2 and camber line hinges (potentially resulting in a bi-stable mechanism);
- highest clearance from the airfoil boundary, thus avoiding interference problems between the physical hinges and the skin panels.
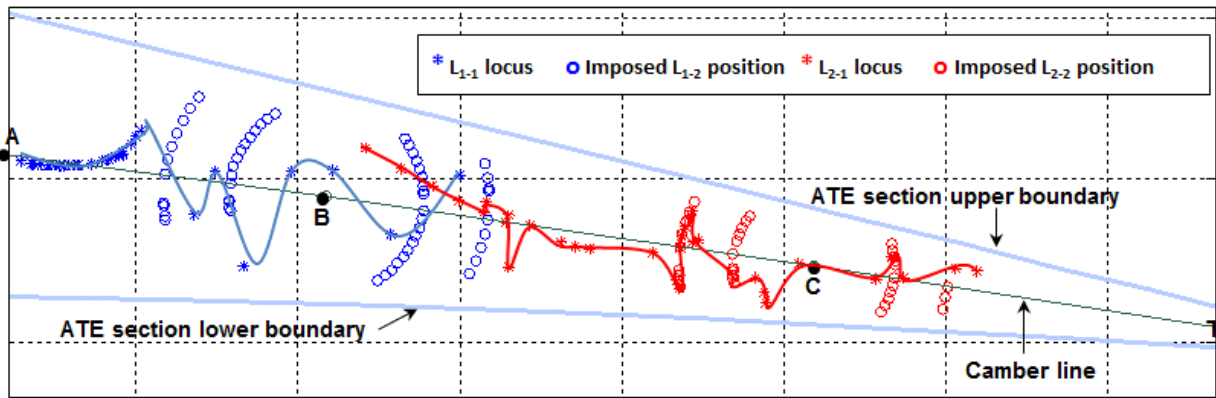
Fig. 12: Outboard ATE tip section, hinges locus

The hinges position pertaining to the root and tip sections of ATE regions, and resulting from the above described selection algorithm, have been reported in Fig. 13 - Fig. 16.
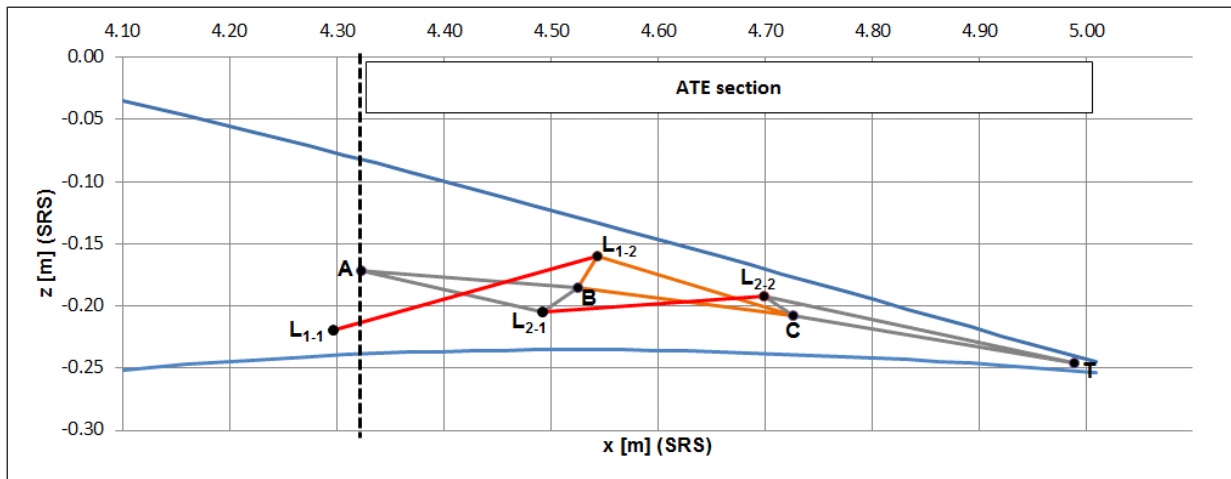

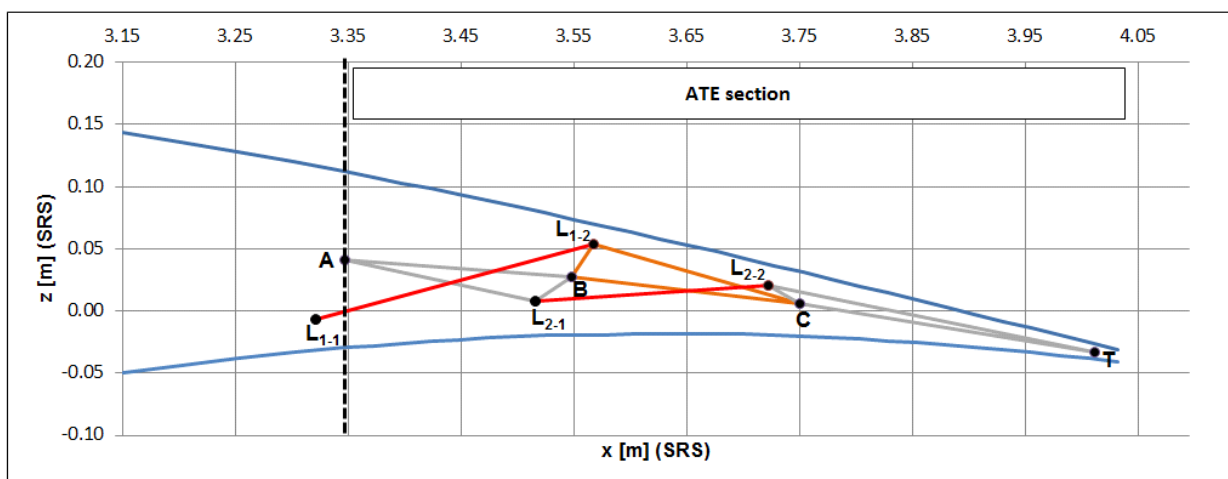**Fig. 13: Inboard ATE root section, equivalent scheme of rib mechanism**

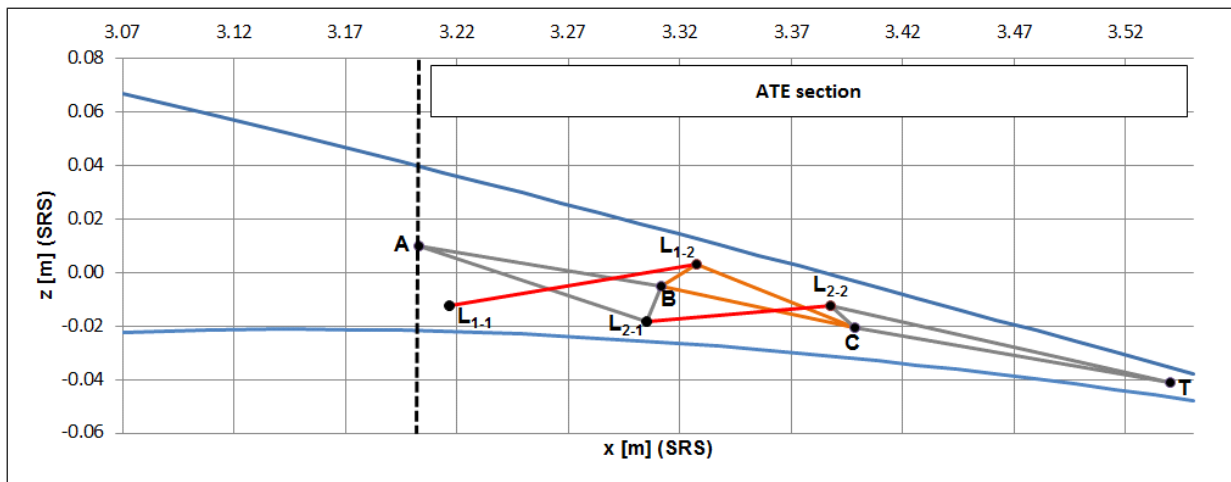**Fig. 14: Inboard ATE tip section, equivalent scheme of rib mechanism**

Fig. 15: Outboard ATE root section, equivalent scheme of rib mechanism
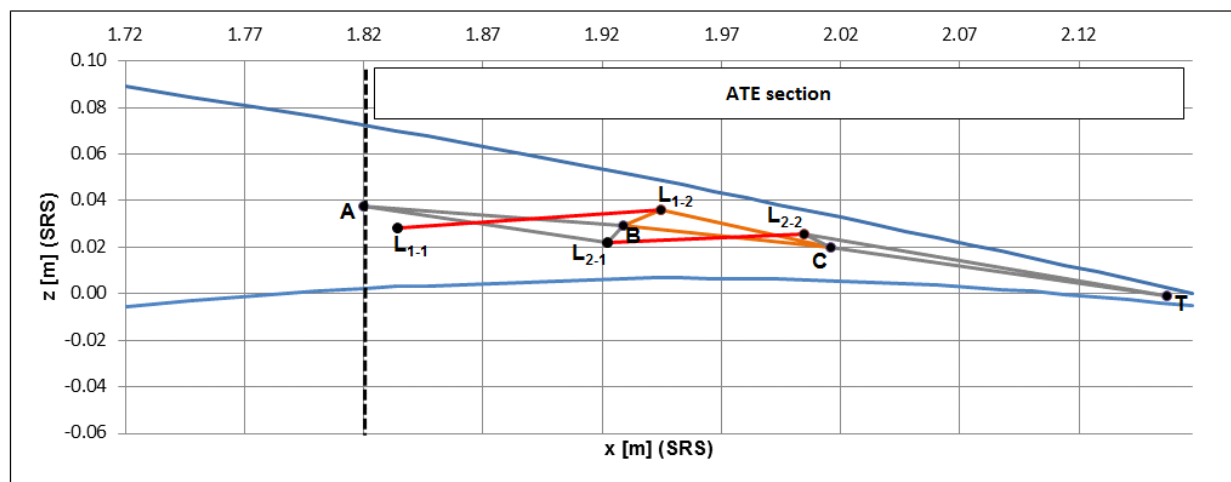

Fig. 16: Outboard ATE tip section, equivalent scheme of rib mechanism

1.3 DEFINITION OF THE MORPHING BOX KINEMATICS

According to the procedure described in the previous paragraph, the kinematics of the rib mechanism was defined in order to exactly match the target morphed camber lines at each section delimiting the ATE regions. As a consequence of this, the ribs blocks were assumed to be connected through hinges located on airfoil camber line (A,B,C, Fig. 13 - Fig. 16) and links properly positioned to *drive* the camber line to its morphed shapes upon the actuation of the mechanism. The definition of the ribs kinematics was moreover carried out section by section, thus considering each rib as an independent mechanism designed with the sole purpose to enable the shape transition of the section from its baseline configuration to the target morphed ones.

In other terms, the joints of the mechanisms (hinges and links) were assessed to assure the full compliance with the required morphed shapes at each investigated ATE section; on the other hand such *full compliance* inevitably resulted in two main drawbacks when ribs mechanism were regarded as spanwise connected parts of a morphing box assembly:

- *misalignment of spanwise hinge lines*: due to the specific geometry of the wing trailing edge, the lines connecting homologues hinges of different ATE sections resulted not perpendicular to the sections planes and (therefore) not parallel to the trailing edge line; the spanwise connection of two different sections (necessary to assure adequate bending and torsion stiffness to the box assembly) forced the blocks of the sections to rotate around oblique axes with dramatic impacts on the design of hinges and on the overall box kinematics;

- *differential actuation of the mechanisms*: two different sections of the ATE resulted characterized by different mechanisms due to the change of the spatial location of hinges and links from one section to another. Different mechanisms along the span required different displacements fields to move each mechanism thus increasing the level of complexity of the actuation and control systems of the entire box.

Higher priority was then given to the simplicity of the morphing box assembly rather than the full compliance of ribs mechanisms with the target morphed shapes at each ATE section.

For each cross section of the ATE outboard (/inboard) region, the hinges of the rib mechanism were repositioned according to the criteria listed below:

- the hinges of the section *S** located at the semi-span of ATE outboard (/inboard) region were defined according to the methodology described in the previous paragraph;

- at the generic cross section S_i, the hinges of the mechanism were obtained by projecting the hinges of S* onto S_i plane.

The application of such criteria led to:

- equal mechanism at different spanwise stations;

- hinge lines perpendicular to the rib planes and parallel to the trailing edge line;

- fully compliance of the mechanism with target morphed shapes along the middle section of ATE outboard (/inboard) region;

- slight (and negligible) deviation of attainable morphed camber lines with respect to the target ones all along the other cross sections.

1.4 STRUCTURAL SIZING OF THE MORPHING BOX

The ribs' kinematic was transferred to the overall trailing edge structure by means of a multi-box arrangement. Each box of the structural arrangement was assumed to be characterized by a *single-cell* configuration delimited along the span by homologue blocks of consecutive ribs, and along the chord by longitudinal stiffening elements (spars).

An equivalent static scheme -based on lumped elastic properties- was considered for each box; such scheme is sketched in Fig. 17 with reference to a generic bay delimited by two consecutive ATE ribs.
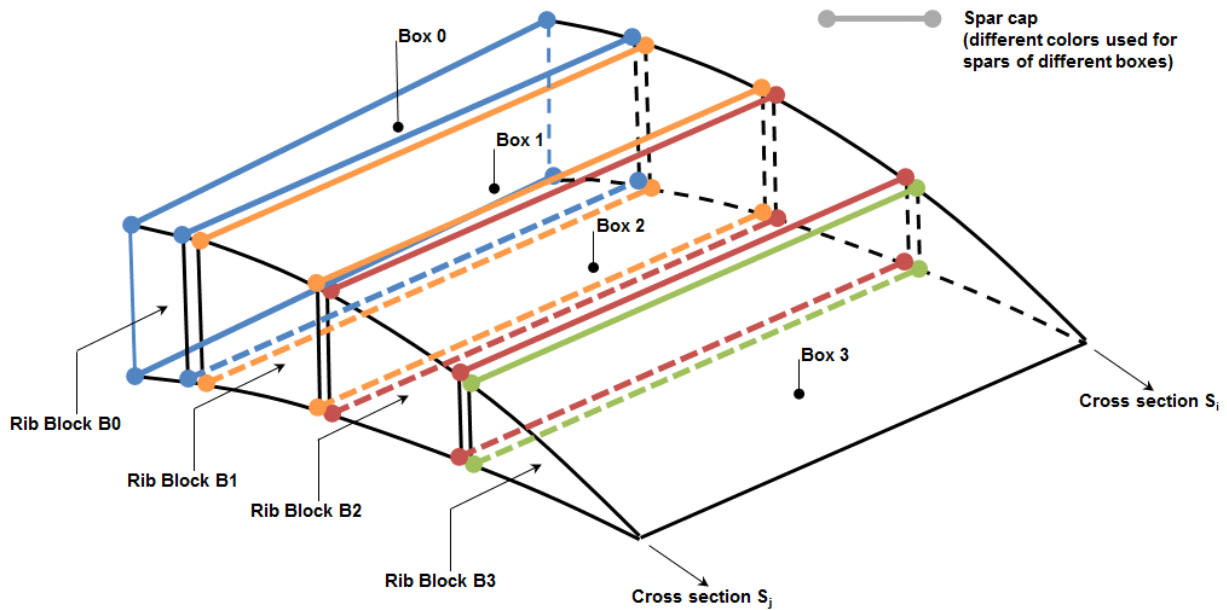
Fig. 17: Multi-box arrangement, equivalent static scheme of a generic bay

The structural sizing of each box was carried out referring to elementary methods under the following assumptions:

- AL2024-T5 alloy for all structural components (spars, rib plates and skin panels);
- ultimate load distributions pertaining to the trimmed level-flight condition at limit load factor, max take-off weight and dive speed;
- no interaction with adjacent boxes along the chord (each box of the multi-box arrangement was treated separately);
- box orientation with respect to the aerodynamic flow congruent with the un-morphed ATE configuration.
- rib planes perpendicular to the trailing edge line and intersecting the rear spar of the wing in correspondence of wing-box ribs surfaces. Such assumption was considered appropriate to properly transfer internal solicitations from the ATE structure to the wing-box.

Investigated load case Cp distributions (upper and lower Fig. 18) were interpolated along ATE rib planes; at each rib plane, the interpolated Cp distributions were conveniently replaced by linear piecewise distributions characterized by constant average values of (upper/lower) Cp along the chord of each ATE box.
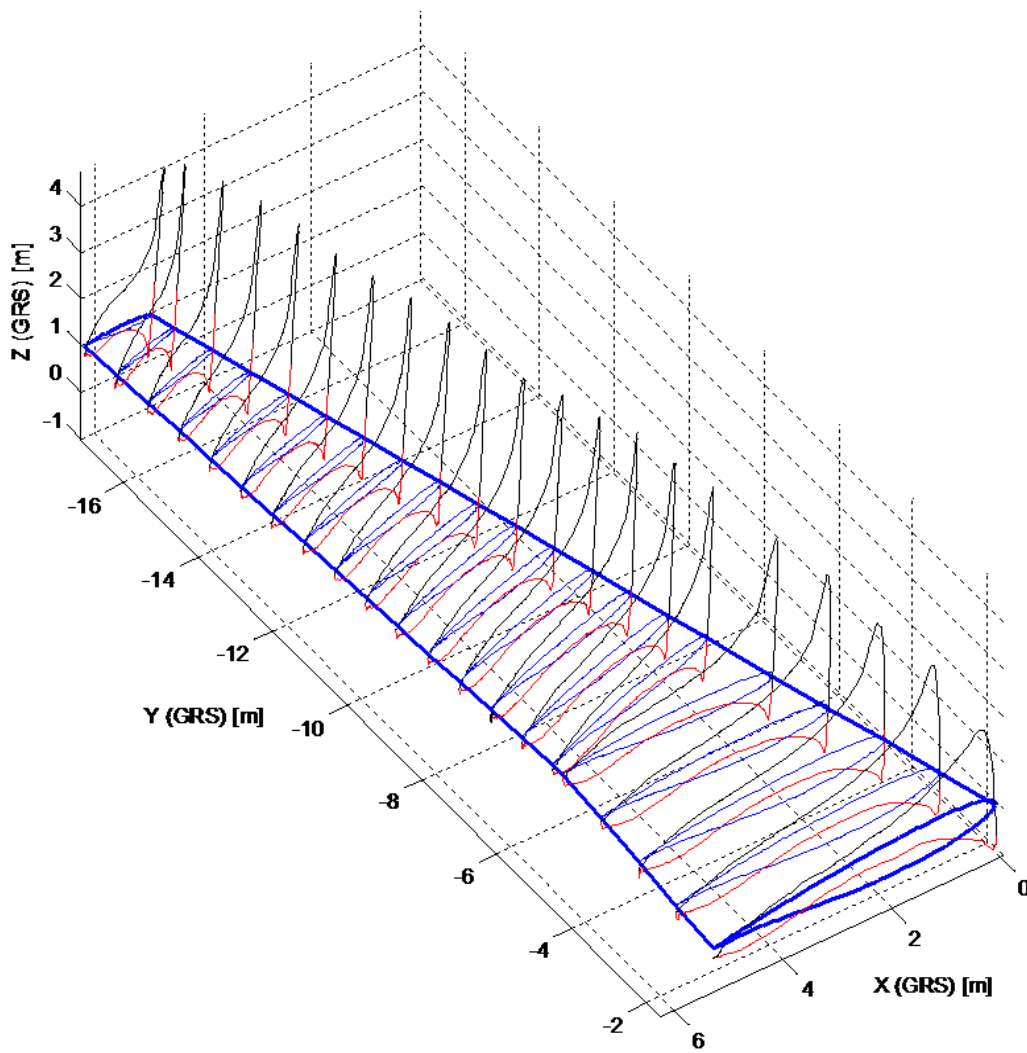
Fig. 18: Cp distributions across reference aerodynamic sections

The piecewise distributions were then multiplied by the dynamic pressure (at dive speed and sea-level) and by the factor 1.5; resulting pressure levels were finally integrated to get ultimate bending moment, shear and torque distribution along each section S_i of each ATE box.

For each cross section of each ATE box, the following approaches were used to assess the dimensions of the load bearing components (spar webs, spar caps, skin panels, rib plate).

Spar caps section area at generic section S_i

The ultimate bending moment $BM_{i(U)}$ at section S_i was assumed to be absorbed by front and rear spars caps according to the following criteria:

$$BM_{i(f)} = \frac{h_{i(f)}^2}{h_{i(f)}^2 + h_{i(r)}^2} BM_{i(U)} = \gamma \cdot BM_{i(U)} \tag{5}$$

$$BM_{i(r)} = \frac{h_{i(r)}^2}{h_{i(f)}^2 + h_{i(r)}^2} BM_{i(U)} = (1 - \gamma) \cdot BM_{i(U)} \tag{6}$$

where:

$BM_{i(f)}$ is the amount of section ultimate bending moment absorbed by front spar caps;

$h_{i(f)}$ is the height of the front spar;

$BM_{i(r)}$ is the amount of section ultimate bending moment absorbed by rear spar caps;

$h_{i(r)}$ is the height of the rear spar.

Normal stress induced by bending moments in front and rear spar caps were imposed equal to σ_{ref}, σ_{ref} being equal to 0.7 σ_{tu} (σ_{tu}: ultimate tensile stress of the material).

Required equivalent areas for front and rear spar were than obtained as:

$$Aeq_{i(f)} = \frac{BM_{i(f)}}{\sigma_{ref}} \cdot \frac{1}{h_{i(f)}} \tag{7}$$

$$Aeq_{i(r)} = \frac{BM_{i(r)}}{\sigma_{ref}} \cdot \frac{1}{h_{i(r)}} . \tag{8}$$

Equivalent areas where imposed equal to zero if resulting lower than 1 cm^2.

Spars webs, skin panels, rib plate thickness at generic section S_i

The x-position of the ultimate shear force in SRS was obtained as:

$$X_{S_{i(U)}} = -\frac{TM_{i(U)}^*}{S_{i(U)}} \tag{9}$$

$TM_{i(U)}^*$ being the ultimate torque moment at section S_i and referred to SRS Y-axis;

$S_{i(U)}$ the ultimate shear at station S_i.

Shear center x-position was assumed equal to:

$$Xsc_i = \frac{X_{i(f)} + X_{i(r)}}{2} \tag{10}$$

where $X_{i(f)}$ and $X_{i(r)}$ respectively indicate the x-positions of front and rear spar webs in SRS.

According to the made assumption on shear center position, the effective ultimate torque moment was replaced by a dummy value given by:

$$\overline{TM}_{i(U)} = S_{i(U)} \cdot \left| X_{S_{i(U)}} - Xsc_i \right| . \tag{11}$$

By invoking Bredt formula, cell's shear flow resulted equal to:

$$q_i = \frac{\overline{TM}_{i(U)}}{2\Omega_i} ,$$ (12)

Ω_i being the area enclosed by the cell.

The shear flows, arising in each element of the section, were then assumed equal to

$$q_{i(fw)} = q_i \frac{h_{i(f)}}{P_i}$$ (13)

$$q_{i(rw)} = q_i \frac{h_{i(r)}}{P_i}$$ (14)

$$q_{i(sk)} = q_i \frac{l_{i(sk)}}{P_i}$$ (15)

where:

$q_{i(fw)}$ is the shear flow in the web of the front spar;

$q_{i(rw)}$ is the shear flow in the web of the rear spar;

$q_{i(sk)}$ is the shear flow in the (upper/lower) skin panel;

$h_{i(f)}$ is the height of the front spar;

$h_{i(r)}$ is the height of the rear spar;

$l_{i(sk)}$ is the length of the (upper/lower) skin panel;

P_i Is the perimeter of the cell.

Shear stress induced by shear and torque moment along section elements were imposed to be equal to τ_{ref}, τ_{ref} being assumed equal to $\sigma_{ref} / \sqrt{3}$. Webs and skin panels thicknesses were therefore obtained by the equations:

$$t_{i(fw)} = q_{i(fw)} / \tau_{ref}$$ (16)

$$t_{i(rw)} = q_{i(rw)} / \tau_{ref}$$ (17)

$$t_{i(sk)} = q_{i(sk)} / \tau_{ref}$$ (18)

where:

$t_{i(fw)}$ is the thickness of the front spar web;

$t_{i(rw)}$ is the thickness of the rear spar web;

$t_{i(sk)}$ is the thickness of the (upper/lower) skin panels.

The thickness of the rib plate was assumed to be equal to the maximum value among $t_{i(fw)}$, $t_{i(rw)}$, $t_{i(sk)}$. Moreover, for practical reasons, the thickness of webs and skin panels were imposed to not be lower than 2 mm and 1.5 mm respectively.

It is evident that the above described approaches allowed for an *iso-stress* sizing of the structural elements at each cross section; in this way the dimensions of the structural elements at each section did not result oversized with respect to the internal solicitations along the section. The adequacy of the adopted arrangements is then investigated and assessed during the **advanced structural design** phase. Finite elements analyses are carried out to verify and –if necessary– to update the structural layout while removing all the simplifications made in the preliminary design. It is in fact in this phase that the *static interaction* between adjacent boxes is taken in account and the links joining not adjacent blocks are properly sized. Actuation chain, that is integral part of the load bearing structure, is investigated together with its interfaces to the surrounding structure.

Stiffness and inertial spanwise distributions obtained for each box were checked also from the aeroelastic stand point.

Since each box of the ATE is part of a multi-body structure driven by actuators, it was believed necessary to check if the stiffness and inertial distributions, obtained on the base of the iso-stress approach, resulted also adequate to avoid any flutter instability in the certification envelope.

Trade-off flutter analyses were then carried out to properly define *safety ranges* for trailing edge inertial and stiffness distributions in combination with different frequency levels of the control line harmonics. Flutter-free distributions were finally used as a reference database to properly adjust the iso-stress distributions.

The methodologies implemented for the trade-off flutter analyses and obtained results have been summarized in the next paragraph.

1.5   TRADE-OFF FLUTTER ANALYSES

Rational analyses were implemented to simulate the effects induced by variations of trailing edge actuators' stiffness on the aeroelastic behavior of the wing, in combination with different dynamic properties of the trailing edge structure. Sensitivity studies were carried out on the base of fast aeroelastic approaches involving simplified and reliable structural and aerodynamic models. Outcomes of sensitivity studies provided useful guidelines to judge the adequacy of the ATE structural configuration -resulting from the iso-stress approach (see §1.4) - in the framework of its potential impact on wing flutter instability.

1.5.1   *Structural model*

In order to perform fast sensitivity analyses, a simplified and fairly representative structural model of the wing system was generated referring to a stick-equivalent representation.

Stiffness and inertial properties of the aeroelastic model where extracted by two FE models that were elaborated by concurring partners of SARISTU Consortium to preliminary assess the structural layout of the reference wing:

Model A :   FE model of the right wing box structure, characterized by super-elements and coarse mesh (Fig. 19, (a));

Model B :   FE model of the right wing structure, covering also leading and (conventional) trailing edge architectures and characterized by refined mesh specifically conceived for detailed stress analyses (Fig. 19, (b));.

The position of wing box elastic axis was evaluated by means of an iterative procedure consisting of seven main steps:

A trial position of the elastic axis was assumed;

Nodes were added to Model A in correspondence of the intersection points between the elastic axis and ribs' planes;

At each rib, RBE2 elements were generated to slave the nodes of the rib boundary to the node at the intersection between the rib plane and the (imposed) elastic axis;

An arbitrary torque M_T, was applied along the elastic axis and in correspondence of its intersection with the plane of the rib located at wing tip. The master node on the root rib plane was constrained in all degrees of freedom;

Static analysis was performed in MSC-NASTRAN® environment and the following displacements were evaluated:

> TZi : displacement of the master node on the i-th rib along the axis Z perpendicular to the elastic axis and to the wing box middle plane (vertical bending displacement induced by M_T);

> RY_i : rotation of the master node on the *i-th* rib around the axis Y coincident with elastic axis (torsion induced by M_T);

- Ratios $\lambda_i = |TZ_i/RY_i|$ were evaluated at each rib location thus providing the offset of the actual shear centre with respect to its supposed position;

- At each rib location,. the master node defined at point 3 was shifted chordwise by the amount λ_i ;

- Steps from 4 to 7 were repeated until all ratios λ_i resulted quite equal to zero.
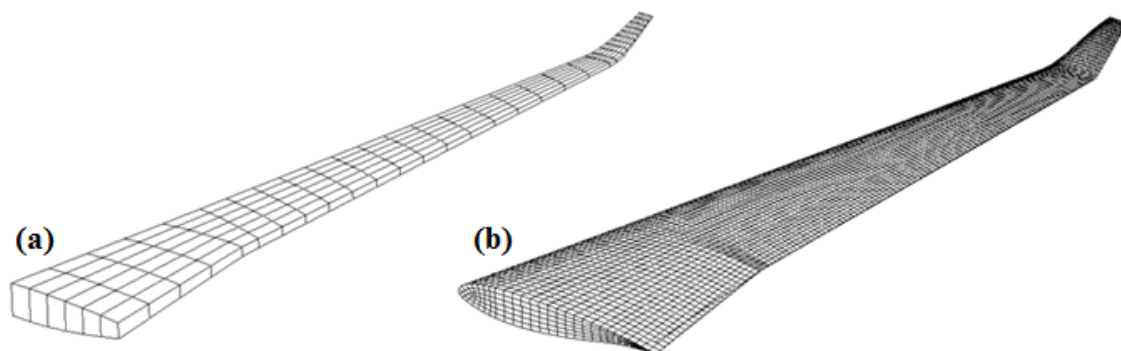

Fig. 19: FE reference models (RH wing): (a) Super-elements model [21], (b) Static model [23]

The same procedure was followed for the determination of the winglet elastic axis.

Stiffness distributions along the span of the wing box (/winglet box) equivalent beam were determined with reference to the Model A (modified according to the actions described at points 2 and 3) and to the following equations:

$$GJ(y) = \frac{M_T}{\frac{d}{dy}[RY(y)]} \tag{19}$$

$$EI_{min}(y) = \frac{BM_X}{\frac{d}{dy}[RX(y)]} \tag{20}$$

$$EI_{max}(y) = \frac{BM_Z}{\frac{d}{dy}[RZ(y)]} \tag{21}$$

$$EA(y) = \frac{F_Y}{\frac{d}{dy}[TY(y)]} \tag{22}$$

where:

- *X,Y,Z* are the axis of a Cartesian reference system characterized by:
  - origin at the beginning of the wing box (/winglet box) elastic axis (at the inner rib location of the item);
  - *Y* axis coincident with the item elastic axis and positively oriented towards item's tip;
  - *XY* plane coincident with wing (/winglet) *middle* surface;
  - Z axis normal to *XY* plane and upwards oriented.
- *y* is the generic coordinate along the Y-axis.
- *GJ(y)* is the torsional stiffness distribution.
- *EI$_{min}$(y)* is the vertical bending stiffness distribution (stiffness to bending across *XY* plane).
- *EI$_{max}$(y)* is the lateral (fore & aft) bending stiffness distribution (stiffness to bending across *YZ* plane).
- *EA(y)* is the distribution of the stiffness exhibited with respect to forces acting along the elastic axis (normal-to-sections solicitations).
- *M$_T$* and *RY(y)* are respectively an arbitrary torque moment acting around the elastic axis (Y-axis) at its free-end and RY(y) is the rotation around the Y-axis of the cross section at spanwise location *y*.
- *BM$_X$* and *RX(y)* are respectively an arbitrary bending moment acting around X-axis at elastic axis free-end and RX(y) is the rotation around the X-axis of the cross section at spanwise location *y*.
- *BM$_Z$* and *RZ(y)* are respectively an arbitrary bending moment acting around Z-axis at elastic axis free-end and RZ(y) is the rotation around the Z-axis of the cross section at spanwise location *y*.
- *F$_Y$* and *TY(y)* are respectively an arbitrary force acting along elastic axis (Y-axis) at its free-end and TY(y) is the displacement along the Y-axis of the cross section at spanwise location *y*.

The evaluation of wing-box' elastic axis provided a good correlation index, R2 = 0:7611, after a few iterations. The estimates were clearly impacted by the taper of the wing that results in a spike about the kink region (Fig. 20).
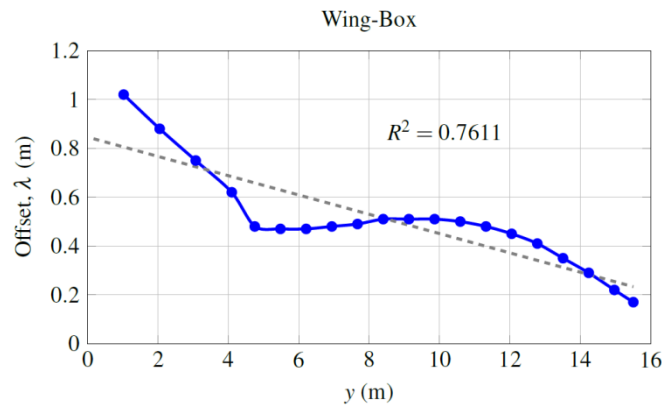

Fig. 20: Elastic axis determination

The elastic axis is partially represented in Fig. 21 ; the master node of each RBE2 element constitutes the elastic centre of every rib plane.
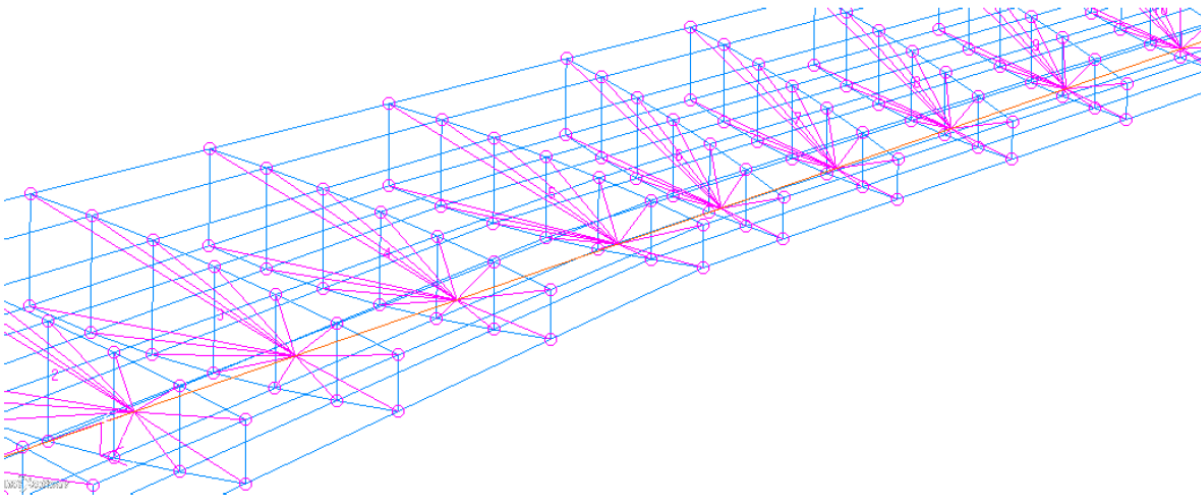

Fig. 21: Detail of wing-box FE model.

The following figures represent the elastic properties of the wing-box, evaluated by means of the methodology previously described. Fig. 22 shows the torsional stiffness versus the span direction.
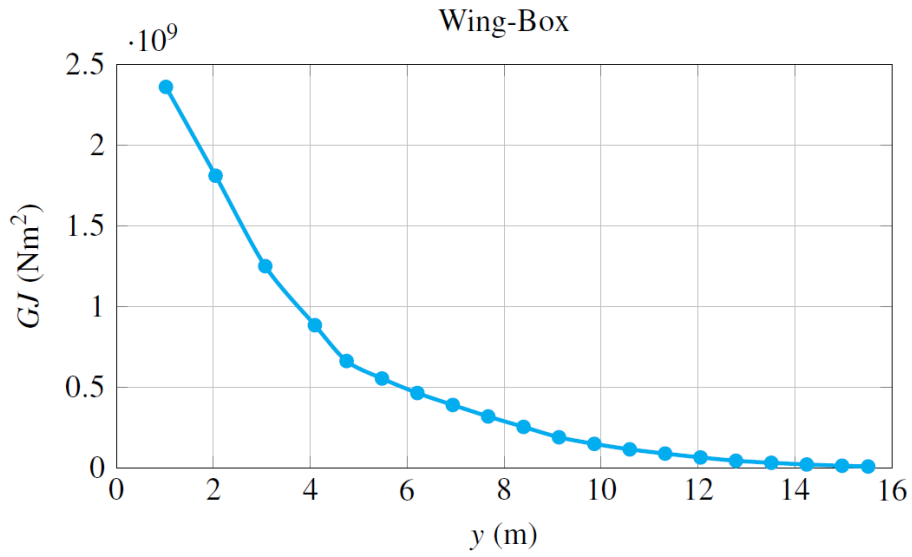
Fig. 22: Torsional stiffness vs span distribution.
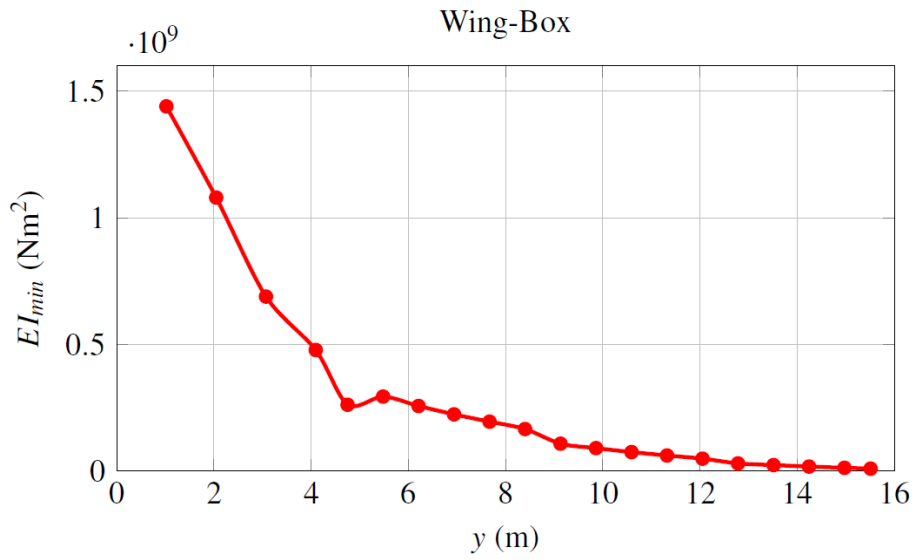
Fig. 23: Vertical bending stiffness vs span distribution
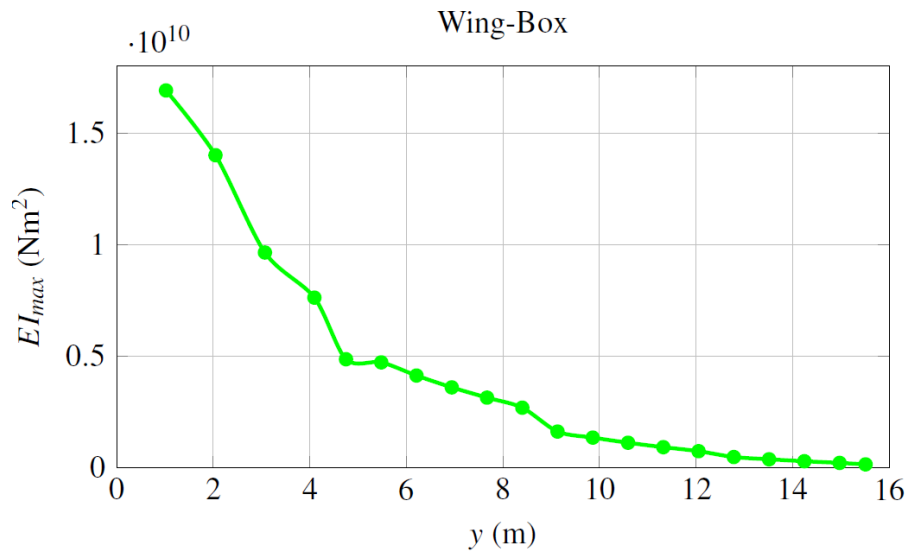
Fig. 24: Fore & Aft bending stiffness vs span distribution
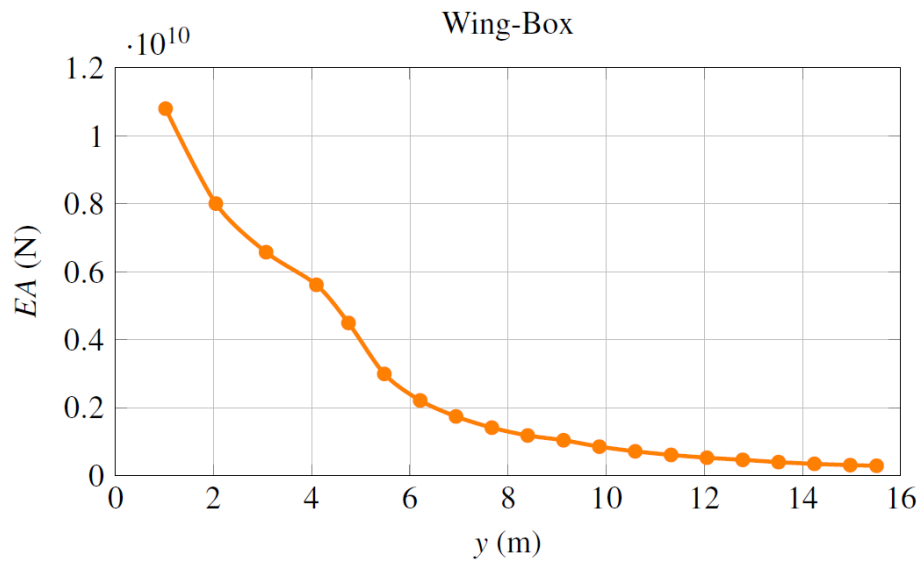
Fig. 25: Axial stiffness vs span distribution

Moreover the shear stiffness is not predicted because the wing is considered a thin beam; in such a way it is possible to neglect the shear effect.
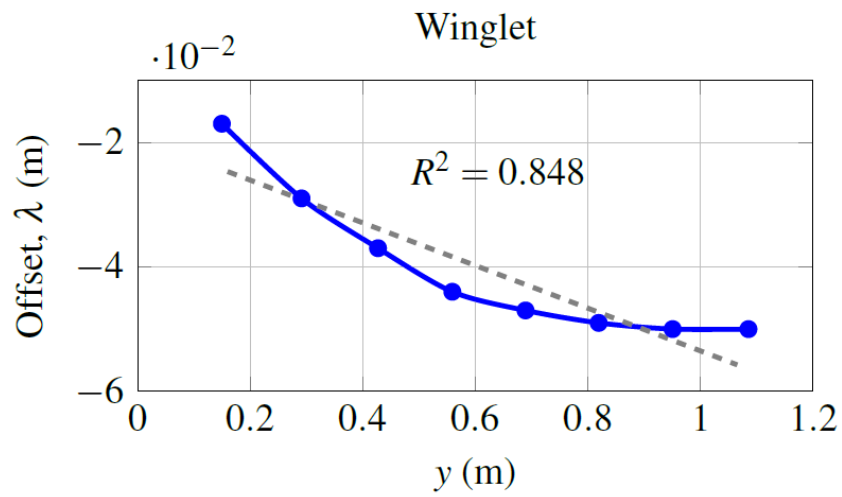
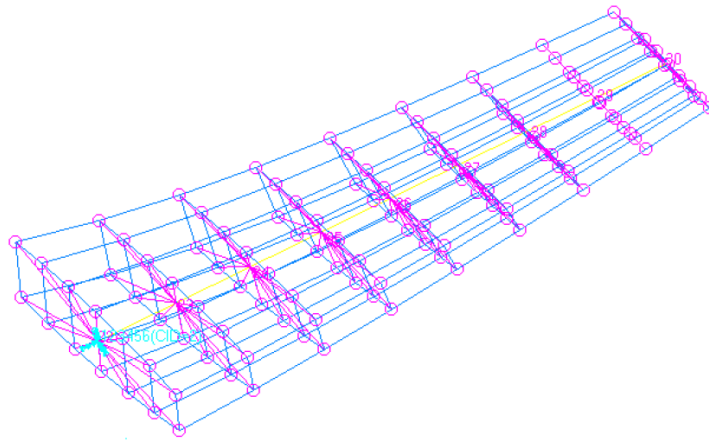The same iterative procedure was applied to the winglet.

Fig. 26: Winglet elastic axis determination.

Fig. 27: Detail of winglet FE model

Winglet stiffness distributions are summarized in the following sub-figures. The graphs show a more regular trend than the wing-box results: the winglet even if tapered does not exhibit strong variations about its planimetry.

25
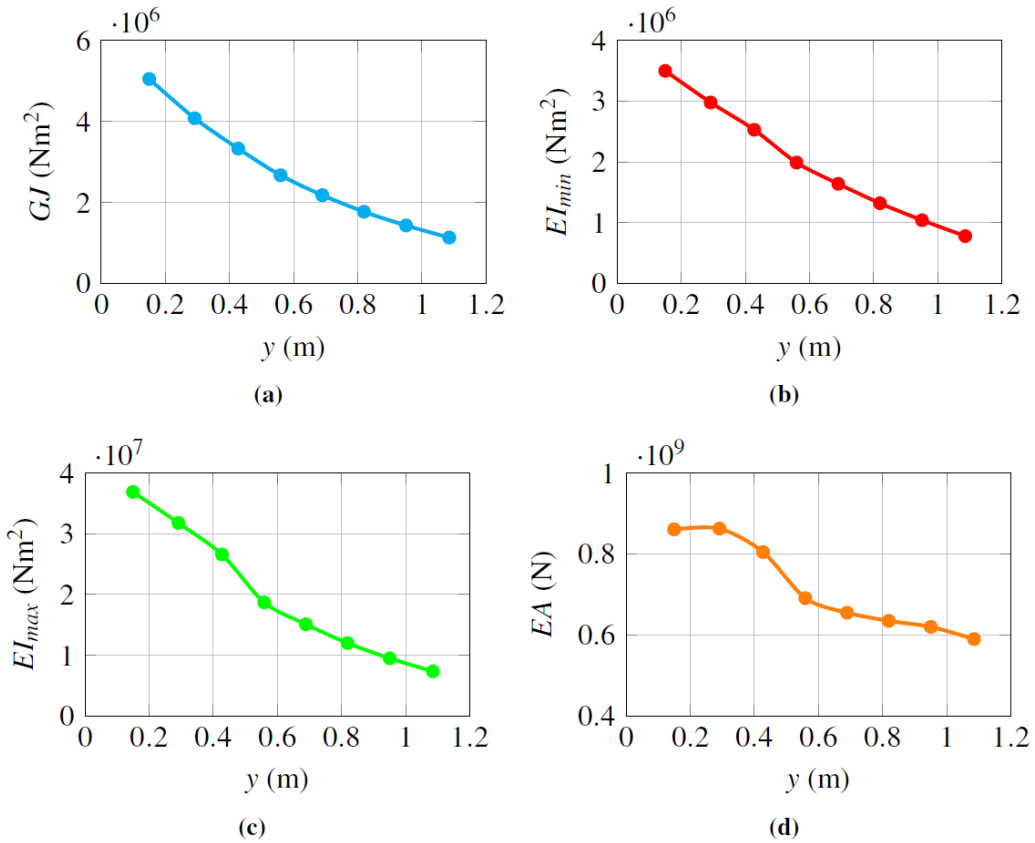
Fig. 28: winglet stiffnesses distributions.

For aeroelastic stability analyses, the morphing trailing edge was modeled as a conventional movable surface characterized by a unique hinge line located at

- 85% of the wing chord for the inner wing region (see Fig. 1);
- 88% of the wing chord for the outer wing region (see Fig. 1).

Stiffness properties of the equivalent beams representing the hinge lines were obtained always by equations (19)-(22) but referring, in this case, to Model B.

The stiffness distributions of all the other structural items (namely: leading edge, not movable trailing edge portions) were considered negligible.

The effect of such items on wing aeroelastic behavior was then considered only from the inertial standpoint (Fig. 29).

Equivalent lumped mass (/inertia) distributions were evaluated for all the structural items of the wing. For the generic item, the inertial properties of each bay were evaluated on the base of finite elements model data; such properties were then assigned to a CONM2-like element [18] located at the center of gravity of the bay (Fig. 30). Model A was used to evaluate the inertial properties of the bays belonging to wing and winglet box, while Model B was used for leading and trailing edge bays.

CONM2 elements were rigidly connected to the closest grid of the beam-equivalent model of the pertaining item.
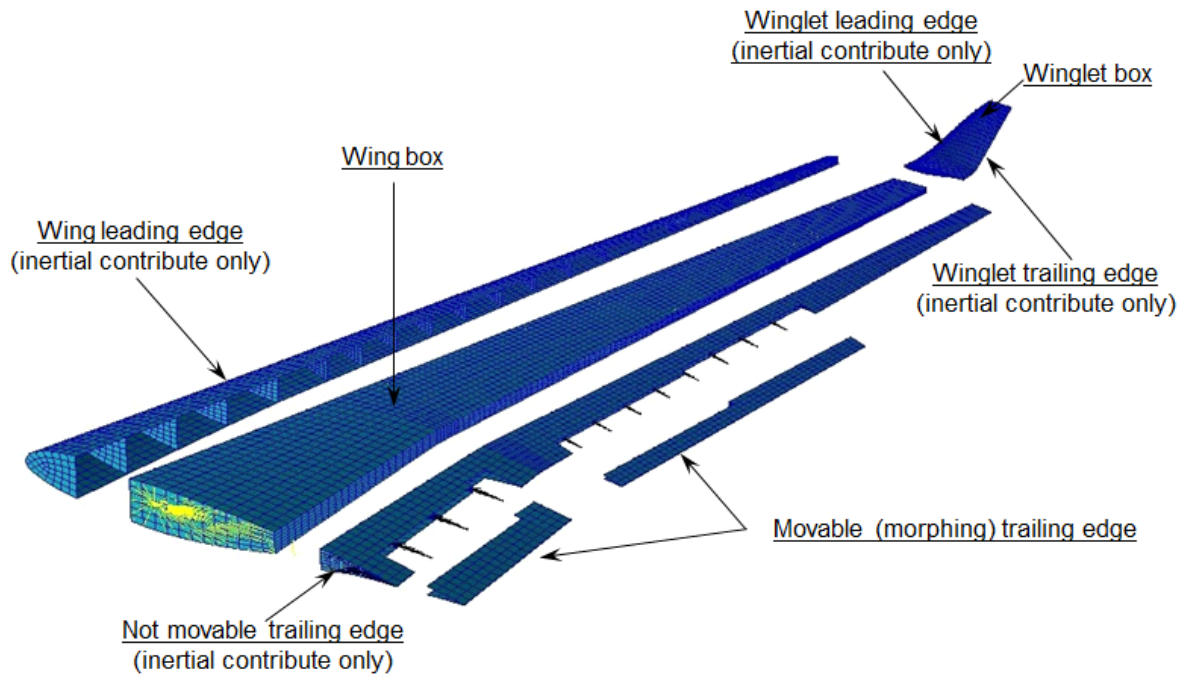
Fig. 29: Items considered for the generation of the wing aeroelastic model
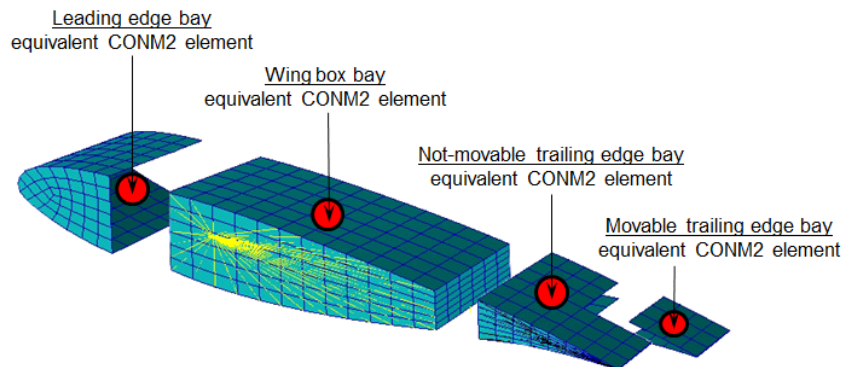

Fig. 30: Example of inertial condensation for a wing bay

The structural model of the left wing was obtained by mirroring with respect to aircraft symmetry plane. Right and left hand side models were then linked to a central node (on aircraft symmetry plane) by means of DMIG elements generated to simulate the stiffness of the wing-fuselage interface (Fig. 31). DMIG elements solution was also implemented to connect wing and winglet elastic axes. The hinge lines of the morphing trailing edge were linked to the elastic axis of the wing by means of stiff beam elements; pin flags were properly imposed at the end-nodes of such elements to release the rotation around the hinge lines. A torsional spring element was finally added at the inner node of each hinge line to simulate actuators stiffness.
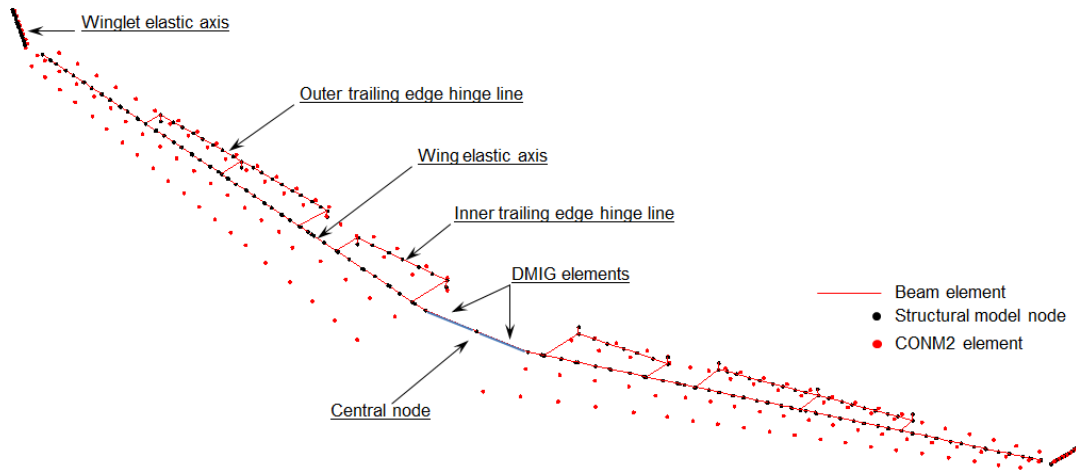
Fig. 31: Equivalent structural model of the wing (rigid elements hidden for clarity)

1.5.2 Aerodynamic and interpolation model

Matrices of unsteady aerodynamic influence coefficients (AIC) were evaluated by means of doublet lattice method (DLM). The aerodynamic lattice of the wing (Fig. 32) was generated by properly meshing the middle wing plane through 8 macro-panels for each side of the wing; macro-panels were further meshed into elementary boxes; higher boxes density was considered for the movable trailing edge and -to assure mesh uniformity- also for the not-movable trailing edge.

Modal displacements at the centre of each aerodynamic box were obtained by means of linear spline functions attached to *support-nodes* of the structural model. In Fig. 33 the aerodynamic and structural models have been depicted together.
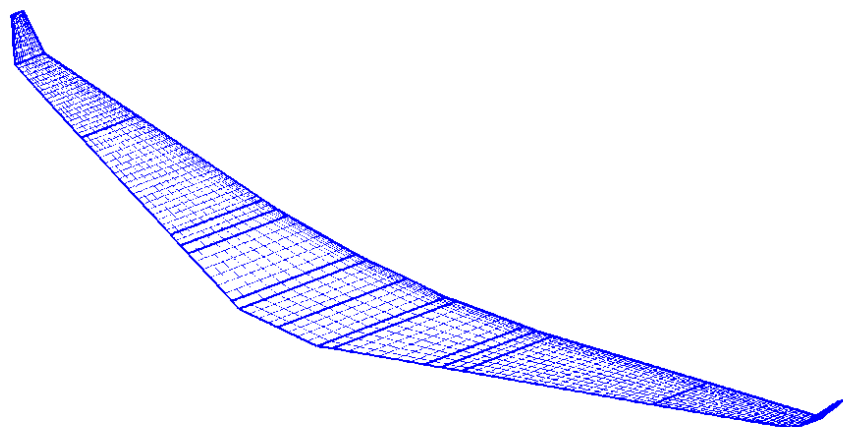

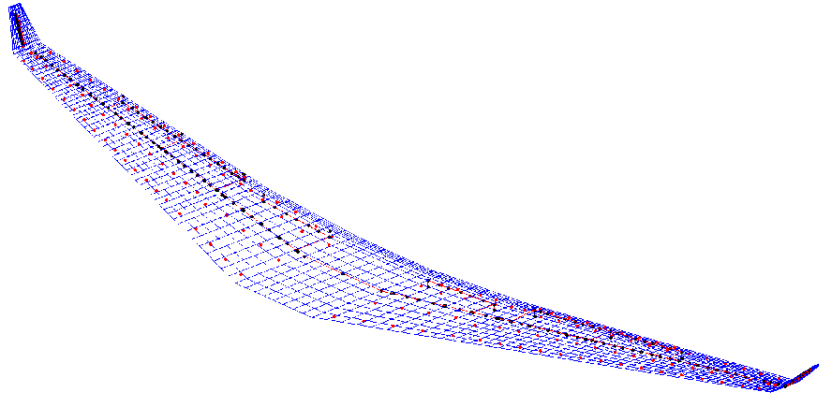**Fig. 32: Aerodynamic model (thick lines represent panels' boundaries)**

Fig. 33: Structural and aerodynamic models

1.5.3   *Flutter analyses, assumptions and investigation cases*

Flutter analyses were carried out under the following assumptions:

- PK-continuation method with rationalization of generalized aerodynamic forces for the evaluation of modal frequencies and damping trends versus flight speed;

- theoretical elastic modes association in the frequency range 0Hz-60Hz (elastic modes being pertinent to free-free aircraft, with only plunge and roll motions allowed);

- modal damping (conservatively) equal to 0.01 for all the elastic modes;

- sea-level altitude, flight speed range 0-300 m/s ($\approx$1.5 V_D, V_D(dive speed) = 205.9 m/s, [1]).

Flutter speeds were evaluated in correspondence of different settings for the movable trailing edge, each setting being defined by means of three (trade-off) parameters:

- inertial distribution;
- stiffness distribution;
- harmonic frequency (i.e.: frequency of the elastic deflection at locked actuators).

Investigated cases mapped three different inertial distributions in combination with three different stiffness distributions and five harmonic frequencies of the movable surface (Table 1); the trade-off domain was therefore composed by forty-five different configurations of the movable trailing edge.

Table 1: Values of trade-off parameters.

Movable trailing edge inertial distribution	Movable trailing edge stiffness distributions	Movable trailing edge harmonic frequency [Hz]
Baseline	Baseline	0
		15
Baseline*1.3	Baseline*1.15	30
		45
Baseline*1.6	Baseline*0.85	60

The harmonic frequency was set by manipulating the stiffness of the movable trailing edge actuators; in order to get a given frequency f, the torsional stiffness K_a of the actuators was imposed equal to:

$$K_a = \left(\frac{f}{2\pi}\right)^2 \cdot I \tag{23}$$

where I stands for the inertia of the movable trailing edge around its hinge line.

The condition f = 0 Hz was taken in account to simulate actuators failure; in such a case the movable trailing edge harmonic obviously coincides with its fundamental (free rotation around the hinge line).

1.5.4   Analysis outcomes and guidelines

For each investigation case flutter speeds and flutter mode were evaluated. Accurate analysis of modes participation factors into flutter mode were performed in order to isolate the principal modes involved in each detected flutter.

Two types of flutter were identified for all investigated cases:

- bell-shaped flutter;
- sharp flutter.

Both flutter types occurred in all investigated cases but at different speeds; in some cases the flutter speeds related to one or to both flutter types resulted outside the speed investigation range ([0:300 m/s], see previous paragraph).

In Fig. 34 the trends of modes frequencies and damping versus flight speed have been plotted with reference to a generic case of investigation for which both flutter types are present in the speed investigation range.
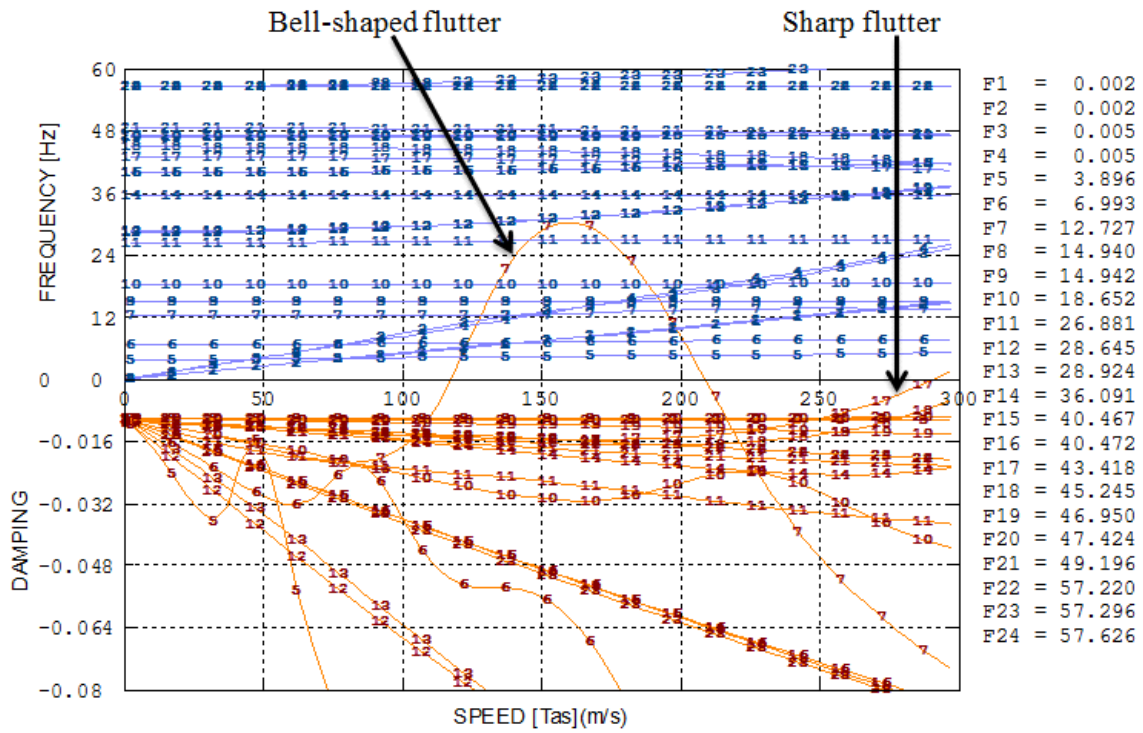
Fig. 34: Modes frequency/damping versus flight speed

The first type of flutter was found to be due mainly to the coupling of two modes (binary flutter): the first symmetric wing bending (Fig. 35) and the outer trailing edge symmetric harmonic (or fundamental, in case of actuators failure, Fig. 36).

The dynamics of the sharp flutter resulted instead more complex: three modes are *mainly* involved, namely, first symmetric wing bending, outer trailing edge symmetric harmonic and outer wing symmetric torsion (Fig. 37).
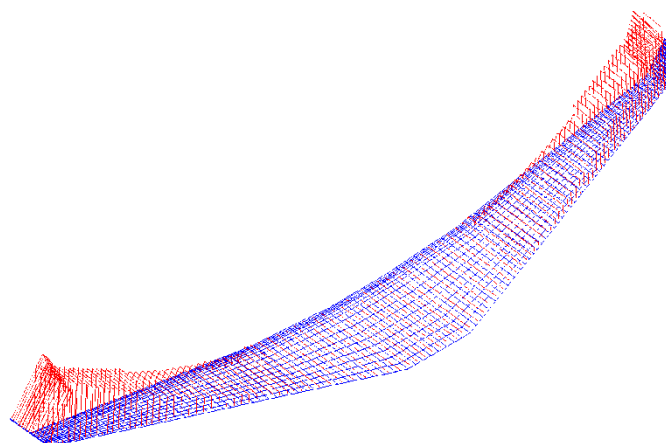
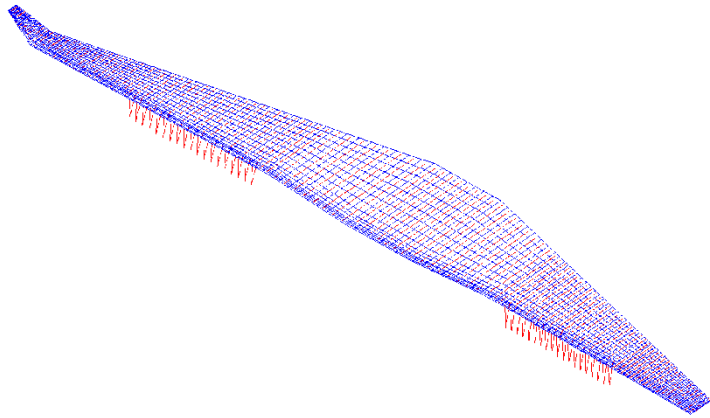**Fig. 35: 1st wing bending (symmetric)**

31

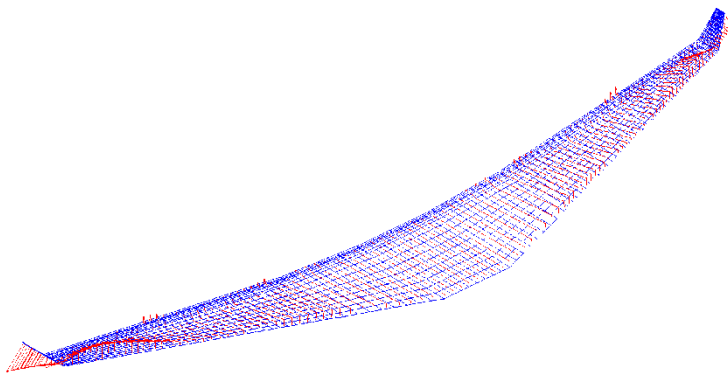**Fig. 36: Outer trailing edge harmonic (symmetric)**

Fig. 37: Outer wing torsion (symmetric)

A stability carpet plot was generated to provide a thorough overview of flutter speed trends versus the frequency of movable trailing edge harmonics (Fig. 38).
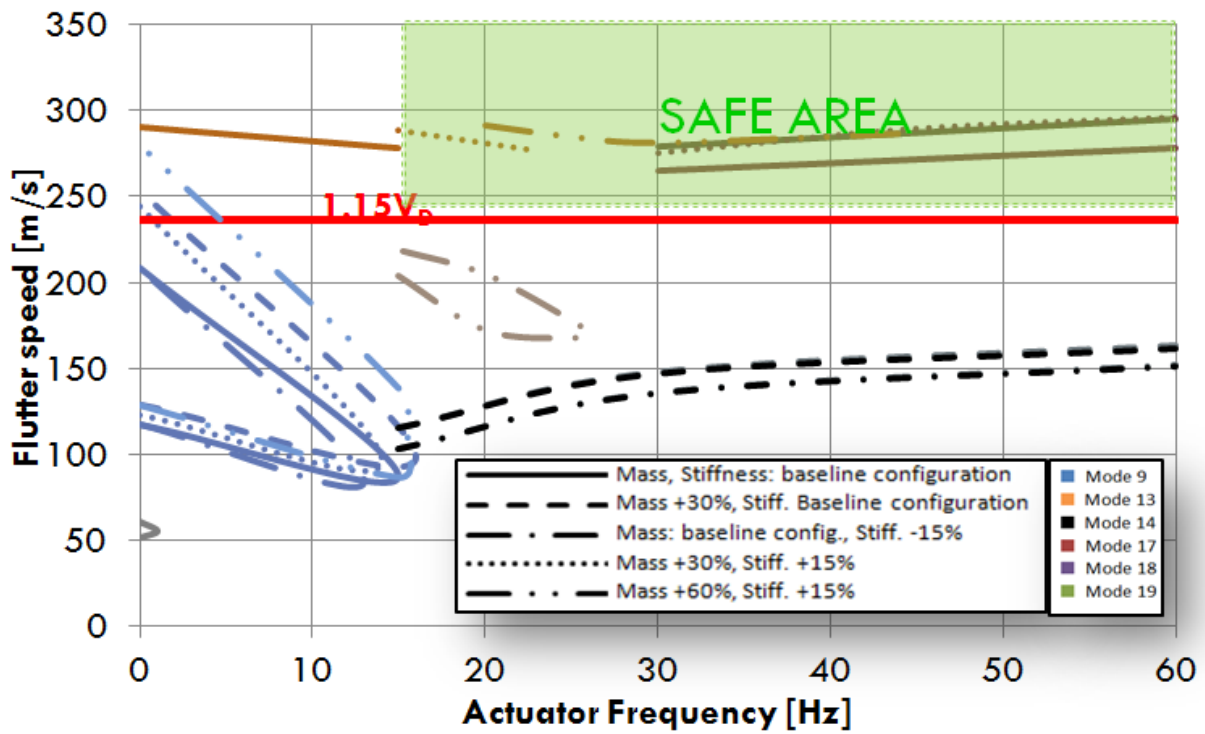
Fig. 38: Carpet plot of flutter speeds

Each curve of the carpet plot has been coloured according to the flutter mode it refers to; moreover the line-style of each curve has been chosen according to the pertaining trailing edge configuration (i.e.: investigation case).

Only five of the forty-five investigation cases are covered by the carpet plot; this is due to the fact that the remaining forty cases resulted in flutter speed greater than 300 m/s.

The red horizontal line at constant speed equal to 1.15 V_D, divides the carpet plot in two different regions:

- the region above the red line, defining the safe domain for flutter speed according to CS-25, paragraph 629;

- The region below the red line, defining the unsafe domain for flutter speed occurrence.

If the inertial distribution of the movable trailing edge is kept equal to its nominal value and its stiffness distributions is reduced by the 15%, flutter occurs at flight speeds lower than 1.15· V_D whatever is the frequency of the trailing edge harmonic. The same happens if the inertial distribution is increased by the 30% and the stiffness distributions are equal to the nominal ones. These dangerous combinations of inertial and stiffness distributions where therefore carefully avoided in assessing the structural properties of the ATE.

For all the other inertial/stiffness configurations covered by the carpet plot, a minimum frequency of 30 Hz for the trailing edge harmonic resulted sufficient to avoid any flutter instability up to 1.15· V_D.

In case of actuators failure (harmonic frequency equal to 0 Hz) flutter always occurs at speeds within the certification envelope. Although the simultaneous failure of actuators represents an event of extremely

remote probability, it was found that -even in such case- flutter is avoided by a suitable mass-balancing of the movable trailing edge with respect to its hinge line.

1.6 3D CAD OF THE MORPHING STRUCTURE

1.6.1 ATE Demonstrator region

According to SARISTU work plan, the functionality of the ATE device, as well as of the other morphing technologies developed within the project, is expected to be proven by means of experimental tests. Tests will be carried out on a common platform (*technology demonstrator*), fully representative of the outermost region of the reference wing (4,5 m span) and equipped with all morphing devices and related systems (Fig. 39).
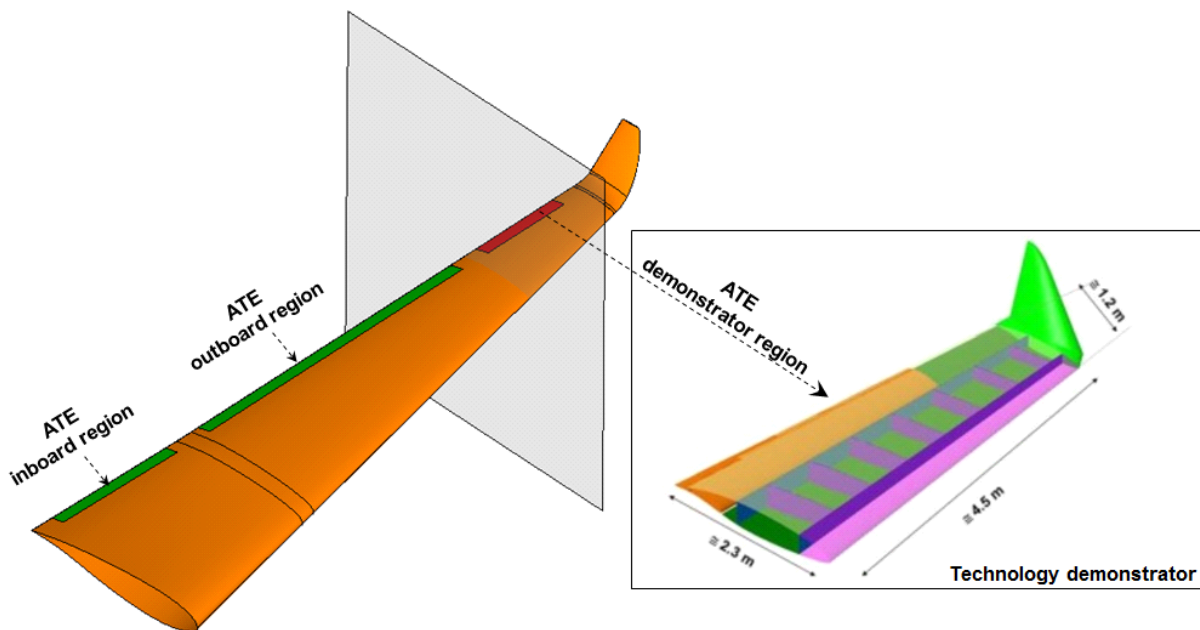

Fig. 39:Technology demonstrator and ATE demonstrator region

Fig. 39 shows the main dimensions of the technology demonstrator as well as its location on the LH reference wing. Recalling ATE design specifications reported at §1.1(and in [21]), it appears evident that the technology demonstrator covers the wing region pertinent to the aileron and where no ATE installation is therefore foreseen. Results from the preliminary design of the outboard ATE were then rationally extrapolated to the demonstrator region in order to assess the morphing structure to be manufactured and tested.

Since outboard and inboard ATE are not supposed to be manufactured in the framework of SARISTU project, higher priority was given to the emission of refined 3D-CAD for the ATE demonstrator. The general layout and main structural properties preliminarily assessed for the device were duly converted into detailed drawings of each constitutive component. Adopted solutions were based on designer's industrial

34

experience and were mainly oriented to increase the structural robustness of the system, to minimize manufacturing costs and to simplify assembly and maintenance processes. The assembly drawing of ATE primary structure is reported in Fig. 40.

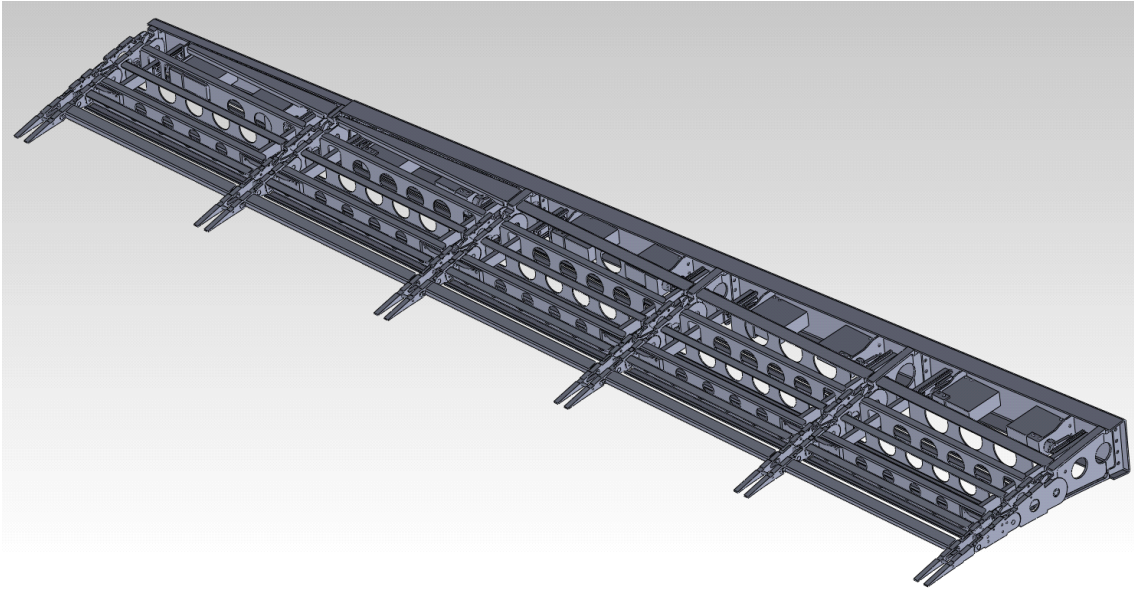The primary structure is characterized by four interconnected boxes composed by five bays of 0.40 m span.

Fig. 40: ATE primary structure (demonstrator region)

The most forward box is rigidly connected to the wing box through an *interface spar*; the remaining ones are moved by active ribs upon the action of actuators. Actuation leverages move synchronously the block B2 of each rib, thus making the entire structure to morph. If the motion of the leverages is prevented by locked actuators, the entire structure preserves its external shape under the action of aerodynamic loads. For each rib, the blocks B1, B2 and B3 were duplicated (Fig. 41) and links L1, L2 were located among them.
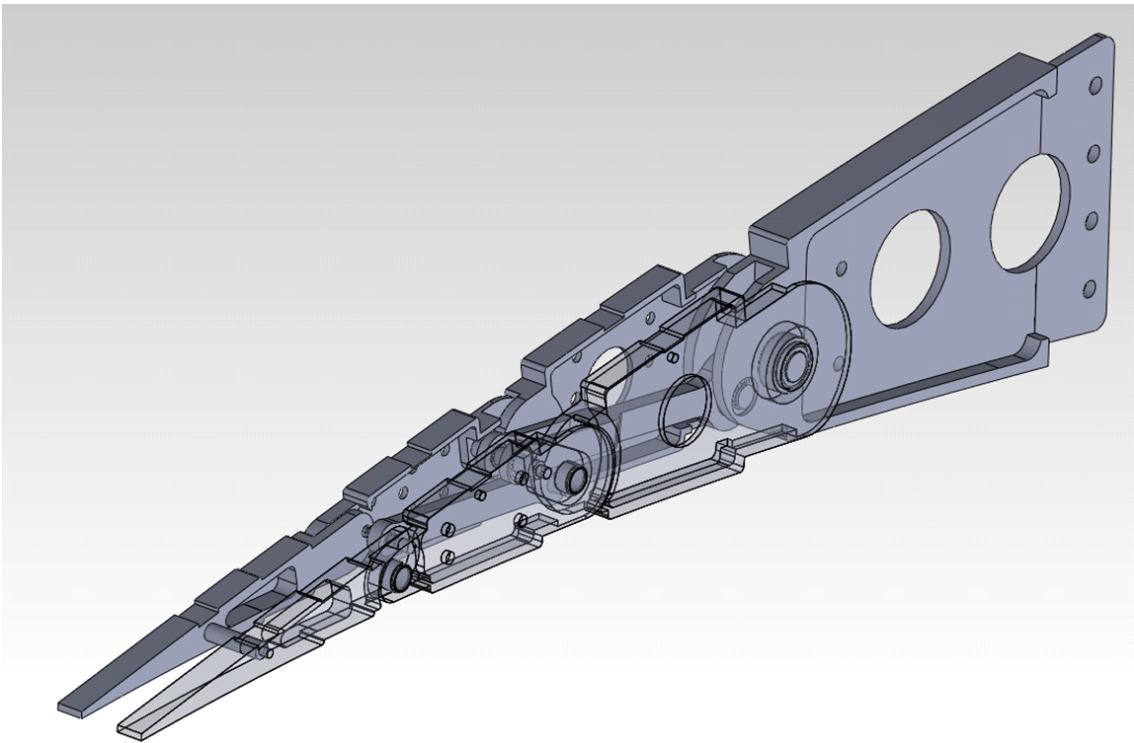
Fig. 41: Morphing rib layout

In this way, a compact and robust solution was assured for the morphing rib; moreover, it was prevented any interference between links and longitudinal stiffening elements (spar/stringers) during morphing. Hinges of rib mechanism were implemented through frictionless bushings at joints B, C, L_{2-1}, L_{2-2}, L_{1-2} (see §1.3).
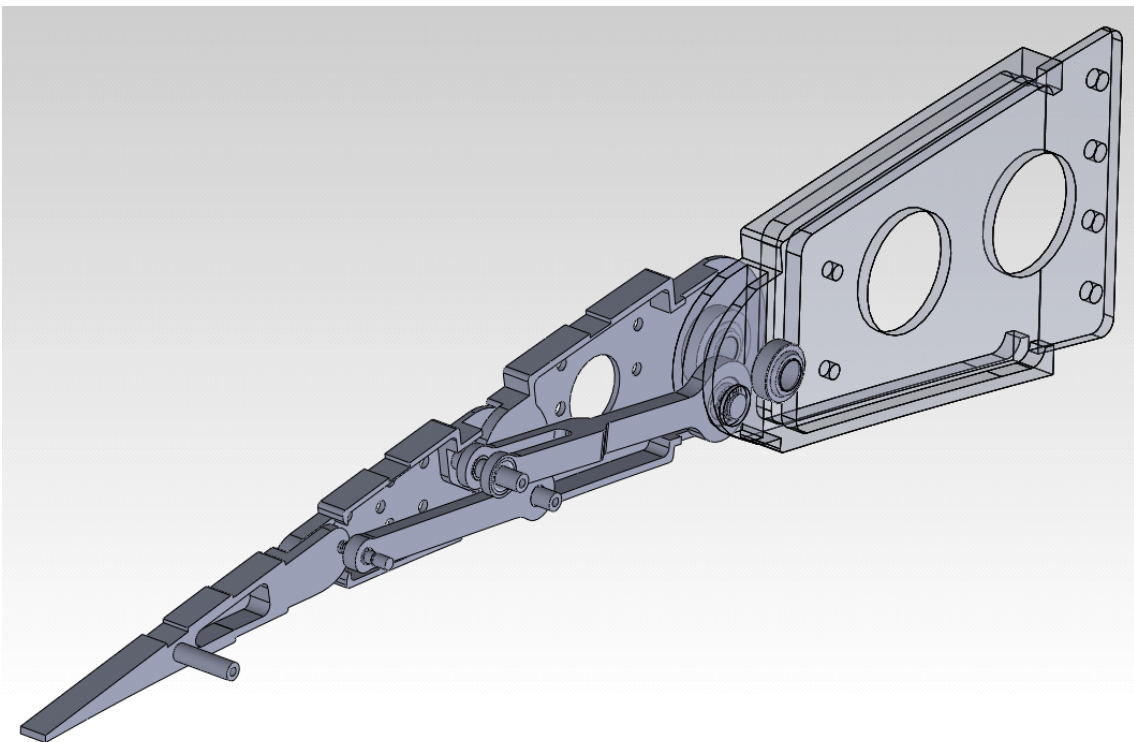

Fig. 42: Morphing rib hinges

Spherical hinges based on frictionless bearings were instead implemented for all the joints to block B0, namely, L_{1-1}, A. The spherical hinges solution at block B0 was adopted in order to compensate the out-of-plane elastic displacements induced by bending moments, thus preventing mechanism jamming under the action of external loads. Commercial off-the-shelf components (compliant with aeronautical standards) were used for bushings and bearings.

The fork-shape of link L1 (Fig. 42) was properly designed to avoid any interference with link L2 during morphing. The entire mechanism was checked from the interference standpoint up to two times the maximum design excursions. Such *safety margin* with respect to the interference, was believed necessary to enable the actuators to recover elastic deformations of the actuation chain, thus restoring target morphed shapes under the action of external loads.

The goodness of approaches followed for the design of all rib components was successfully proved trough a preliminary manufacturing test of a rib assembly. The rib prototype resulted extremely feasible, robust with respect to deviations from design tolerances and smoothly morphable.
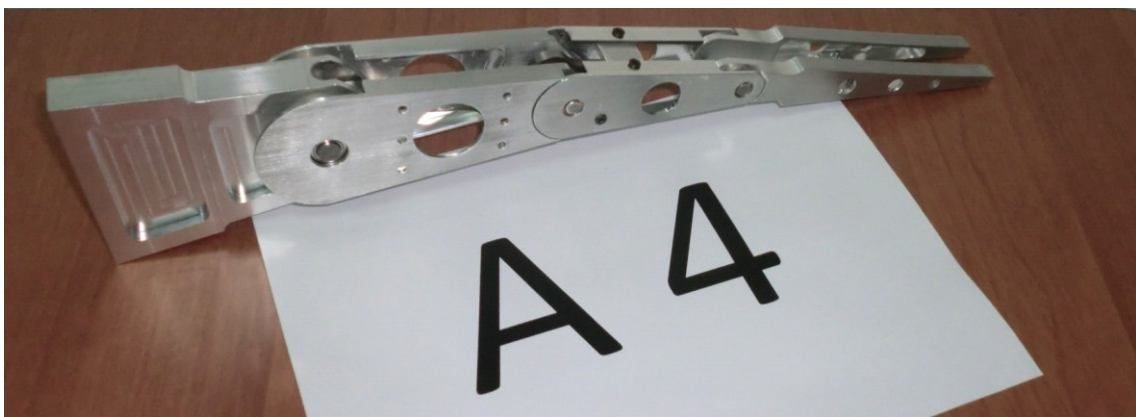

Fig. 43: Prototype of the morphing rib

The shape of rib blocks at skin interface (Fig. 44) was assessed to accommodate foam segments of the morphing skin across camber line hinges (A,B,C) as well as the components of the sensing system. The protuberance of block B1 across joint A, was properly sized to adequately mass-balancing the ATE and consequently to avoid any flutter instability also in the extremely remote event of simultaneous actuators failure.
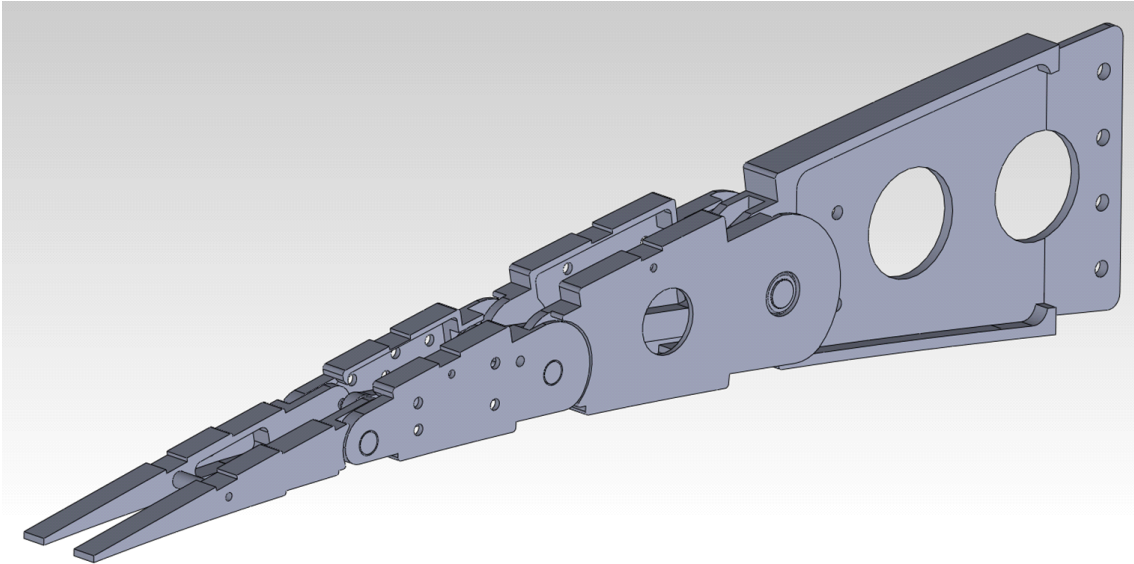
Fig. 44: External shapes of rib blocks

Spar and stringers were located in chordwise positions compliant with morphing kinematic as well as with bending/torsion stiffness requirements coming from the preliminary design. Particular attention was paid to the definition of spar webs cut-out crossed by the actuation leverages (Fig. 45): the morphing evolution of the actuated system was deeply investigated and cut-out size was assessed in order to avoid interference between ATE primary structure and actuation system's elements.
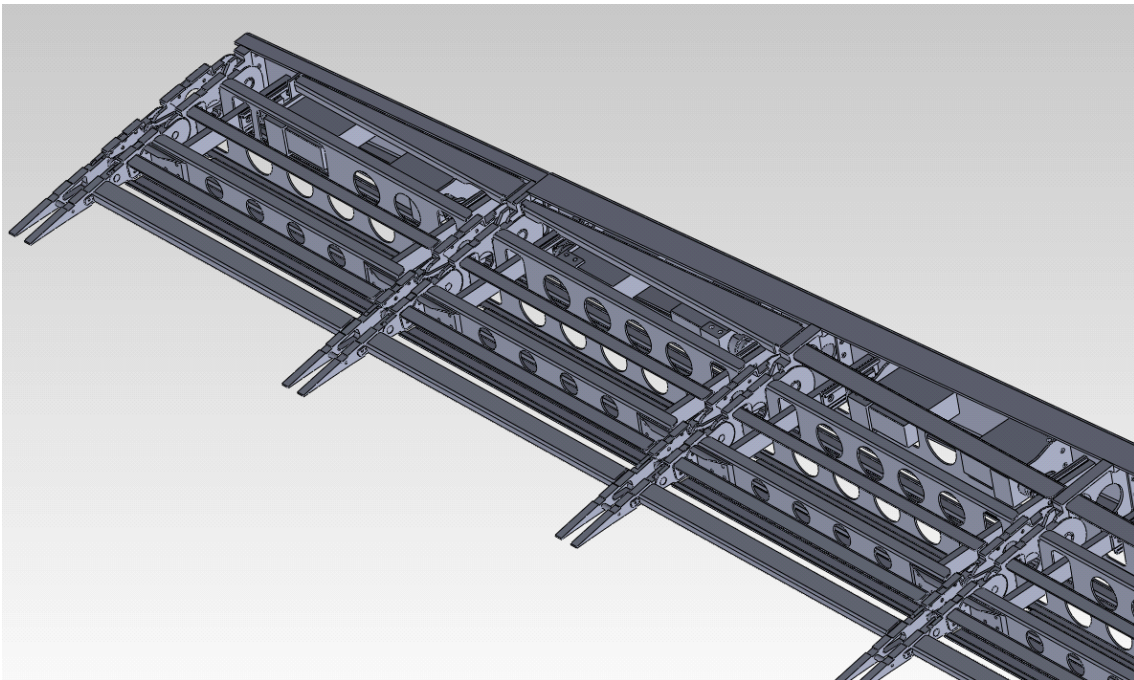

Fig. 45: ATE primary structure (last 3 bays of the demonstrator region)

Referring to the lower side of the primary structure, each spar (or stringer) was provided with Z-shaped flanges (Fig. 46) to support foam segments of the morphing skin in withstanding the compression forces induced by the aerodynamic flow.
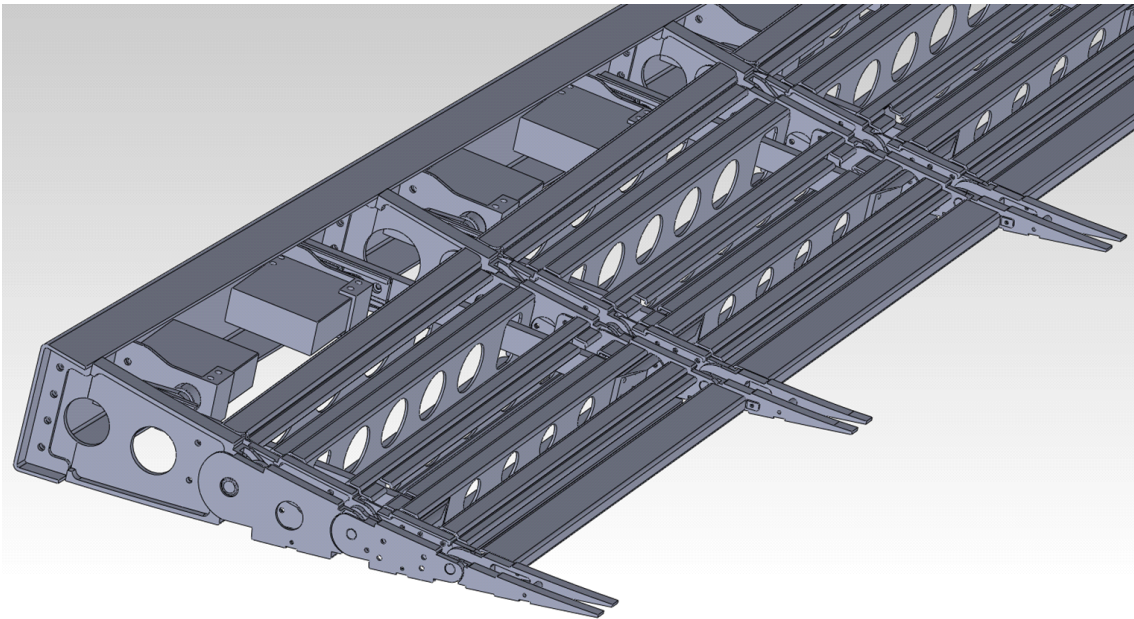
Fig. 46: Z-shaped flanges of spars (first two bays of the primary structure, lower side)

Each component has been identified by a specific part-number composed by 7 fields (Table 2). Commercial components (bushings and bearings) have been identified by means of the commercial code provided by the supplier. In Fig. 47 some components have been highlighted together with their part-number and part-number explanation.

Table 2: Part-numbering logic

Designer Acronym	TE Zone	Macro-Assy ID	Sub-Assy ID	Component ID	Position ID	Rev Id
UNINA	DEM	BAY1	RIB1	BLOCK0	RH	0
		BAY2	RIB2	BLOCK1	LH	
		BAY3	RIB3	BLOCK2	X	
		BAY4	RIB4	BLOCK3		
		BAY5	RIB5			
			RIB6			
		X	X	LINK	BiBi+2	

Designer Acronym	TE Zone	Macro-Assy ID	Sub-Assy ID	Component ID	Position ID	Rev Id
UNINA	DEM	BAY1	SPAR	X	FBi	0
		BAY2			RBi	
		BAY3			SBi	
		BAY4	STRINGER		SUBi	
		BAY5			SLBi	

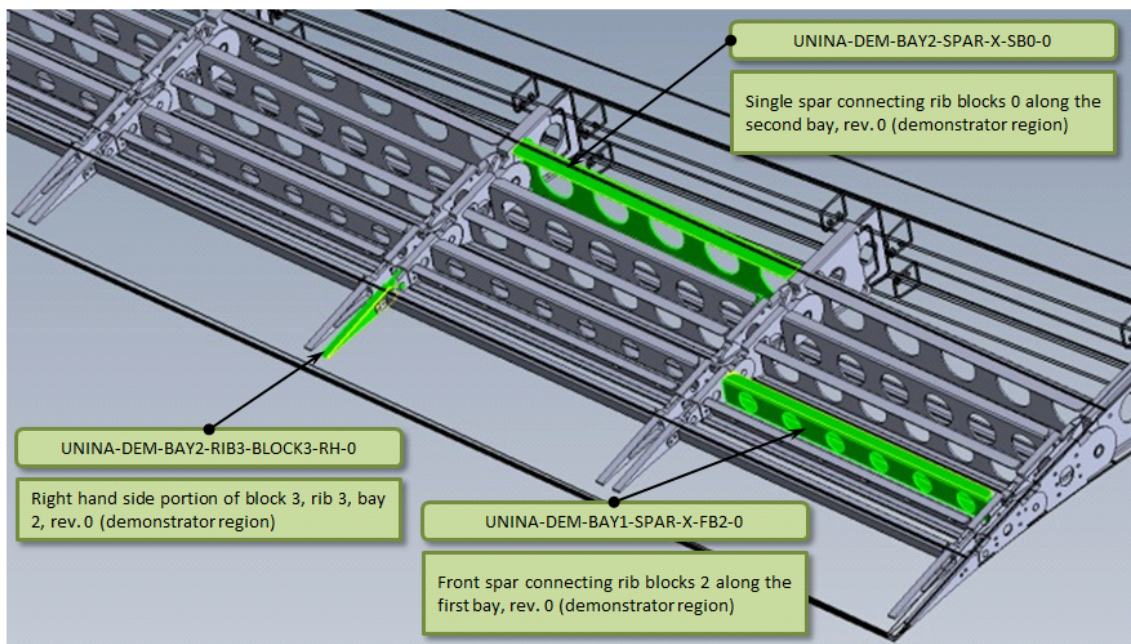|	
X	Not applicable
RH	Right hand side (closer to wing root)
LH	Left hand side (closer to wing tip)
Bi	i-th rib block
F	Front (closer to wing leading edge)
R	Rear (closer to wing trailing edge)
S	Single
U	Upper
L	Lower

Fig. 47: Part numbers examples

Final revision was made after the outcomes of the FE analysis described in §1.7.

A brief description of the other ATE components, which were not under the responsibility of University of Naples, is provided hereinafter to globally describe the overall system.

1.6.2   Skin System

Concepts for the ATED largely deformable skin wing parts were developed by Fraunhofer IFAM with the objective to release a smooth, gapless transition between movable and fixed parts. In order to maintain a smooth geometry, preserving the air flow from early detachment, the modular skin involves flexible segments. Stiff segments are instead used to compensate deformations due to air pressure gradients, (Fig. 48). Materials behavior was first evaluated by devoted numerical studies, considering actual deformations consequent to actuation forces and external aerodynamics.

A specific material system was tailored in order to meet a set of established requirements. Adhesive joints are used to guarantee a permanent connection between foams and structural materials. Fracture surface analysis is used to evaluate the interface stability. Results of mechanical tests proved the goodness of the proposed solution. The tests involved static and fatigue loads and took account of physical aging aspects in the range between -55°C to +80°C.
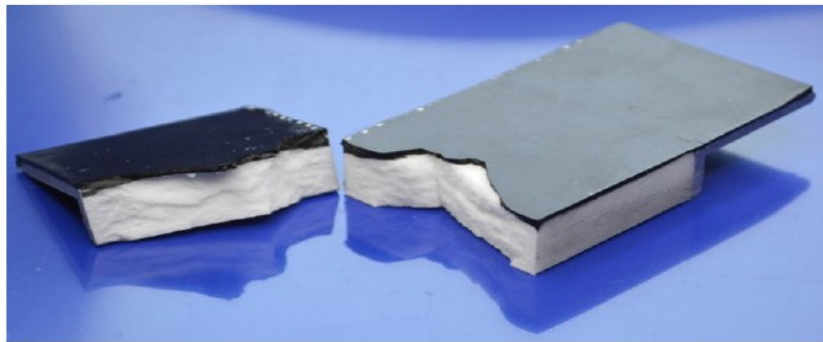

Fig. 48: SI rubber / SI foam / Al joint for fatigue evaluation. Adhesive strength leads to cohesive failure - Fraunhofer IFAM.

The selected morphing skin concept was tested till to physical sub-component level. In summary, a large deal of investigations was performed on interface technology, joints technology, manufacturing and mechanical testing. As a final result, a complete morphing skin panel, was delivered and ready for WTT (Fig. 49)
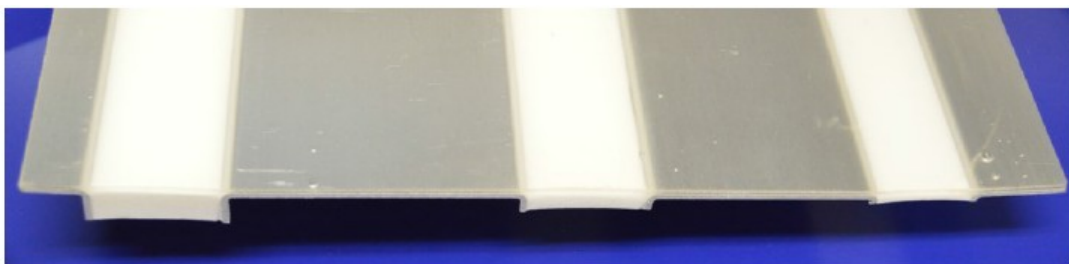

Fig. 49: Complete SI-SI-Al Morphing Skin; detail.

1.6.3 Actuator & Control System

SARISTU proposes a state-of-the-art actuation system, including advanced electromechanical actuators (Fig. 50), developed by CIRA with the specialist support of Fraunhofer ENAS. An SRF (Safety, Reliability and Failure) approach was implemented to evaluate system airworthiness in a low-critical aircraft control surface, such as ATED, by pursuing:

• Simplicity: "direct-drive" actuation, without gearboxes

• Redundancy: duplication of actuation per morphing rib;

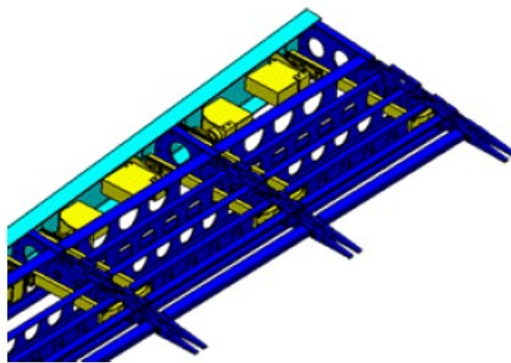• Fault tolerance: continued operation after single-actuator fault.

Fig. 50: Actuation system concept - CIRA, FhG ENAS

A fully-electric ATED reduces classical drawbacks of hydraulic systems and overall complexity, yielding also weight and maintenance benefits. Lack of supply buses, improved torque control, enhanced efficiency, removal of fluid losses and flammable fluids bring to further benefits. A general limit of electromechanic actuators is the possibility of jamming failures that can lead to critical aircraft failure conditions.
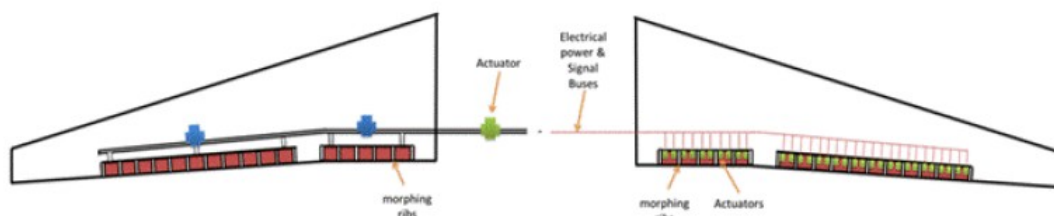

Fig. 51: Comparison b/w conventional shafted (left) and distributed unshafted (right) actuation layouts

The adopted unshafted actuators layout allows achieving further weight savings. This architecture uses both inherent rotation sensors on each actuator and a FBG-based distributed sensor system to synchronize the different elements action and to monitor localized failures. Distributed actuation also enables the motion of individual ribs, enforcing for in- stance twist angle, leading in turn to further features as load alleviation. Starting from the structural design, the actuator electrical arrangement was defined. The connections to the control system hardware, signal conditioning electronics and routing to each actuator was defined. Relative actuator movement with regards to transition times and velocity discrepancies between each rib segment were considered to synchronize each actuator. As a last step, control system components were selected. Resulting scheme is reported in Fig. 52.
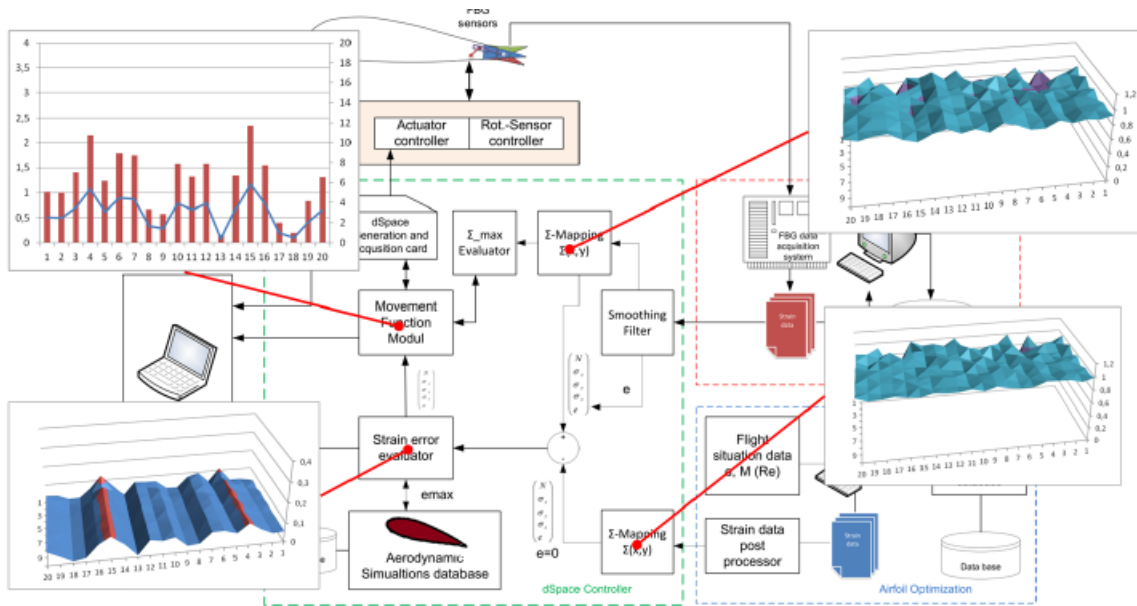

Fig. 52: Control system schematics - CIRA, FhG ENAS

The connection between control system (dSPACE Embedded System) and actuator controller was specifically designed and verified together with the implemented equipment. During the design process, safety and reliability issues were considered. All the potential failure conditions of the actuation kinematics were evaluated by estimating the respective probability of occurrence and the corresponding impact on main aircraft functions that were anyhow preserved.

1.6.4   Sensor System

The use of optical fibers (FO) as sensing elements is facing a bright future. Their properties and capabilities with regard to strain sensing and data transmission, their high endurance and chemically inertness allow application in harsh environments. Many studies and implemented models, during and prior SARISTU progress, validated the feasibility to a wide range of sensing applications. ATED measurement task is to reconstruct its shape from strain data, retrieved from span and chord-wise sections, using tailored solutions

based on FO technologies, Fig. 53. To match the geometrical constraints, two kind of sensorized structures were selected for chord-wise (sensing beam) and span-wise deformations (ribbon tapes).
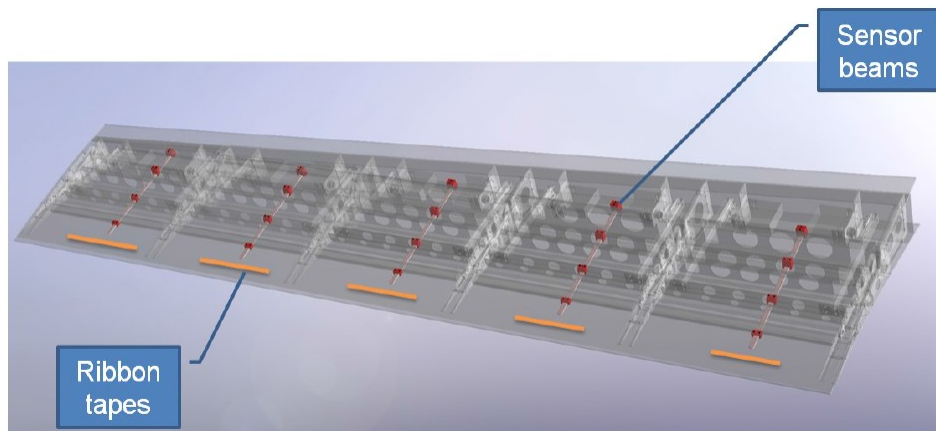

Fig. 53: ATED sensor system layout; span- and chord-wise layout for the 5-bay demonstrator

Technobis Fibre Technologies utilizes a FO based approach for chord wise ATED shape reconstruction by Fibre Bragg Gratings (FBG) implementation. Based on a mechanical device, integrated with an optical fibre transducer, the shape information is translated into strain information and properly modulated. By specific data processing mathematics, these strain values are converted back into an approximation of the produced shape. The resulting error is compliant with the monitoring requirements. The solution is the result of a cooperation among structural (UniNa, CIRA), manufacturing (Aernnova) and sensor (Inasco, Technobis) technology partners.

Spanwise monitoring system design resulted from a co-operation among structural (CIRA), manufacturing (KVE) and sensor (Inasco) technology partners. It consists of very thin and flexible glass fiber reinforced patches called ribbon tape, Fig. 54. Expected span-wise strains are coherent with standard glass FO capabilities so that direct sensing is possible. Ribbon tapes are bonded to the inner side of the metallic tip cover and then connected to form two measurement lines, then drastically reducing the channels number. Suitable structural adjusts permit a safe installation in the structural core.
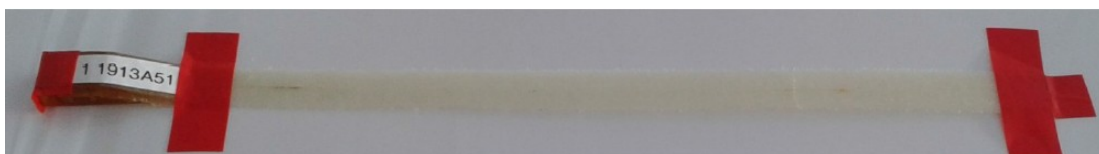

Fig. 54: Ribbon tape incl. connector case

1.7 STRESS AND BUCKLING ANALYSES

Reference dimensions of the most relevant structural components were set according to the results of the preliminary sizing process based on elementary and fast methods, as seen in §1.4. A detailed CAD was then elaborated for the structural layout and used to address stress and buckling verifications based on advanced FE models and analyses.

The detailed modeling of such a complex morphing system involved the proper schematization of all the sub-assemblies: rib and the actuation systems, skin, spars as well as spherical and cylindrical joints, rivets and screws adopted to link parts while assuring required kinematic implementation.

Modeling specifications were compatible with Finite Element Method customary approaches; mesh size and general properties were rationally defined in order to get detailed and reliable distributions of stress and strains (especially around holes) while optimizing the computational time required for each analysis; in Figure 5, some detailed pictures of modelled parts are shown. FE analyses were all carried out in MSC-NASTRAN® environment [18].
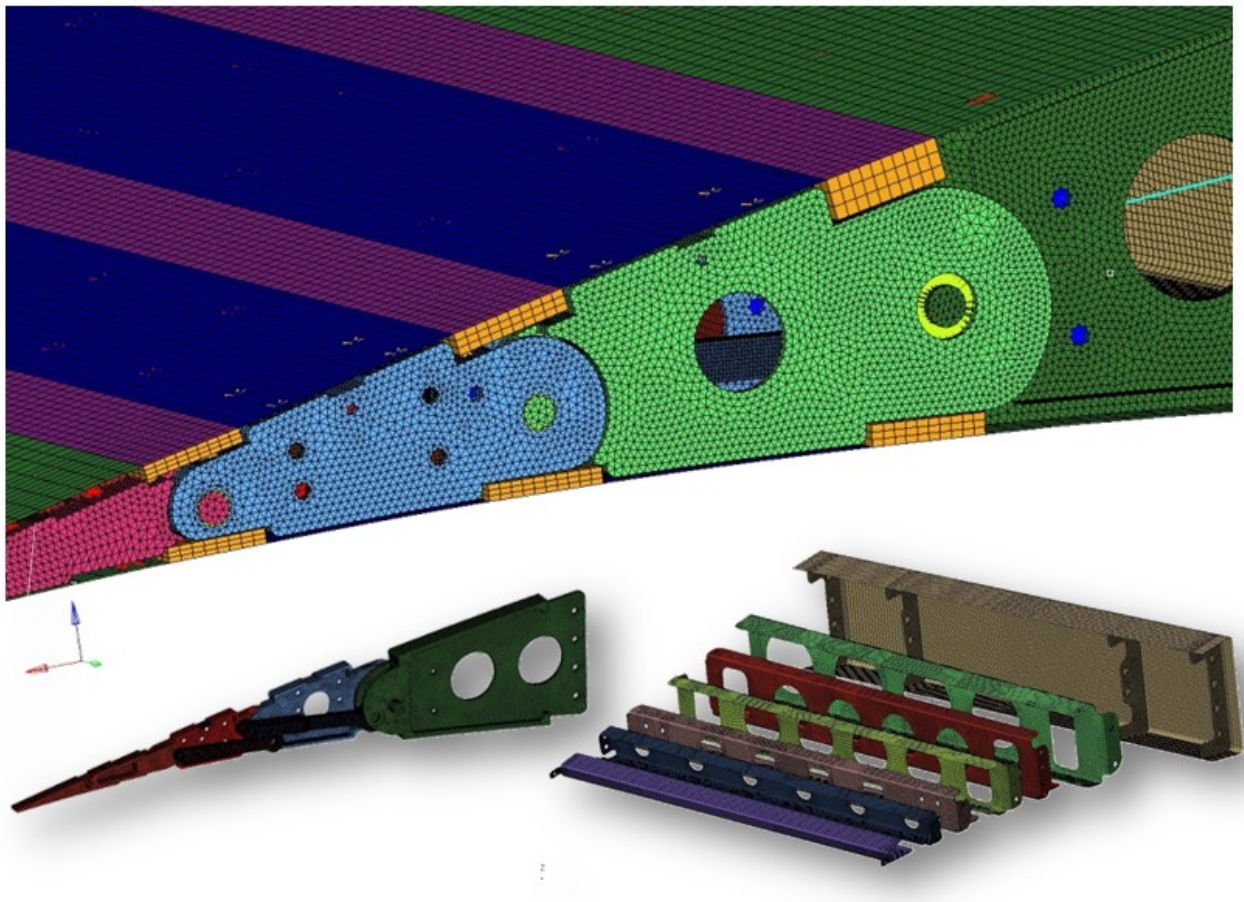

Fig. 55: FEM details: skin-rib interface (up), rib (low, left), spars (low, right)

Linear static analysis under limit load condition was carried out keeping locked the actuator shafts; all grids belonging to the upper and lower skin regions supposed to be joined to wing rear spar, were constrained in all six degrees of freedom. Limit load condition was simulated through piecewise pressure distributions acting on upper (suction) and lower skin (compression); pressure distributions were obtained by referring to the dynamic pressure of 26000 N/m^2 (dive speed, sea-level) and to Cp trends evaluated through inviscid 3D vortex lattice method. In order to be more conservative, no inertial alleviation was taken in account.

Non-linear static analysis was then addressed to evaluate deformation and stress up to ultimate load condition (defined as limit loads multiplied by the reserve factor of 1.5).

As per EASA CS-25 part C, the absence of any permanent deformation (/failure) up to limit (/ultimate) load condition was proven (Table 3).

Reaction forces at fastening holes were evaluated and used to verify both fasteners and lugs at ultimate load. Fasteners were checked with respect to failure in tension, shear and tension combined to shear [16]; lugs were checked with respect to failure by bearing, net section crack, shear-out, transverse and oblique load [16]. Positive safety margins were obtained in correspondence of all performed checks.

The absence of any structural instability up to limit load condition was then proven by means of linear buckling analysis; as shown in Figure 6 the first buckling eigenvalue was found to be safely equal to -3.28 and due to the instability of the fork shaped link belonging to the fourth rib along the spanwise direction.

In Fig. 57 the contour of the elastic displacements induced by limit loads has been reported; in force of a maximum upward displacement of just 15 mm, localized at the tip region, the structural arrangement was considered adequately stiff to withstand aerodynamic loads without significant shape change due to elastic deformations.
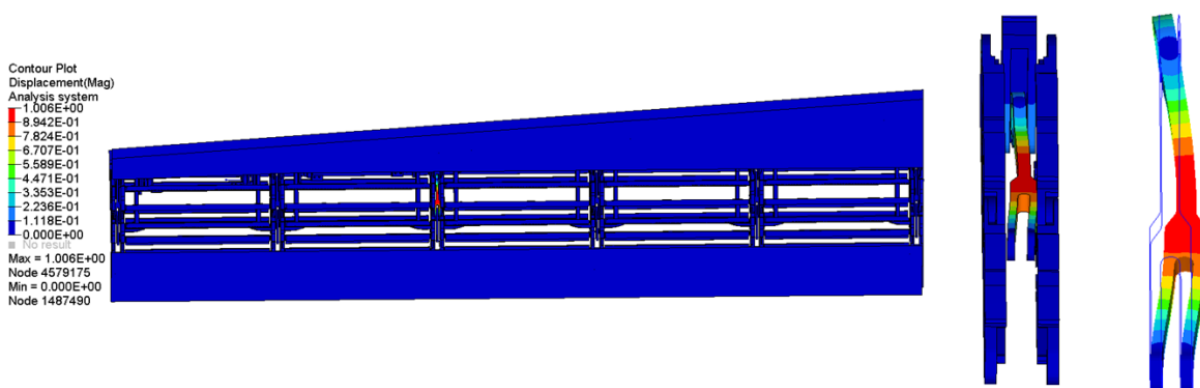

Fig. 56: First buckling eigenvector (eigenvalue equal to -3.28, referred to limit load condition)
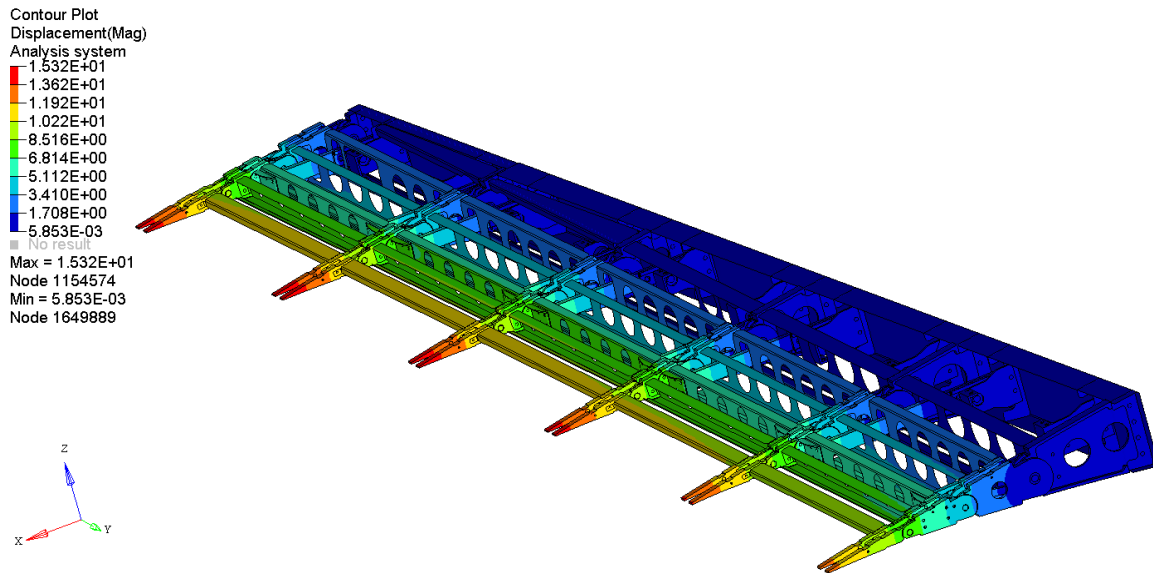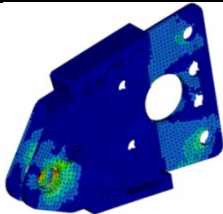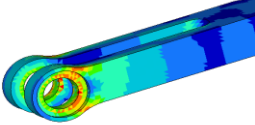
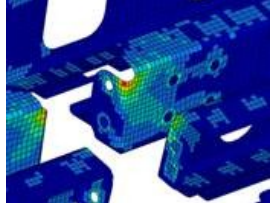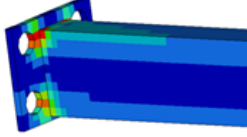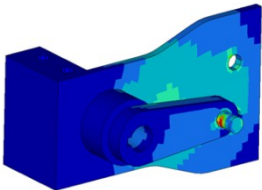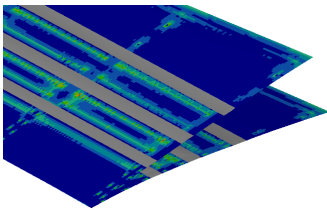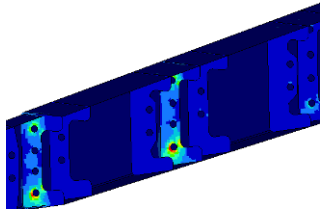**Fig. 57: ATED structure, elastic displacements contour (mm) at limit load condition**

Table 3: Maximum Von Mises stresses (σmax) and safety margins (SM)
at limit (LL) and ultimate loads (UL) (σtY, σtU: yield and failure allowable)

Part	σ_{tY}	$\sigma_{max,LL}$	SM_{LL}	σ_{tU}	$\sigma_{max,UL}$	SM_{UL}	Higher Stress location (red)
Rib	330	262.5	0.26	448	394.4	0.14	
Rod	1150	448.6	1.56	1227	672.9	0.82	
Spar	330	268	0.23	448	401.9	0.11	
Actuator lever	330	166	0.99	448	248.6	0.80	

47

Part	σ_{tY}	$\sigma_{max,LL}$	SM_{LL}	σ_{tU}	$\sigma_{max,UL}$	SM_{UL}	Higher Stress location (red)
Actuator crank	330	50.4	HIGH (>>2)	448	55.4	HIGH (>>2)	
Aluminum skin	330	107	2.08	448	160.8	1.67	
Front spar	330	246	0.34	448	369	0.21	
Skin Foam	---	---	---	1.17	1.13	0.035	

CHAPTER 2:

Experimental characterization of the ATE

This chapter describes briefly the experimental characterization of a "dummy" device, which is a strongly simplified reproduction of an adaptive trailing edge morphing device and was released within the AS02 scenario. Ground vibration tests were performed to evaluate the damping coefficient and provide consistency of a simplified FE model with the dummy itself.

2.1 DUMMIES DESCRIPTION

Four different dummy test articles were designed, manufactured and tested for component and final system verification purposes. These test articles were conceived as a quasi-rigid reproduction of a relevant section of the final prototype, limited spanwise to a 2-bay extension. A steel skeleton was realized to reduce as much as possible any structural elastic coupling effect with the morphing skin during static and dynamic tests. As reported in Fig. 58, the four different test architectures were respectively named as:

- Dummy 1 – Skin over dummy – made of a dummy skeleton and the morphing skin;
- Dummy 2 – Actuators over dummy – made of the dummy skeleton and the servo-rotary actuators;
- Dummy 3 – Control system over dummy – made of the dummy skeleton, the sensor system and the control system;
- Dummy 4 – Control system over skinned dummy – made of the dummy skeleton, the sensor system, the control system and the morphing skin.
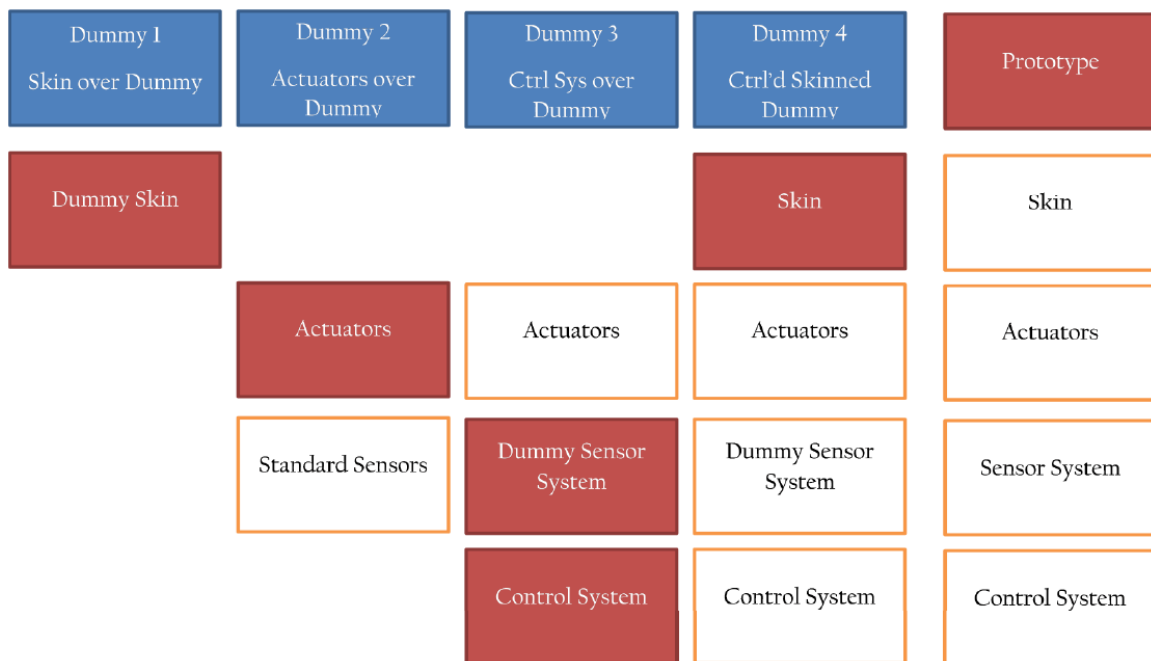

Fig. 58: Dummies logic

The final prototype of the adaptive trailing edge (not yet the final structure, but a complete representation at system level) consists of the aluminum primary structure skeleton, the morphing skin, the actuator system, the control system and the sensor system. This prototype constituted the proof of concept, released within the dedicated work package of SARISTU and was object of wind tunnel test at the University of Naples facilities, as shown in §4.3.1.

2.2 GROUND VIBRATION TESTS

For our purposes the dummy 1 was tested by means of ground vibration tests. Dummy 1 is a strongly simplified reproduction of an adaptive trailing edge morphing device. With respect to the final layout, the following main changes apply:

- Spars: simplified geometrical layout, steel used as constitutive material;
- Skin: no aluminum skin present along the dead box and at the tip of the device;
- Control and sensors systems: not installed.

Experimental tests were carried out to evaluate the damping coefficient. Test article was excited by means of shakers..

A schematic of the acquisition layout and a photo of the test rig is reported in Fig. 59 while a short summary of the observed modes for two different constraint configurations is reported in Table 4. The characteristic damping of the structural system is found to be around 3%, with some exceptions. Enough surprisingly, damping is lower for the free-free configurations, while it reaches its maximum for the clamped configuration. Moreover, a clear distinction can be observed for the free-free modes at low and high frequencies. Damping increases from unit to 3% as the frequency grows up. For higher modes, not reported in the referenced table, damping assesses at 3%. This evidence can be explained as follows: free-free boundary conditions enforce modes that do not involve skin dynamics. In other words, those modes are "encouraged" such that skin is poorly involved. As frequency grows up, the structure is instead forced to stretch and compress the rubber skin, then involving higher dissipation. The same phenomenon holds when the structure is clamped. In that case, in fact, the structure is forced to involve skin dynamics, since the very first eigenvalue, and the damping is assessed from the very first beginning to 3%.
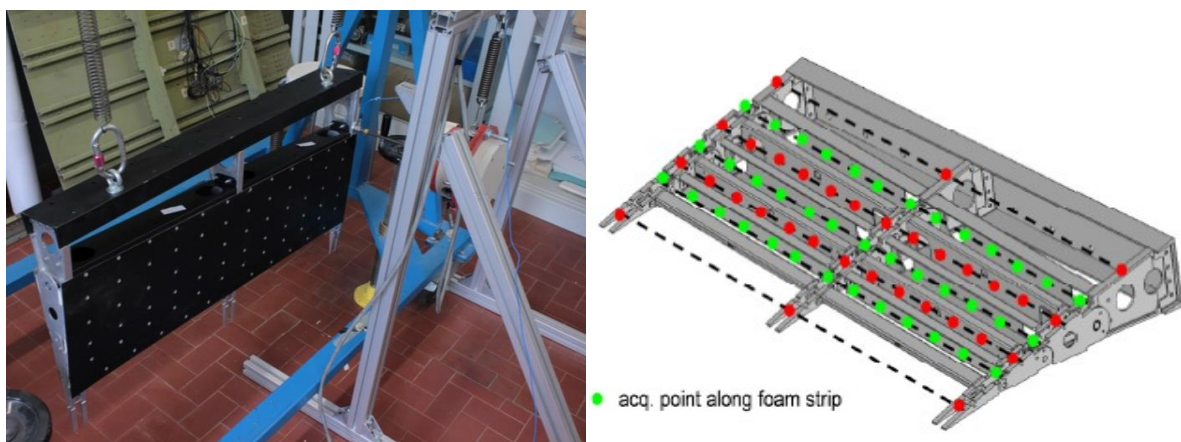

Fig. 59: Test article and map of the acquisition points

Table 4: modal results summary

Boundary Condition	Mode type	Frequency (Hz)	Damping (%)
Free-Free	-	-	-
	Torsion	59,0	0,8
	Rib antiphase bending	80,0	0,3
	Rib in-phase bending	125,6	1,8
Clamped	Kinematic mode	35,0	3,0
	Torsion	65,0	2,9
	Rib antiphase bending	145,0	3,5
	Rib in-phase bending	214,0	2,3

The adaptive trailing edge concept herein presented is derived by combining classical and new technologies, all assembled into a new product. In this way, there are well assessed components (the sensor system, the control system, the actuator system and the structural system), combined with a more innovative product, like the morphing skin. While the classical components are not reasonably going to give rise to complex issues on the maintenance and the reliability (classical kinematic, actuator and sensor chain models may be referred to) the innovative skin should be imagined to undergo a long testing period in order to characterize its behavior outside of the standard design domain, above all with respect to fatigue and aging aspects. From the workability point of view, maturation of this latter technology is necessary to come to a final product of industrial relevance. Furthermore, because the active camber deformation devices are largely distributed, reduction processes should be properly targeted. This would in the end result with a necessary update of the standard design processes and codes, to face with this new challenge.

Skin influences the introduced adaptive trailing edge dynamics with three contributions, namely mass, damping and stiffness, none of them negligible with respect to the original system ones. The ATED, has in itself a relevant complication linked to the augmented degrees of freedoms, directly related to its morphing capability that can in turn lead to aeroelastic instabilities. In fact, namely larger degrees of freedom bring to a higher modal density, together with a more extensive and complex coupling among the eigenmodes. Indeed, the structural system, as it has been conceived, is free to move, unless the motor chain is installed. The insertion of the skin causes the system to be stable, because of the stiffness contribution of the skin.

Unfortunately, the increase of mass (a relevant percentage of the whole architecture) leads also to a further increment of the modal density, therefore complicating the aeroelastic behavior, in principle. Intrinsic high damping level strongly balances this drawback because of two more concurrent aspects. First, it increase the system capability to dissipate energy and, secondly, attenuates the characteristics of the different modes by flattening the FRF. In the preliminary experimental investigations, carried out on simplified mock-ups of the final prototype and shown in this paper, this value was estimated in several percentage units, in line with the expectations.

2.3 SIMPLIFIED FINITE ELEMENT MODEL

A FE model was created of the dummy 1, implementing all the simplifications assumed for the dummies also from a numerical point of view, moreover keeping the model very light computationally speaking.

2D elements were used for spars, rib blocks and skin. Hinges were modeled as beams with released torsional degree of freedom; links were simplified with rod elements. Fasteners between skin model (Fig. 62) and TE structure (Fig. 60) were modeled through beams.

Table 5: Material properties for modal analysis

	Aluminium 2024-T3	Steel 17-4 PH	Hyperelastic	Hyperfoam
Density (Tonn/mm^3)	2.78E-09	7.80E-09	1.00E-11	1.00E-11
E (MPa)	70000	210000	1.7	$\approx$3.7
F_{tu} (MPa)	448	1227		1.17
F_{ty} (MPa)	330	1150		
F_{bru} (MPa)	730			
F_{bry} (MPa)	517			

Properties of the so-called "hyperelastic" and "hyperfoam" materials were set to properly match the experimental results.
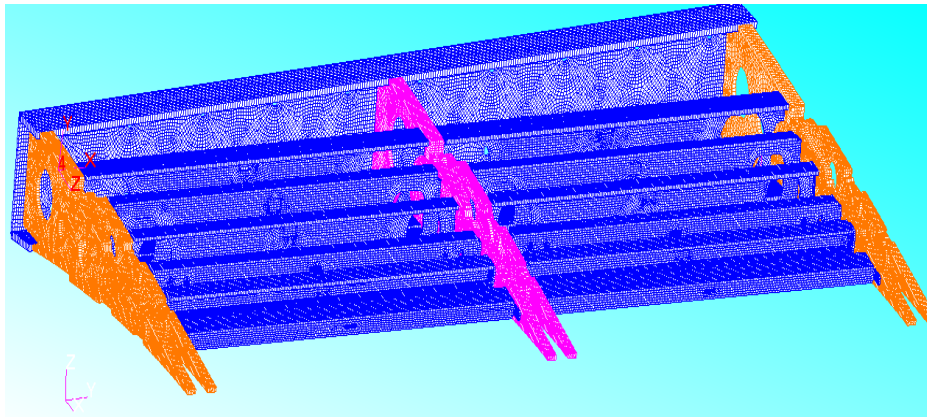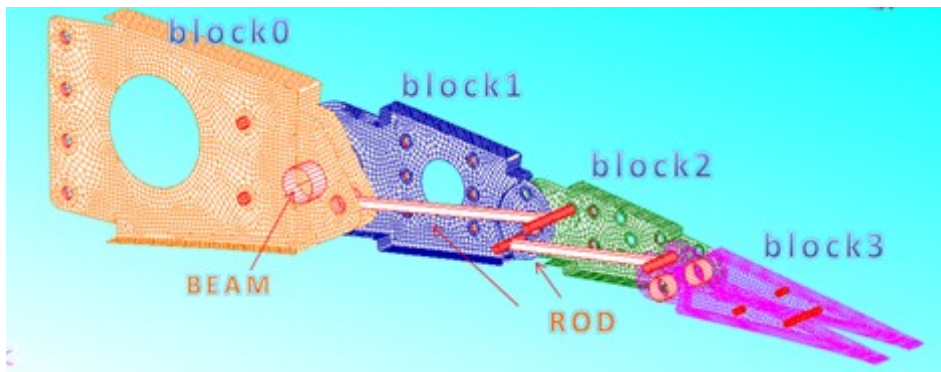

Fig. 60: Dummy 1 FE model.
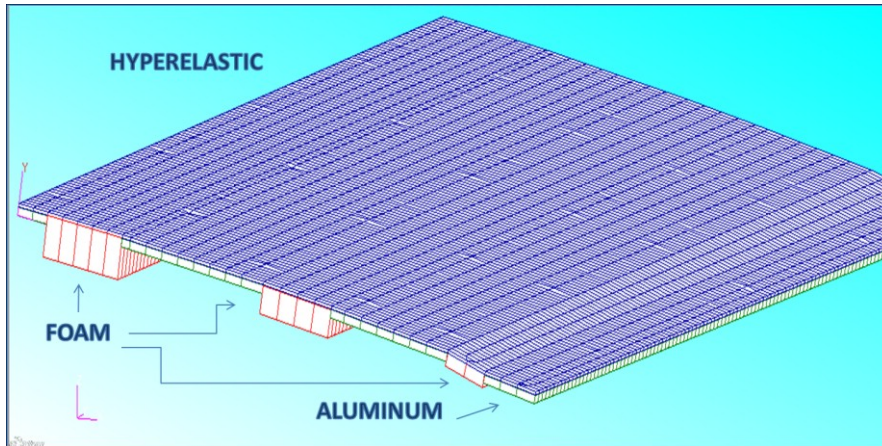
Fig. 61: Rib parts and connections.

Fig. 62: Skin model

2.4 MODAL ANALYSIS OUTCOMES

Modal analyses were carried out in clamped conditions, since we have already seen in §2.1 that free-free boundary conditions enforce modes that do not involve skin dynamics, while main purpose of such analysis is the identification of the skin mechanical properties. Results are summarized inTable 6.

First three modes were also in shown in Fig. 63 - Fig. 65.

Table 6: Modal analysis results - clamped condition

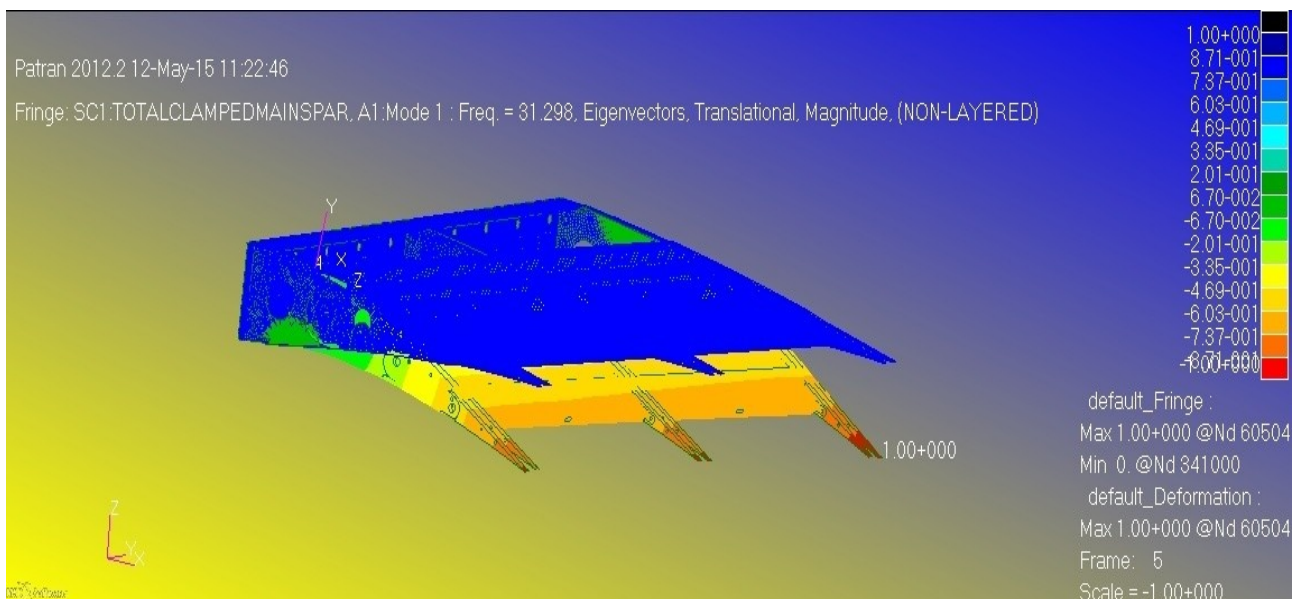| MODE N.	EIGENVALUE	FREQUENCIES
1	3,87E+04	3,13E+01
2	5,72E+04	3,81E+01
3	1,68E+05	6,52E+01
4	8,50E+05	1,47E+02
5	1,07E+06	1,65E+02
6	1,13E+06	1,69E+02
7	2,08E+06	2,29E+02
8	2,51E+06	2,52E+02

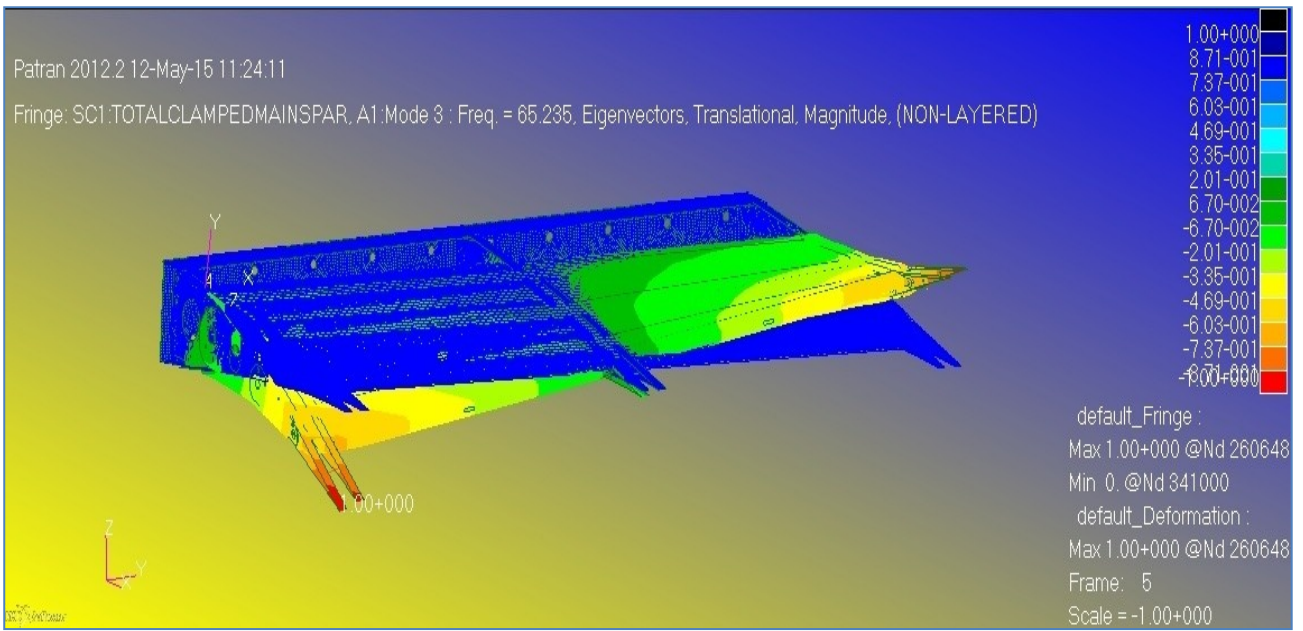**Fig. 63: FEM modal analysis - kinematic mode**

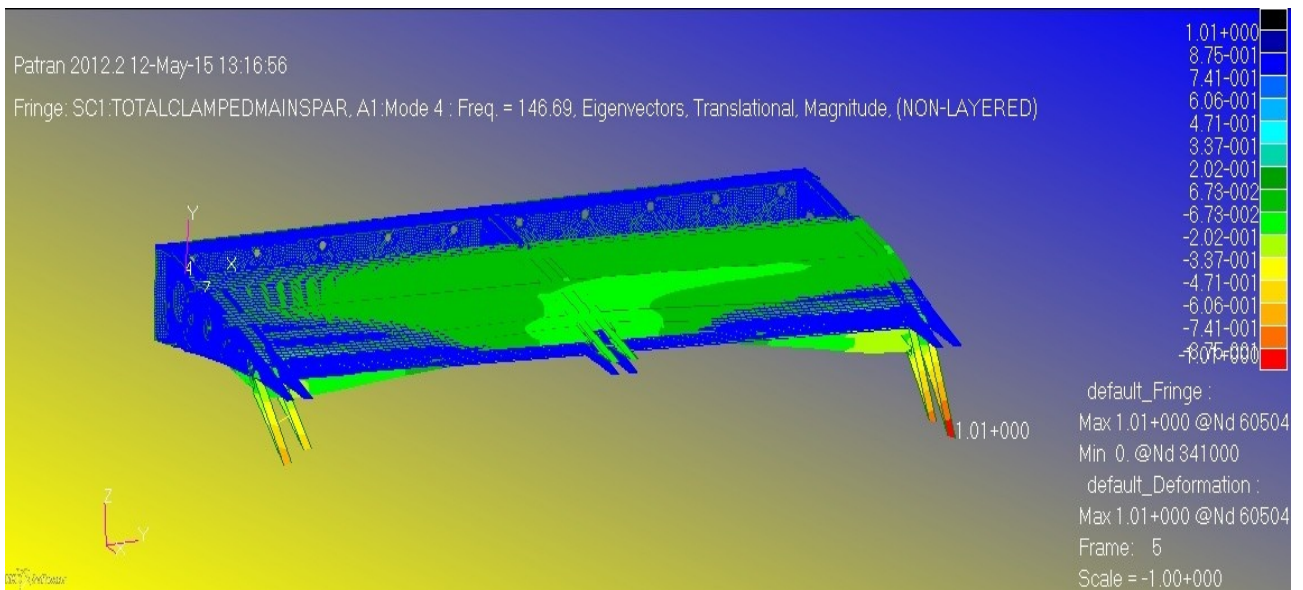**Fig. 64: FEM modal analysis - Torsion mode.**

Fig. 65: FEM modal analysis - Anti-phase bending mode.

2.5 DATA CORRELATION

The results of experimental tests and FE modal analysis were compared and three characteristic modal behaviors were identified:

- kinematic mode.

- torsion mode.

- Anti-phase bending mode.

The frequencies of these modes, from GVT and FE modal analyses, were reported in Table 7. The very good correlation was shown by means of a scattering diagram in Fig. 66. The frequency deviation from the experimental one can be seen as the deviation from the bisector of the plane.

Table 7: Experimental vs FE modal analysis outcomes

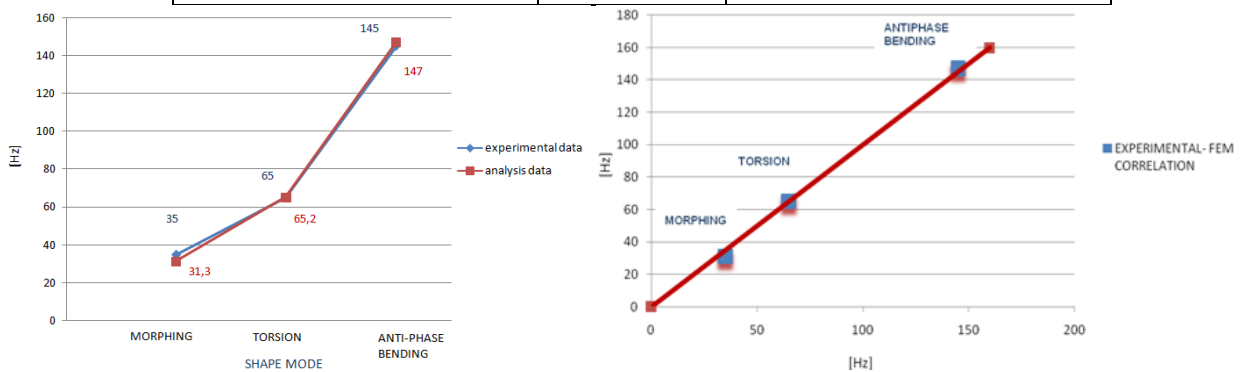| MODE	GVT RESULTS	FE MODAL ANALYSIS RESULTS
Kinematic mode / Morphing	35 Hz	31.3 Hz
Torsion	65 Hz	65.2 Hz
Antiphase bending	145 Hz	147 Hz

**Fig. 66: Experimental - FEM correlation.**

CHAPTER 3:

ATE Aeroelastic Stability investigation

This chapter addresses the aeroelastic stability investigation performed on the ATE. Rational approaches were implemented in order to simulate the effects induced by variations of trailing edge actuators' stiffness on the aeroelastic behavior of the wing also in correspondence of several failure cases. Reliable aeroelastic models and advanced computational strategies were properly implemented to enable fast flutter analyses covering several configuration cases in terms of structural system failures.

3.1 STRUCTURAL MODEL

Wing system structural model was generated referring to the stick-equivalent representation already presented in §1.5.1.

Stiffness and inertial distributions were also evaluated for the trailing edge according to the numerical model presented in §1.7.
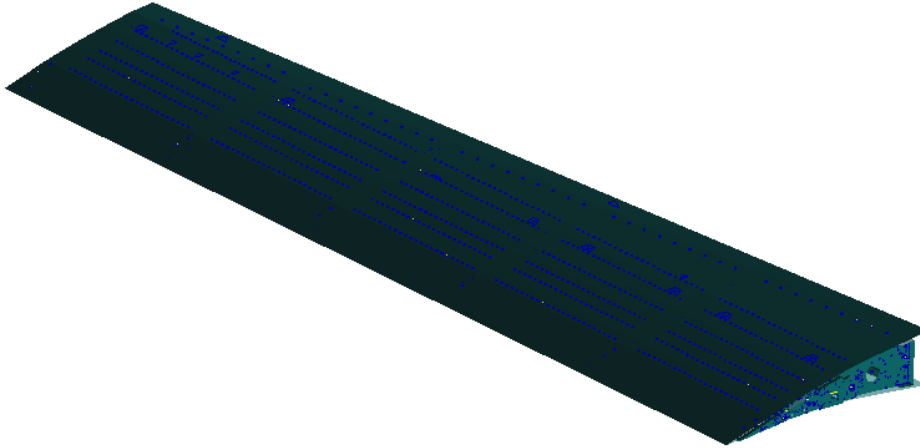
3.2 STIFFNESS DISTRIBUTIONS

In this sub-section a procedure for determination of stiffness properties is described. By working on the ATE FE model, the position of the Block 0 EA was preliminarily determined.

The following procedure was adopted:

1. A guess position of the axis was considered;

2. A reference system having the y-axis aligned with the elastic axis was created. Z-axis was taken normal to the wing plane, origin was located at the RIB 1 station (Sys1);

3. Nodes were added to FE model in correspondence of the intersection points between the elastic axis and ribs' planes;

4. At each rib station, RBE2 elements were generated to slave the nodes of the rib boundary to the node at the intersection between the rib plane and the (imposed) elastic axis;

5. An arbitrary torque M_T, was applied along the elastic axis and in correspondence of its intersection with the plane of the rib located at wing tip. The master node on the rib plane at the wing root was constrained in all degrees of freedom;

6. Master nodes' displacements along z (Dz) and rotations around y axis (Ry) of the reference system were evaluated through linear static FE analysis [3]. The ratio l = Dz/Ry indicated the offset of the section shear centre from the local master node, laying on the (supposed) elastic axis.;

7   From the plot of the above mentioned offsets versus y-coordinate, a linear regression was obtained thus getting a new position of the elastic axis.

Iterations occurred until an acceptable regression coefficient was reached ($R^2 \approx 1$). Stiffness distributions along the span of the box of blocks 0, to be applied to the equivalent beam, were determined with reference to the Model of the ATE (modified according to the actions described at points 3 and 4) and by constraining the first node of the (assessed) elastic axis and by applying a known load value at the tip (last node of the elastic axis).

- A Torque MT , about the elastic axis, yielded rotations of master nodes around y-axis (=elastic axis, Sys1) . The derivative of these Rotations with respect to y coordinate was evaluated and the torsional stiffness was obtained according to the following equation:

$$GJ(y) = \frac{M_T}{\dfrac{dR_y(y)}{dy}}$$

- A Bending moment, about X (and Z) axis, yielded rotations of master nodes around X (and Z)-axis. The derivative of these Rotations with respect to y coordinate was evaluated and the bending stiffness was obtained according to the following equation:

$$EI_{min}(y) = \frac{BM_x}{\dfrac{dR_X(y)}{dy}}$$

$$EI_{max}(y) = \frac{BM_z}{\dfrac{dR_Z(y)}{dy}}$$

- A Normal force, aligned to the elastic axis, produced displacements of master nodes along y-axis (=elastic axis). The derivative of these displacements with respect to y coordinate was evaluated and the axial stiffness was obtained according to the following equation:

$$EA(y) = \frac{F_y}{\dfrac{dD_Y(y)}{dy}}$$

For the movable part (B1, B2 and B3) stiffness properties were evaluated with respect to the main hinge line of the each sub-system instead of the elastic axis.

3.2.1   Block 0

From now on, the term "block" will address the structure sub-assy made up by the rib homolog blocks and the spars linking them in a closed box. Therefore, "Block 0" indicates the region in Fig. 67.
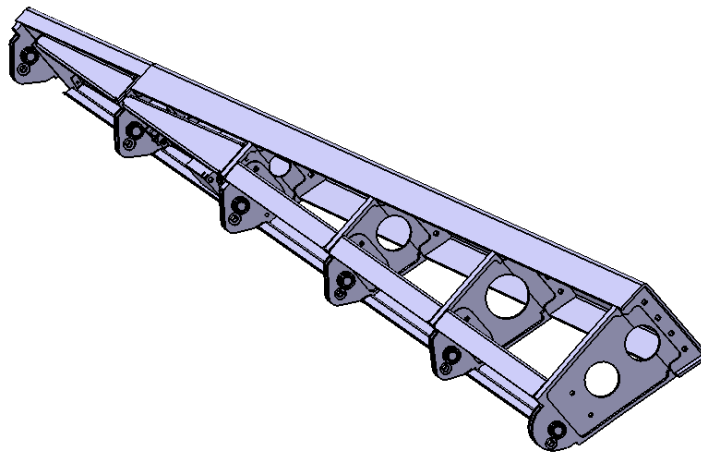

Fig. 67: Block 0 box.

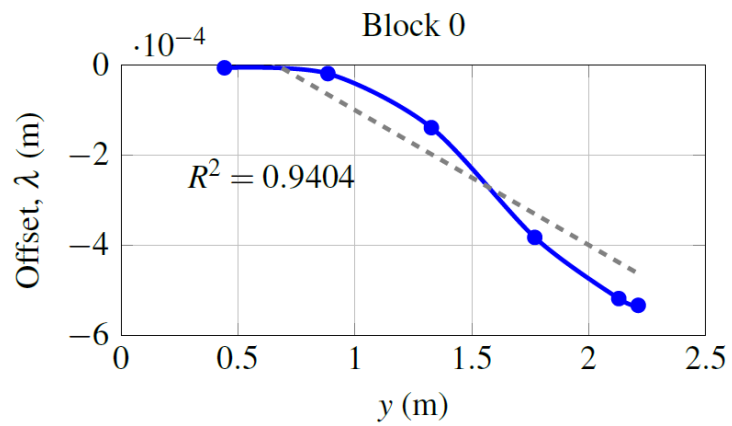As already seen in §1.5.2 for wing box and winglet stiffness determinations,

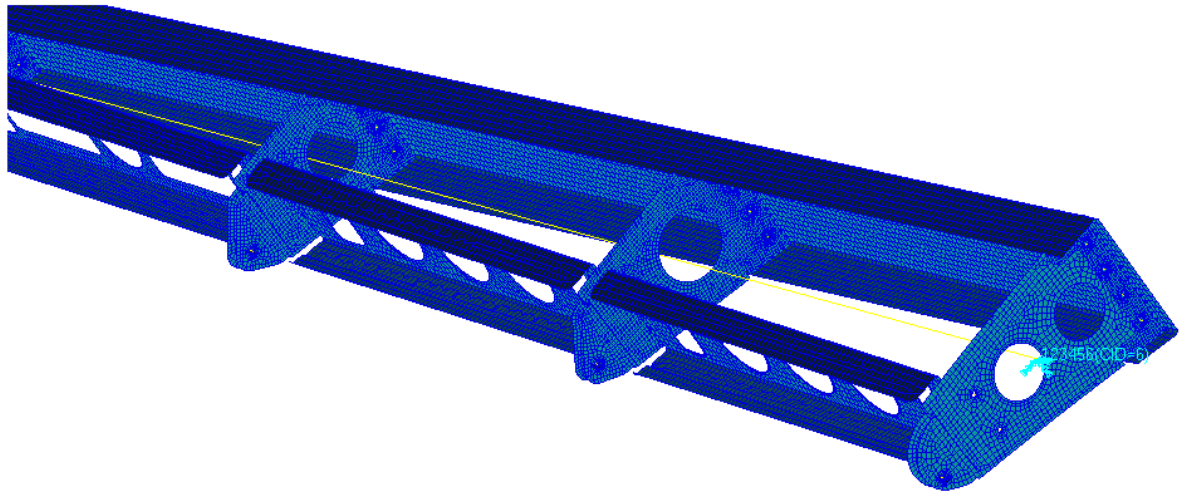**Fig. 68: block zero box elastic axis determination.**

Fig. 69: detail of block zero FE model (MPCs hidden)

The stiffness properties were obtained using a polynomial interpolation limited to the first or second order. In each figure below, the stiffness distributions of the demonstrator and those extrapolated for the investigated area will be shown.
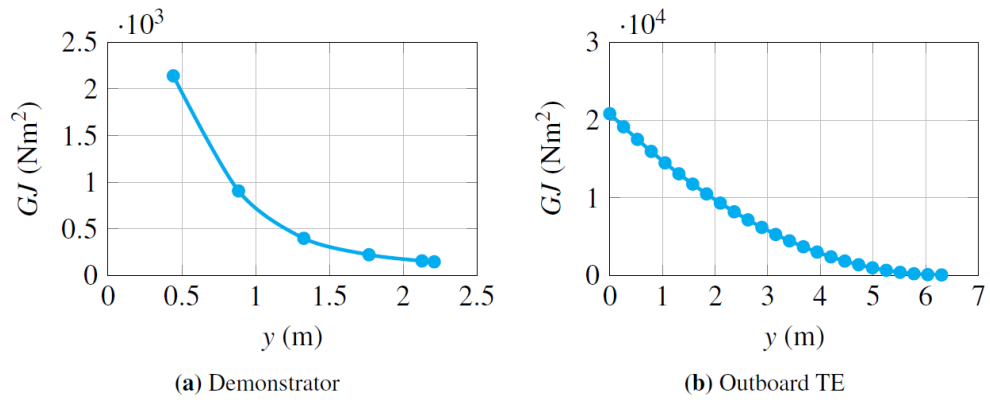
(a) Demonstrator

(b) Outboard TE

Fig. 70: block 0 torsional stiffness distributions.

(a) Demonstrator

(b) Outboard TE
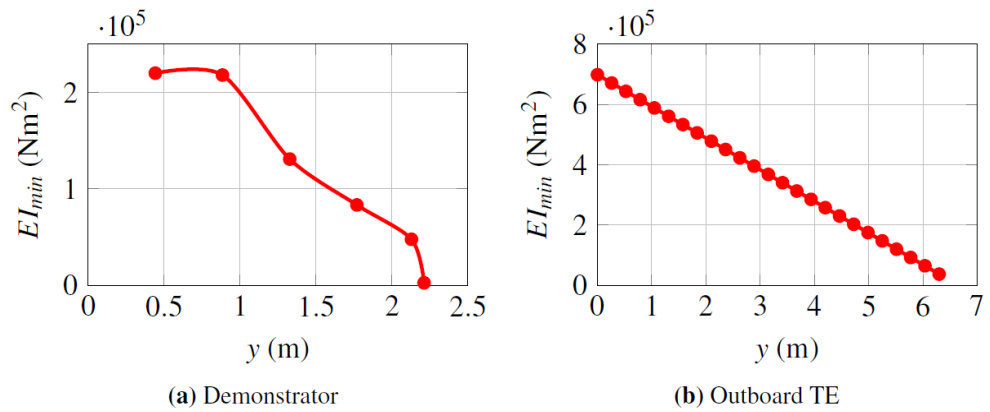
Fig. 71:block 0 vertical bending stiffness distributions.

(a) Demonstrator

(b) Outboard TE
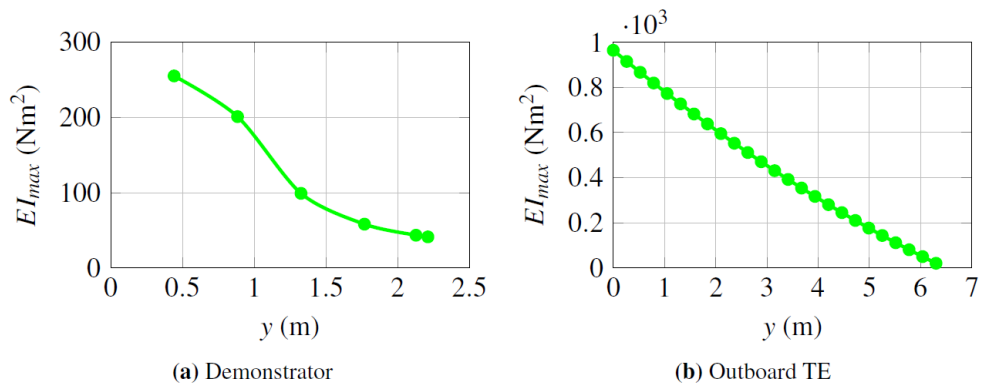
Fig. 72: block 0 Fore & aft bending stiffness distributions.

(a) Demonstrator   **(b)** Outboard TE

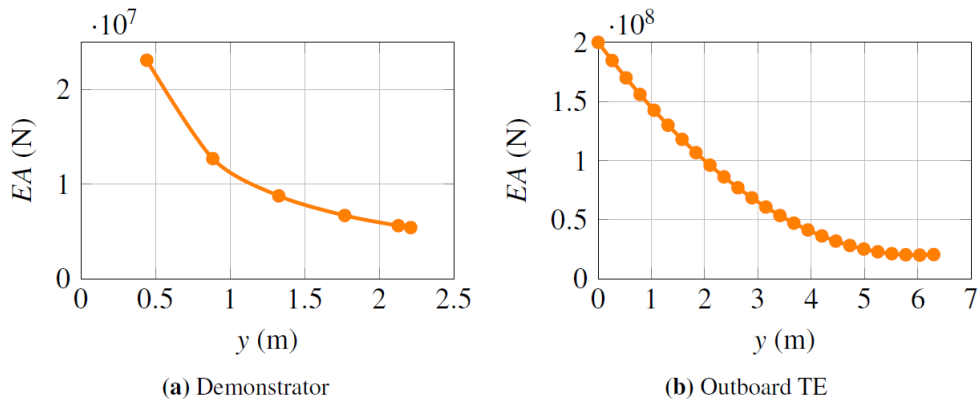**Fig. 73: block 0 axial stiffness distributions.**

The Block 0 is tapered; in order to take into account this variation in the weight estimation, the "chords rule" is applied. It is a homothetic transformation that provides a scale factor for the adjacent bay weight estimation.
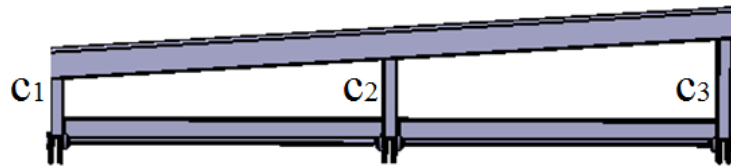

Fig. 74: chords rule parameters.

The scale factor is calculated using the following equation:

$$S.F.= \frac{c_3 + c_2}{c_2 + c_1} = \frac{0.168 + 0.137}{0.137 + 0.112} \approx 1.225$$

This equivalence has been verified for all the bays. The span-wise thickness variation is very slight so it was neglected. In such a way the inertial properties, masses and moments of inertia, were determined. The mass of Block 0 , for both the demonstrator and the outboard region of the wing were summarized in Table 8.

Table 8: Mass properties, Block 0

	Mass [Kg]
Demonstrator	≈16.30
Outboard wing domain	≈128.5

3.2.2 Traiing edge movable parts

The trailing edge movable part was considered equal per each bay along the span (airfoil thickness variation is neglected) so the bays have been simply reconstructed by offsetting the model available for the demonstrator area.

The following paragraphs enclose the extrapolated results for each block of trailing edge movable part. In each figure below, the stiffness distributions of the demonstrator and those extrapolated for the investigated area were shown.

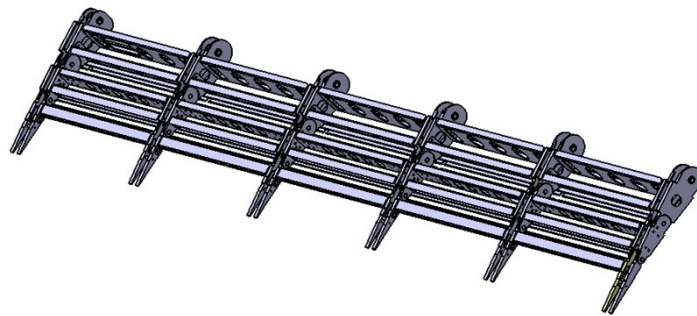A geometric view of Blocks 1,2 and 3 is represented in Fig. 75.

Fig. 75: Trailing edge movable parts

Block 1

The stiffness properties were obtained using a polynomial interpolation limited to the first or second order.

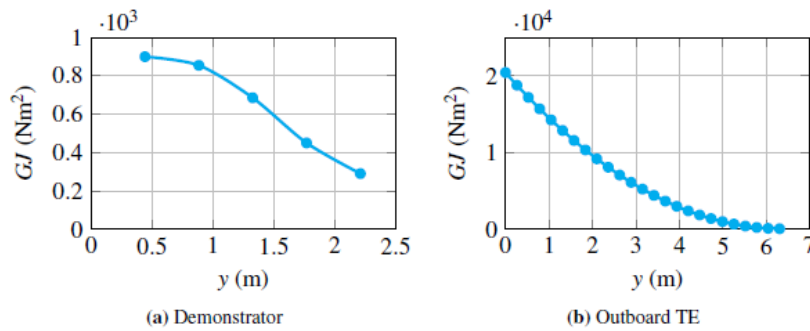The following figures show the stiffness distributions in spanwise direction for the block 1.

Fig. 76: Torsional stiffness, Block 1

Fig. 77: Vertical bending stiffness, Block 1

(a) Demonstrator   (b) Outboard TE

Fig. 78: Fore & aft bending stiffness, Block 1

(a) Demonstrator   (b) Outboard TE

Fig. 79: Axial stiffness, Block 1

The mass of Block 1 both the demonstrator that the outboard region is indicated in Table 9.

Table 9: Mass properties, Block 1

	Mass [Kg]
Demonstrator	≈ 4.80
Outboard wing domain	≈ 13.5

Block 2

The following figures show the stiffness distributions in spanwise direction for the block 2.

(a) Demonstrator   (b) Outboard TE

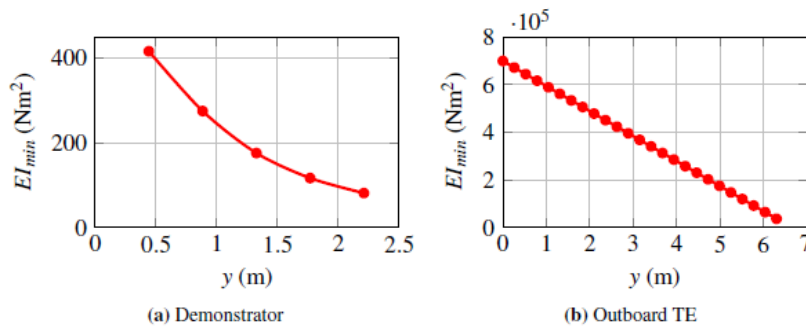**Fig. 80: Torsional stiffness, Block 2**
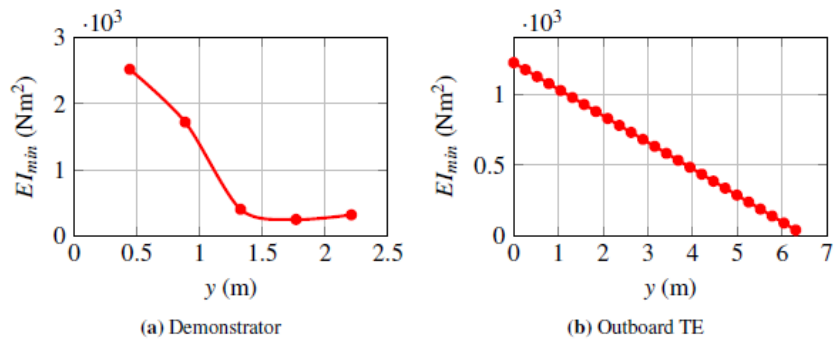
Fig. 81: Vertical bending stiffness, Block 2
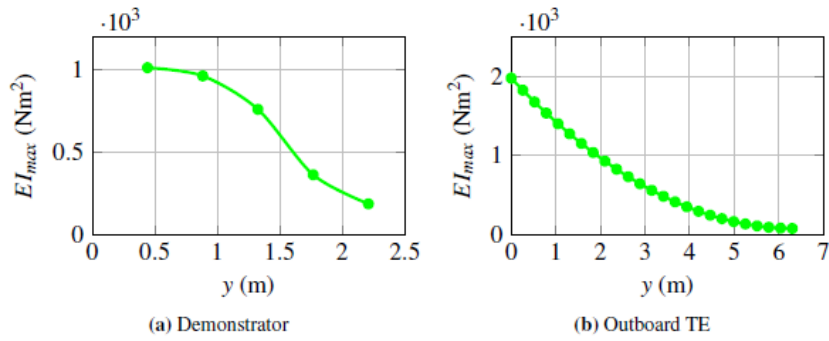
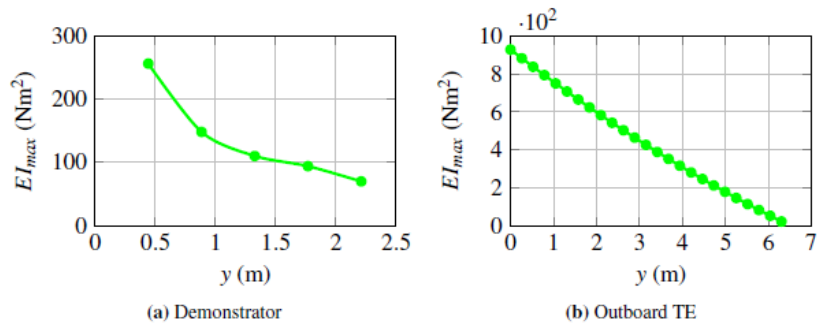**Fig. 82: Fore & Aft bending stiffness, Block 2**
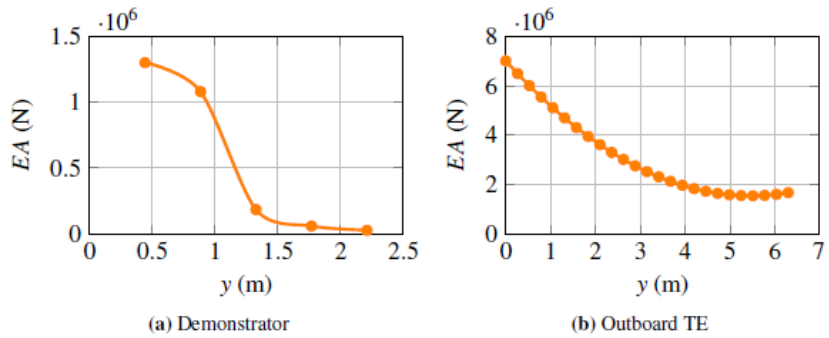
Fig. 83: Axial stiffness, Block 2

The mass of Block 2 for demonstrator and outboard region was indicated in Table 10.

Table 10: Mass properties, Block 2

	Mass [Kg]
Demonstrator	≈4.00
Outboard wing domain	≈11.2

Block 3

The following figures show the stiffness distributions in spanwise direction for the block 3.
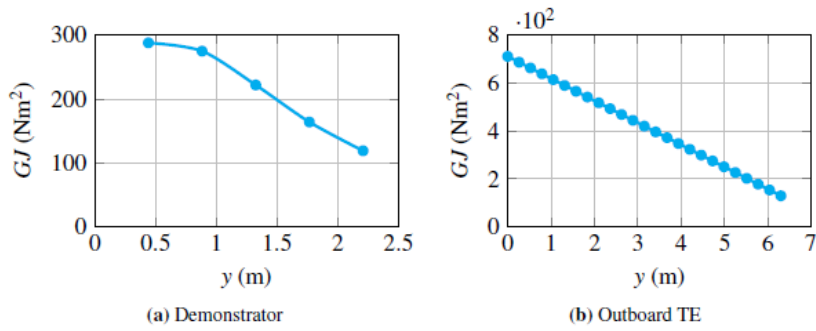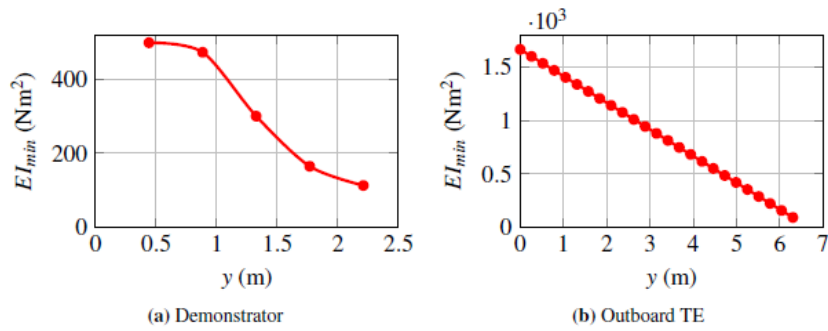
(a) Demonstrator   **(b)** Outboard TE

Fig. 84: Torsional stiffness, Block 3

(a) Demonstrator   **(b)** Outboard TE

Fig. 85: Vertical bending stiffness, Block 3

(a) Demonstrator   **(b)** Outboard TE

Fig. 86: Fore & Aft bending stiffness, Block 3
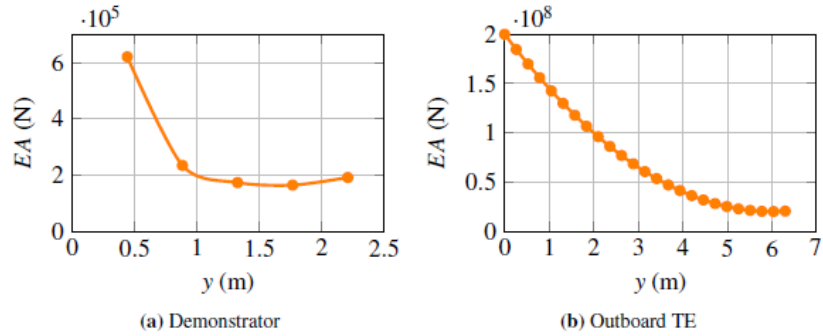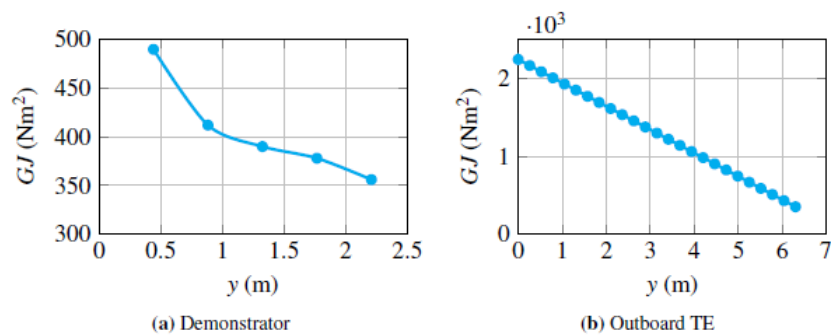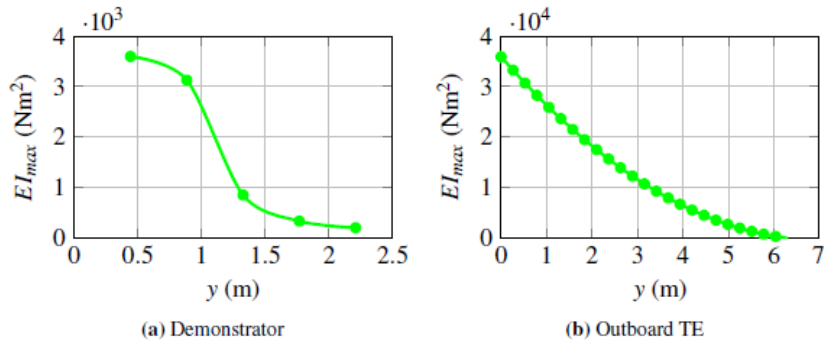

(a) Demonstrator   **(b)** Outboard TE
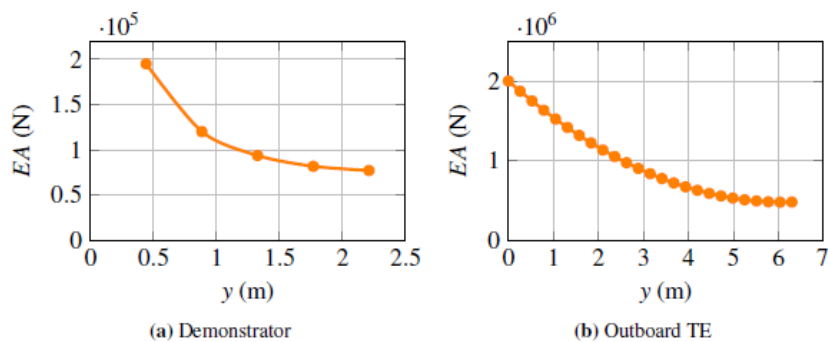
Fig. 87: Axial stiffness, Block 3

The mass of Block 3 for demonstrator and outboard region was indicated in Table 11.

Table 11: Mass properties, Block 3

	Mass [Kg]
Demonstrator	≈6.10
Outboard wing domain	≈17.1

## 3.3 STICK MODEL INTEGRATION

The structural model already developed in §1.5.1 was modified in order to accommodate the stick model of the adaptive trailing edge. It is made up by four beams: the first, to be linked to the elastic axis of the wing by means of rigid elements, with the stiffness properties of the ATE Block 0; the others at the hinge lines between movable blocks.

The harmonic frequency was set by manipulating the stiffness of the torsional spring used to simulate movable trailing edge actuators; in order to get a given frequency f , the torsional stiffness Ka of the actuators with respect to Block 1 hinge-line was imposed equal to:

$$K_a = (2\pi \cdot f)^2 \cdot I$$

Where *I* stands for the inertia of the movable trailing edge around its hinge line.

The morphing frequency was measured experimentally and results about 30 Hz, therefore the generalized stiffness resulted:

$$K_G = (2\pi \cdot 30)^2 \cdot 0.6213 = 22075\frac{N}{m}$$

In which the inertia corresponds to generalized mass of the fundamental mode:

$$M_G = 0.6213 \, Kg \cdot m^2$$

The local stiffness is given by considering the layout series of the connections:

$$\sum_{i=1}^{15} \frac{1}{K_i} \approx \frac{1}{K_G}$$

By placing $K_i = K, \forall i$, it was possible to build the geared elasto-kinematic matrix.

Adjacent blocks have geared rotations due to the single-degree-of-freedom system layout. Therefore, connections between the stick beam models of each block were made by DMIG elements built according to the geared elasto-kinematic matrix description, hereinafter reported.
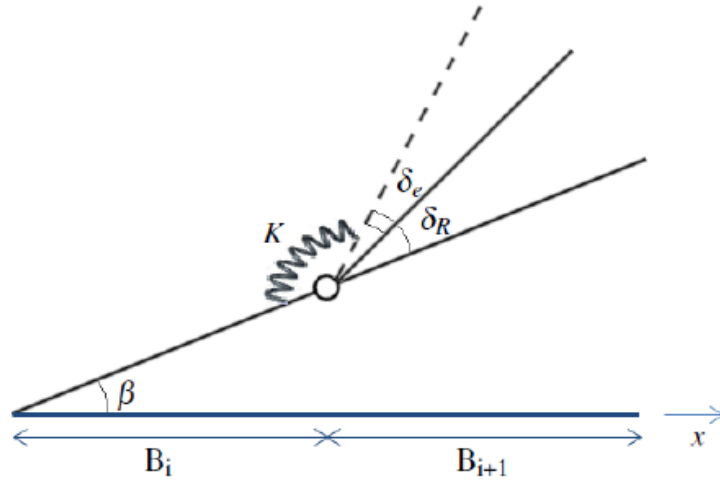
Fig. 88: Sketch of the elastic geared connection

Where:

- β is the block B_i rotation;
- δ_R is the rigid rotation of B_{i+1} with respect to B_i;
- $N = \dfrac{\delta_R}{\beta}$ is the geared ratio of B_{i+1} with respect to B_i;
- δ_E is the elastic rotation of B_{i+1} with respect to B_i;

The total rotation δ $\;of\; B_{i+1}$ with respect to x axis is equal to:

$$\delta = \beta + \delta_R + \delta_E$$

The spring K deformation energy is:

$$u = \frac{1}{2}K\delta_E^2$$

Therefore, we can express:

$$\delta_E = \delta - \beta - \delta_R = \delta - \beta - N\beta = \delta - \beta(1 + N)$$

$$u = \frac{1}{2}K[\delta - \beta(1 + N)]^2 = \frac{1}{2}K\delta^2 - K\delta\beta(1 + N) + \frac{1}{2}K\beta^2(1 + N)^2$$

From which stiffness matrix of the elastic geared connection is obtained:

$$\begin{bmatrix} \dfrac{\partial u}{\partial \beta} \\ \dfrac{\partial u}{\partial \delta} \end{bmatrix} = \begin{bmatrix} (1 + N) & -(1 + N) \\ -(1 + N) & 1 \end{bmatrix}\begin{bmatrix} \beta \\ \delta \end{bmatrix}$$

Fig. 89 shows the definitive structural model of the wing with the implemented modeling of the Adaptive Trailing Edge.
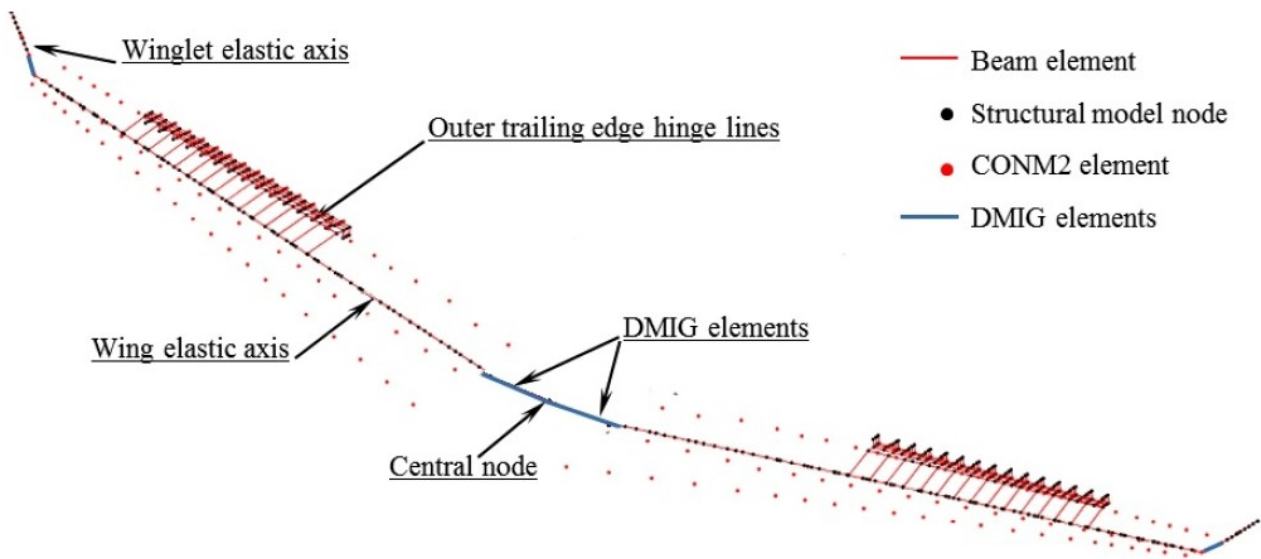
Fig. 89: Equivalent structural model of the wing

Matrices of unsteady aerodynamic influence coefficients (AIC) [20] were evaluated by means of doublet lattice method (DLM). The aerodynamic lattice of the wing was already available from the trade-off analysis described in §1.5.2 where it was generated by properly meshing the middle wing plane through 8 macro-panels for each side of the wing; macro-panels were further meshed into elementary boxes; higher boxes density was considered for the movable trailing edge and to assure mesh congruency with the structural hinged blocks of the movable trailing edge.

Modal displacements at the centre of each aerodynamic box were obtained by means of linear spline functions [20] attached to support-nodes of the structural model.

Fig. 90 shows the overlap of the aerodynamic and the structural models.
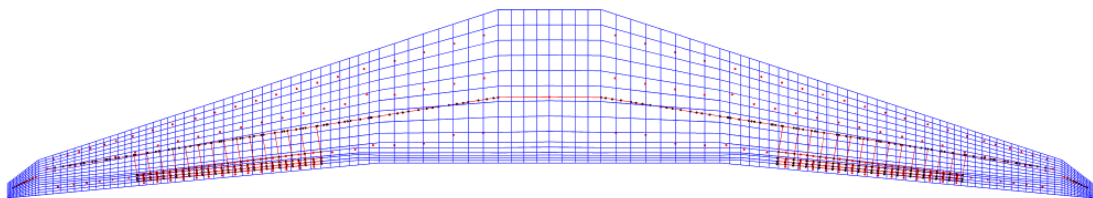
Fig. 90: aeroelastic model

3.4 AEROELASTIC ANALYSIS

The overlap of structural and aerodynamic models provided the aeroelastic scheme to study the wing dynamic behavior. Several cases of flutter analyses, by means of Sandy© code, were investigated in order to meet the safety requirements imposed by the applicable aviation regulations [27]:

- System fully operative;

- System in the failure condition.

3.4.1 *Assumption and investigated cases*

Flutter analyses were carried out under the following assumptions:

- PK-continuation method with rationalization of generalized aerodynamic forces [20] for
the evaluation of modal frequencies and damping trends versus flight speed;

- Theoretical elastic modes association in the frequency range 0 Hz - 50 Hz (elastic modes being
  pertinent to free-free aircraft, with only plunge and roll motions allowed);

- Modal damping (conservatively) equal to 0.01 for all the elastic modes;

- Sea-level altitude, flight speed range 0 - 250 m/s (> 1:15 VD, VD ≈ 200 m/s [27]).

The condition f = 0 Hz was taken in account to simulate actuators failure; in such a case the movable trailing edge harmonic obviously coincides with its fundamental (free rotation around the hinge line). In the following figures the fundamental mode shapes of trailing edge are shown. The morphing fundamental mode is a rigid body motion in the assumption of actuators failure.

Fig. 91 represents the outer right trailing edge symmetric harmonic assuming to release the Block 1 from the fixed system.

In this case a rigid mode that evolves according to a given geared ratio of trailing edge is identified: this ratio grows from Block 1 to Block 3.
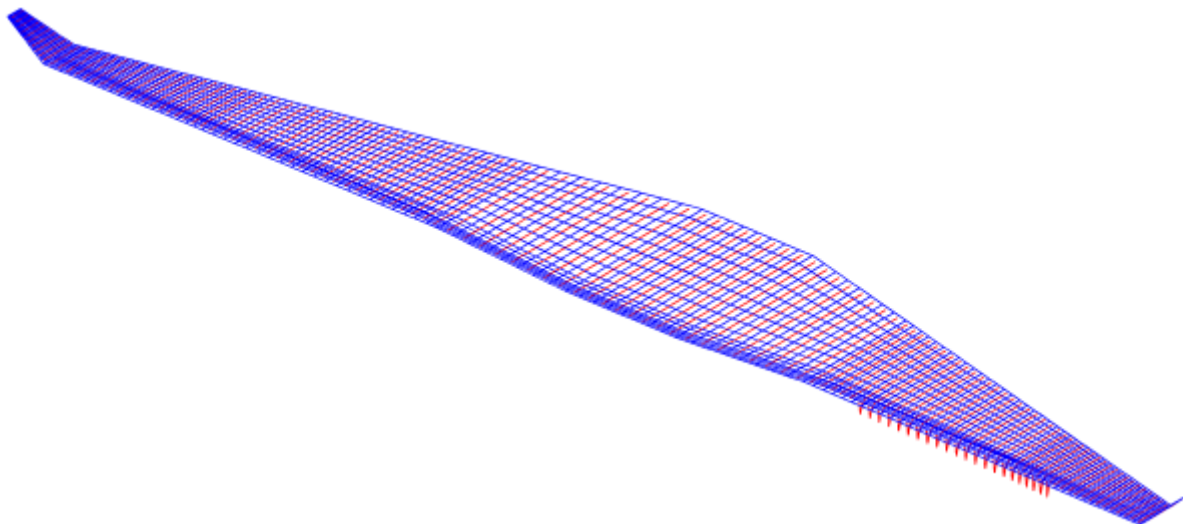
Fig. 91: Outer trailing edge harmonic, *f*=0 Hz.
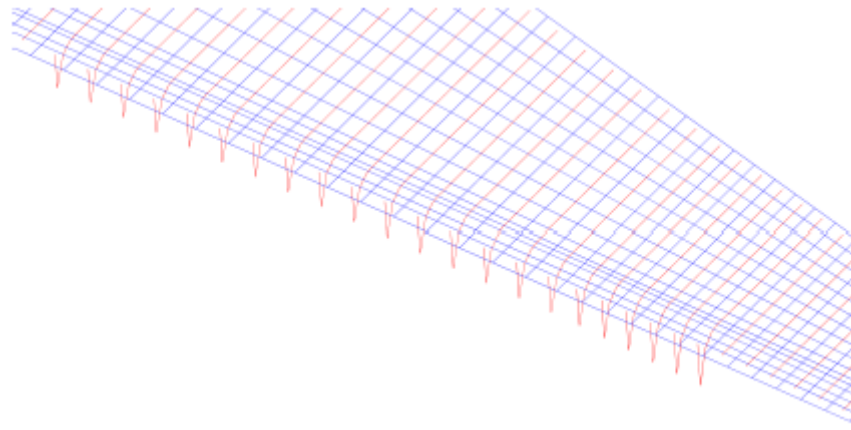
Fig. 92: Zoom on fundamental mode shape.

Moreover a case control was performed for better check the good modeling of the harmonic. A value of K was set to get a frequency about 6 Hz, obtaining the modal shapes in Fig. 93.
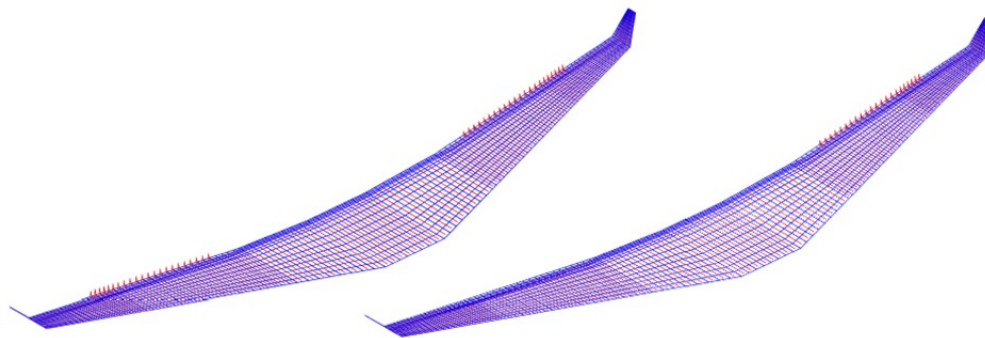
Fig. 93: Outer trailing edge symmetric (LH) and antisymmetric (RH) harmonic, *f*=5.9 Hz.

After these few trial runs, the kinematic mode harmonic was restored to approximately 30 Hz and the following flutter cases were analyzed:

- Baseline: fully operative system
- Actuator group failure at a station;
- • Links failure at a station;
- • Actuator group and links failure at a station;
- • Catastrophic case: actuator group and links failure of three consecutive stations.

The behavior prediction in failure cases was performed in according to FHA (Fault and Hazard Analysis) specifications required by Airbus France.

3.4.2 Baseline: fully operative system

In Fig. 94 the trends of modes frequencies and damping versus flight speed have been plotted with reference to fully operative system. The stiffness is such that dynamic instability does not appear.
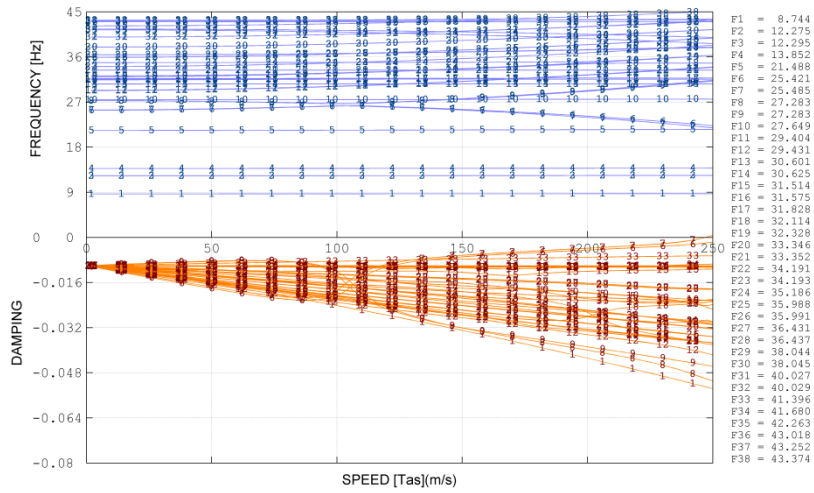
Fig. 94: Baseline V-g plot

3.4.3 Failure cases

Following figures collect the trends of modes frequencies and damping versus speed evaluated for several cases of failure. Failures were assumed to occur on the left ATED, starting from the root station (majorly loaded station).
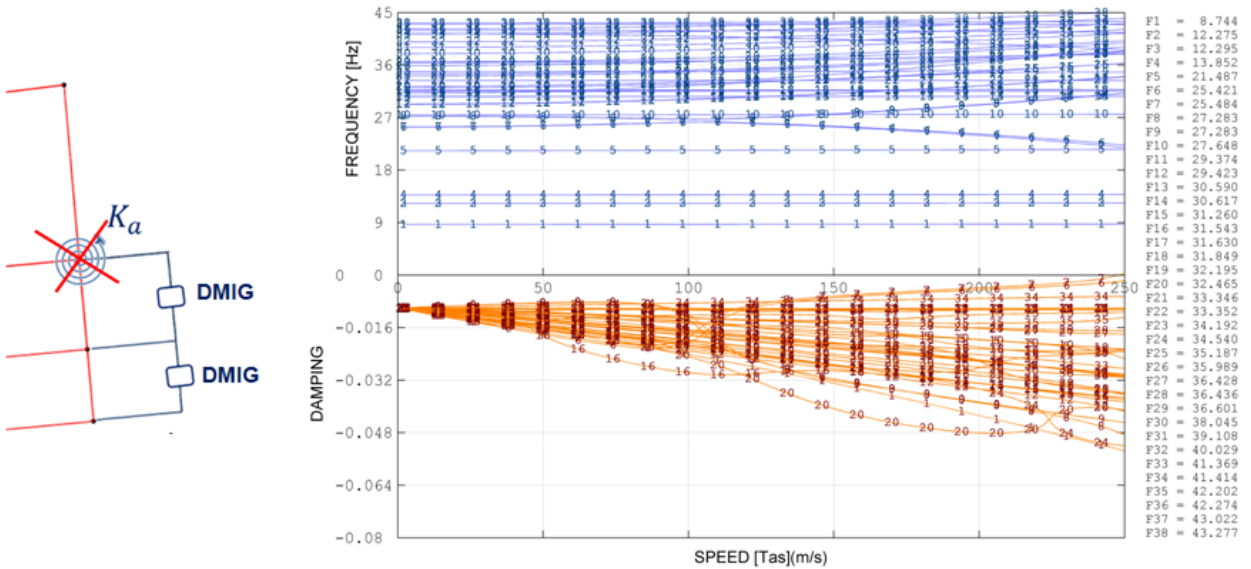
Fig. 95: Actuator failure LH side root station, V-g plot
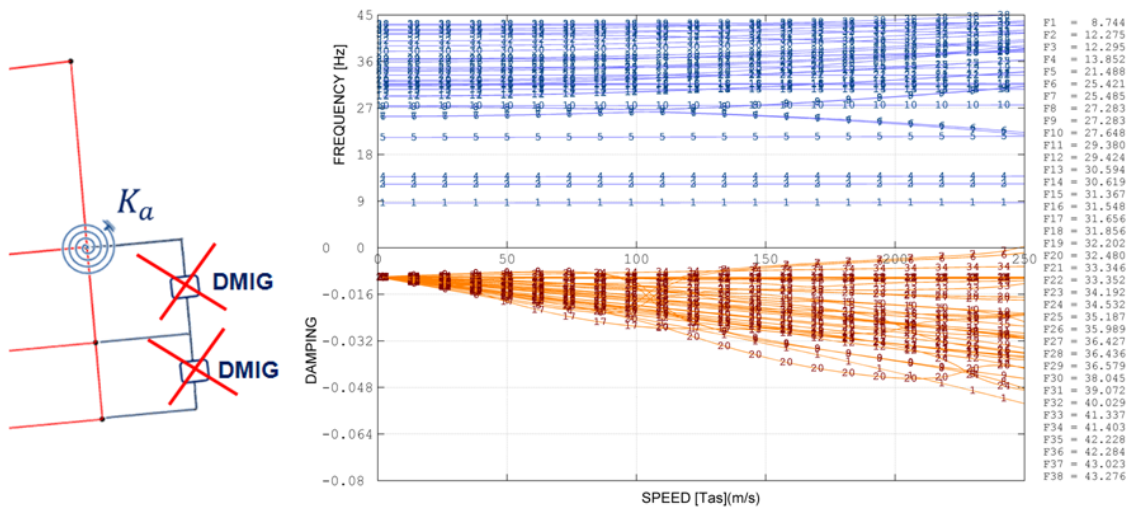
Fig. 96: Links failure LH side root station, V-g plot
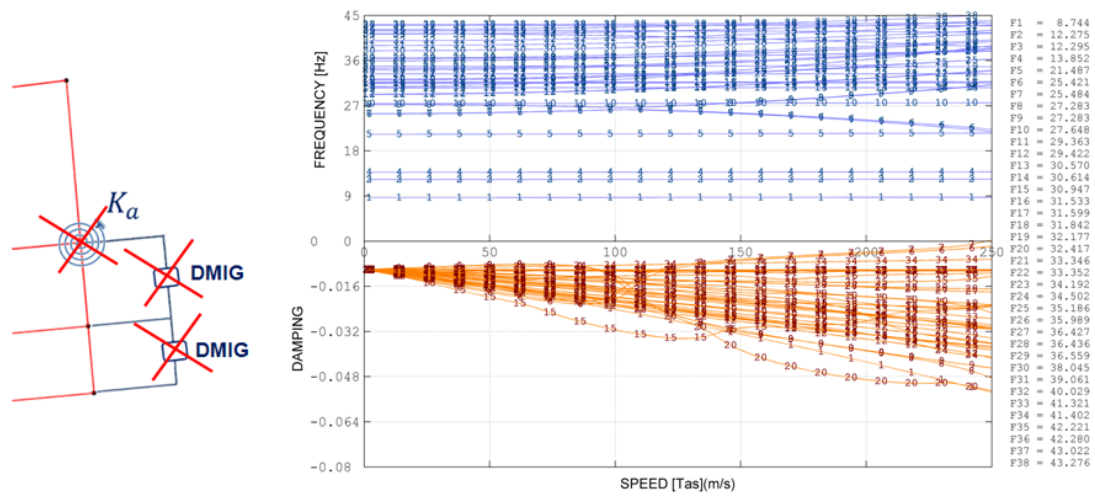
Fig. 97: Actuator group and links failure LH side root station, V-g plot

The system provides a good robustness margin actually; despite the combined failure, it is still stable. In order to meet an aeroelastic instability it resulted necessary to introduce failures of actuator groups and links for the first three ribs, counting from the root station.
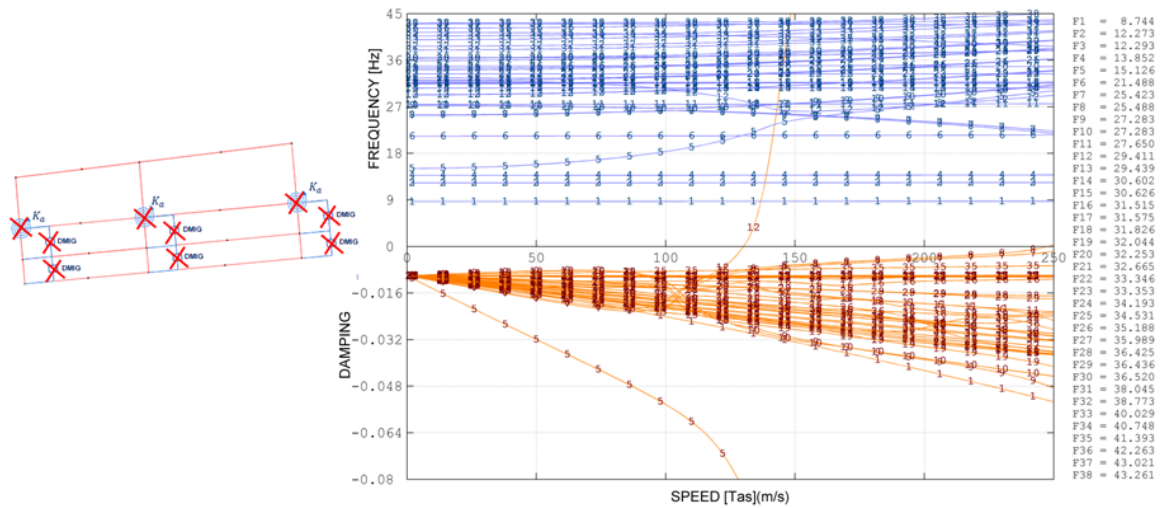
Fig. 98: Actuator group and links failure LH side first three stations, V-g plot

In this investigation case, flutter is present at a speed of about 130 m/s.

Accurate analysis of modal cross participation factors into flutter mode were performed in order to isolate the principal modes involved in detected flutter.

The flutter phenomenon seems to be due mainly to the coupling of two modes (binary flutter), 12 and 14, that induced the ATED bending-torsion (Fig. 99 - Fig. 100). The flutter dynamics resulted indeed more complex: three elastic modes of support are mainly involved: 1, 6 and partially mode 5 (Fig. 101).
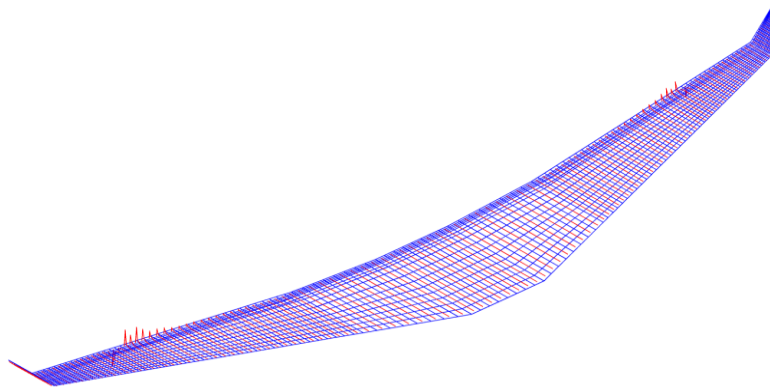
Fig. 99: Mode 12, f=29.4 Hz
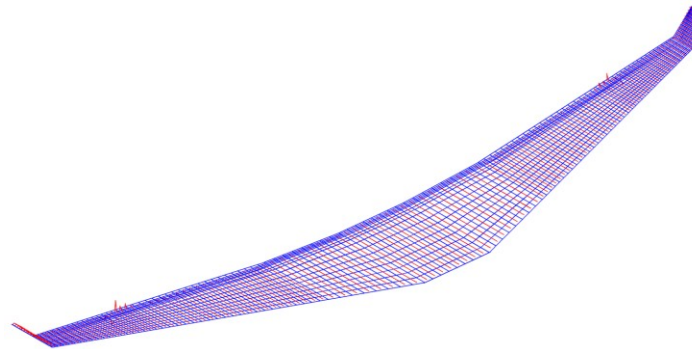
Fig. 100: Mode 14, f=30.6 Hz

76
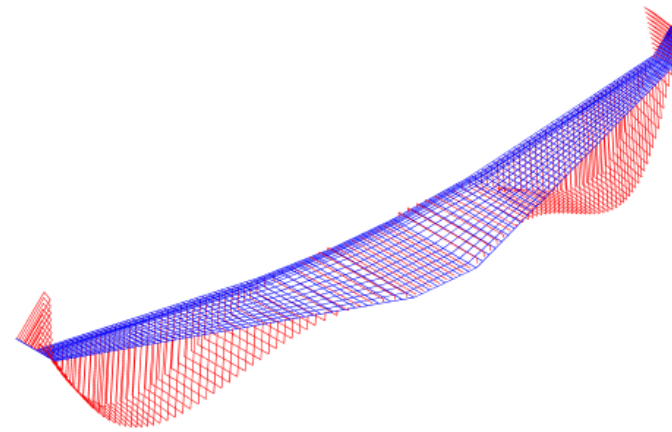
(a) Mode 1, $f = 8.7438$ Hz
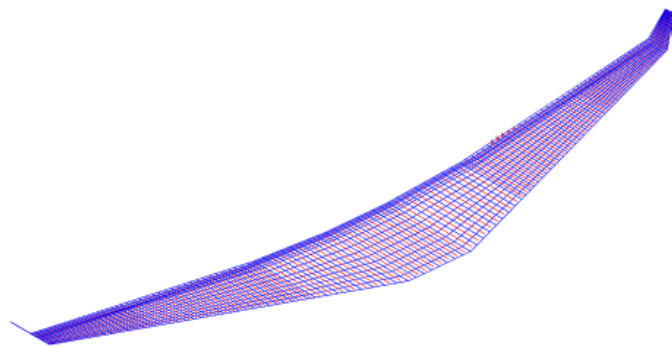
(b) Mode 5, $f = 15.1258$ Hz
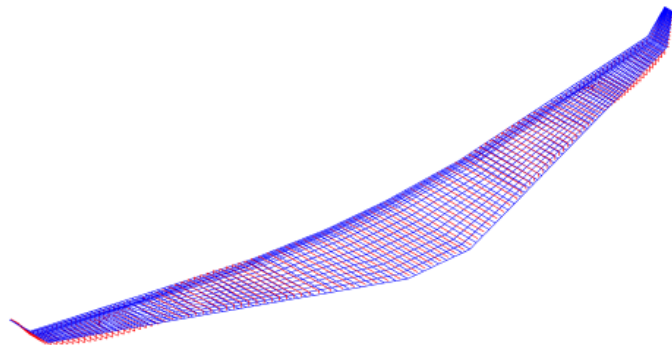
(c) Mode 6, $f = 21.4877$ Hz

Fig. 101: Support elastic modes in flutter dynamic

Obtained results showed that the ATED is not responsible for any flutter instability; moreover compliance with the airworthiness requirements for aeroelastic stability provided by CS-25 was demonstrated. A catastrophic event verifies only in case of three consecutive stations failure, event which is extremely remote according to the fault and hazard analysis outcomes [28].

CHAPTER 4:

Reverse engineering – ATE shapes reconstruction

Reverse Engineering indicates a set of tools and techniques whose main purpose is the shape acquisition of a target object in order to satisfy a large variety of requirements, from Quality inspections to Rapid Manufacturing, from target vs CAD comparison to 3D scanning with non invasive techniques.

In this chapter the shape reconstruction of the Adaptive Trailing Edges demonstrators will be addressed, with the special intention of comparing the attained shapes to the expected aiming at verifying the quality of the manufacturing and the capability of such an innovative technology to hold the target shapes under external loads application.

4.1 PHOTOGRAMMETRY BASIS

R.E. can be defined as the designing of a product through a digital model, obtained starting from a points cloud, extracted by means of three-dimensional scan of a physical object. Typical acquisition techniques are mainly divided into:

- Contact techniques, which are based on tools that scan, by contact, the forms of the object to detect. The disadvantages of this type of techniques are associated to the acquisition time, often very long for large and complex shapes, and for its being somehow invasive, especially for fragile items to be scanned.

- Laser systems, which are very accurate, are not invasive and more and more popular, but still have quite high costs.

- Digital photogrammetry, which is a consolidated measurement technique that allows the acquisition of the metric data of an object (shape and position) without contact, through the acquisition and analysis of a pair of stereometric frames. It has lower accuracy than laser systems but is much more affordable. A special case, called stereophotogrammetry, involves estimating the three-dimensional coordinates of points on an object employing measurements made in two or more photographic images taken from different positions. Common points are identified on each image. A line of sight (or ray) can be constructed from the camera location to the point on the object. It is the intersection of these rays (triangulation) that determines the three-dimensional location of the point.

This last technique, originally invented to be used in architectural survey, is currently used in the field of Reverse Engineering, to study the deformation of mechanical parts subjected to load tests, and precision geometric survey in mechanical and aeronautical applications.

One of the biggest obstacles to its diffusion was definitely the high cost of the necessary equipment, but nowadays the development of computers able to handle a large amount of data and computer graphics have enabled a more simple and quick use, with lower costs. The recent and gradual transition from analogycal photogrammetry to the digital one (defined in slang also "SOFT-PHOTOGRAMMETRY", because of its growing dependence on the total development of dedicated programs) is allowing the advocated transfer of technology, but until now never fully realized between the world of discovery and industry. The introduction of the techniques of image processing by computer has thus radically transformed the approach to the photogrammetric survey, in which technological development was replaced by the continuous development of software that can handle the whole photogrammetric process, limiting overhead investment and allowing a common operator, with good computer skills and photography know-how and even small practical experience, to achieve excellent results. In recent years, the use of programs has allowed the user friendly photogrammetry to present itself in a most

convincing manner than in the past, even outside of research laboratories, greatly expanding the number of potential users.

4.1.1   Digital images: acquisition and characteristics

A digital image is basically a matrix of elements, the PIXELs (picture element), the content of which is expressed by the radiometric continuous function digitized In a discrete function g(i, j), where i, j are basically rows and columns in which the space is sampled; the radiometric content indicates, for example, black or white value, a gray level value or an RGB (Red Green Blue). The process that converts a continuous representation in a discrete one is called <u>digitizing</u>, and is done by sampling the spatial variables and quantizing radiometric corresponding values.

This process can take place in a direct manner, through the use of a digital camera, or in an indirect manner, i.e. by digitizing an image from a scanner slide or negative. In both cases, the heart of the scan tool is a SOLID-STATE SENSOR of variable size, able to collect and accumulate the informations carried by electromagnetic energy, and to make them accessible to the user.

The principle of formation of a digital image is illustrated in Fig. 102: the sensor measures the amount of incident light, which is converted in the form of electric voltage with intensity proportional; the latter in turn is converted by an analog / digital (A / D) in digital number, that is, in bits of information.

LIGHT ENERGY ⇨ | SENSOR | ⇨ ELECTRICAL SIGNAL ⇨ | A/D | ⇨ DIGITAL NUMBER

Fig. 102: Principles of digital image creation.

A digital image consists, then, in a matrix g (i, j) of pixels of the type:

$$G(x,y)= \begin{bmatrix} G(1,1) & \cdots & G(1,C) \\ \vdots & \ddots & \vdots \\ G(R,1) & \cdots & G(R,C) \end{bmatrix}$$

where :

- i=1,...,C, is the row index;
- j=1,...,R, is the column index;
- R=maximum number of lines;
- C=maximum number of columns;
- G (x, y) = {0,1, ..., max} are radiometric values.

80

4.1.2 Radiometric Resolution

The process of forming a digital image therefore consists in two operations, the quantization and sampling, which are directly related to the two fundamental characteristics of this type of images: the RADIOMETRIC RESOLUTION and GEOMETRIC RESOLUTION.

The first is related to the quantization, i.e., the conversion of the intensity of the light signal (transformed by the sensor to a real value of electric intensity) into a whole number, which is stored for each pixel. If the intensity is converted in only two samples, 0 and 1, than one can represent only two levels of radiance, white (1) and black (0), and this information can be stored in a single bit. If the intensity is converted into 256 numbers, 256 levels of radiance can be represented, from 0 (black) to 255 (white), and one can have an image in shades of gray or monochrome (color palette). In this case, the image is said to be 8 bits or 1 byte, as an integer between 0 and 255 can be stored in one byte. Color images with three channels, are represented by the following relationship:

$$G_c = \{ g_1(i,j), \; g_2(i,j), \; g_3(i,j) \} \, ,$$

In which the three functions $g_1(i, j)$, $g_2(i, j)$, $g_3(i, j)$ may indicate, for example, the three levels of Red, Green, Blue (RGB images, or true color). For these images, it can been defined an image matrix in three planes, as, for example, in RGB, each color is the superposition of the three fundamental colors, in which the intensity of each one is represented by a value between 0 and 255; radiometry of a pixel is represented by three numbers which express the intensity of the three fundamental colors, three bytes for each pixel.

It is possible to analyze various types of digital images in relation to their radiometric content.

N.° bit	N.° byte	DN	Digital Image Type
1	1/8	2	Black and White
8	1	256	Grayscale or color palette
16	2	65536	64K colours
24	3	16777216	Red Green Blue (RGB)

4.1.3 Geometric resolution

The geometric resolution is related to the sampling, that is basically the area of image corresponding to each element of the sensor; as a digital image consists of a two-dimensional matrix whose elements or pixels are the containers of the information, a high geometric resolution involves the generation of a matrix with a large number of rows and columns, namely a large number of very small pixels. The geometric size of

the pixels to the soil affects the reproduction of the details of the scene and is determined by the distance of shooting and its focal length. The parameter that indicates the number of pixels in a unit of length, and then the size of the same, is the geometric resolution, which is usually indicated in DPI, i.e. Dots Per Inch.

$$DPI= \frac{number\ of\ pixel}{inches}$$

Directly related to the size of the pixel is the definition of the system of internal reference image. In fact, wanting to use a digital image for photogrammetric purposes, the relationship between the position of the pixel and the coordinate system image has been defined. Fig. 103 shows the image coordinate system with the origin shifted by half a pixel outside of the image matrix; the image coordinates of the center of a pixel gij are obtained by multiplying the index number for the size of the pixels.
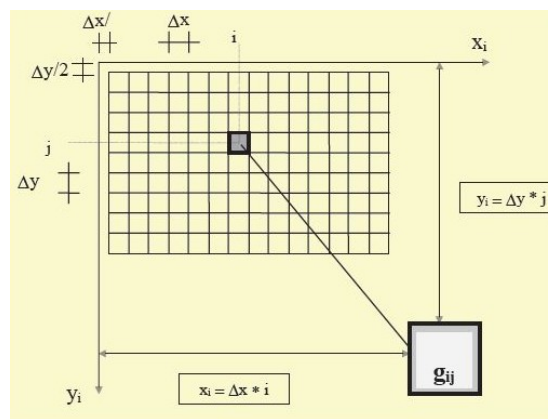
Fig. 103: Metric content of digital images

The traditional measure of coordinates is replaced by the identification of the pixels within the "image matrix". This position results in real "coordinates object", through analytical photogrammetric relations. If pixels are conveniently small, row and column indices can be assumed as *image coordinates*, and also the principal distance, C, can be expressed in units Δx and Δy.

The *image coordinates* define the locations of the object points' images on the sensor. The *exterior orientation* of a camera defines its location in space and its view direction. The *inner orientation* defines the geometric parameters of the imaging process. This is primarily the focal length of the lens, but can also include the description of lens distortions. Further additional observations play an important role: With scale bars, basically a known distance of two points in space, or known fix points, the connection to the basic measuring units is created.

4.2 GEOMETRIC PARAMETERS PRELIMINARY ASSESSMENT

4.2.1 *Distance from the target, focal length, field angle*

The camera used during the photogrammetric analysis had an APS-C sensor (22.5x15mm) with 20 Mpx resolution installed. This means that, according to the common aspect ratio of two/thirds, the sensor has an array of 5472x3648 pixels.

This type of sensor has lower dimensions than a typical full frame sensor, hence the focal length needs to be multiplied by 1.6 to get the actual one. Moreover, focal lengths larger than 35mm were chosen to avoid excessive lens distortion induced on the target; aiming at a resolution of approximately ≈0.1 mm for shape reconstruction, it was preferred to make each pixel corresponding to a shooted area not larger than 0.05*0.05mm2

These considerations led to chose the couple focal length-shooting distance invoking the diagram in Fig. 104. It represents the focal length vs the field angle, trivially related to the shooting distance taking into account the maximum area that can be shot with the expected resolution.

Variazione dell'angolo di campo al variare della lunghezza focale

- 2° - 1200 mm
- 4° - 600 mm
- 5° -500 mm
- 6° -400 mm
- 8° - 300 mm
- 12° - 200 mm
- 18° - 135 mm
- 23° - 105 mm
- 34° - 70 mm
- 46° - 50 mm
- 64° - 35 mm
- 76° - 28 mm
- 84° - 24 mm
- 104° - 17 mm
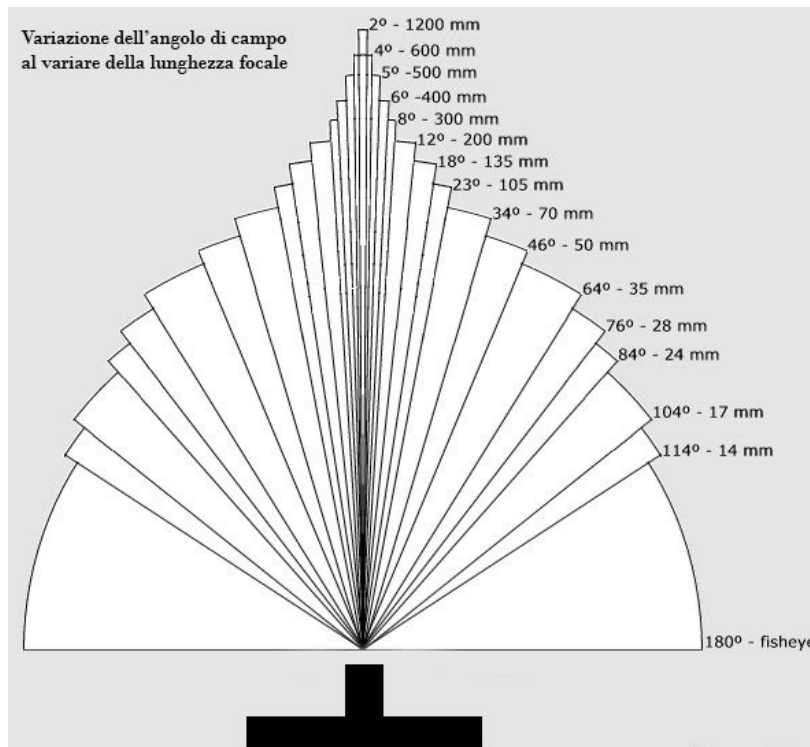- 114° - 14 mm
- 180° - fisheye

Fig. 104: Focal length vs field angle

About the orientation of the camera with respect to the target, it is possible to choose between two alternatives:

- Convergent axes: this provision tries to reproduce the same conditions in which the eyes observe the reality. In fact, when the position of an object is observed at a distance greater than 25 cm and less than 1 m, the visual rays describe bundles of straight lines whose axes are convergent. The similarity of the camera to the human eye, however, is only theoretical; this does not present the automatism of which, instead, enjoys the eye. For example, looking at an object, the eye selects only what matters. The photographic camera, as opposed, distinctly captures also what is behind the object so, with the convergent axes shooting, the background may be different on the two frames and disturb the stereo vision.

- Axes perpendicular to the base: this approach is called "normal case". The advantages that it presents are:

  1) Simplicity of mathematical formulas with which it is possible to derive the spatial coordinates of the points;

  2) Arrangement of frames being returned.

  Compared to the technique of convergent axes, it has the drawback of not using the whole surface of the frames: this problem can be partially reduced by resorting to the side shift, and wide overlapping frames.
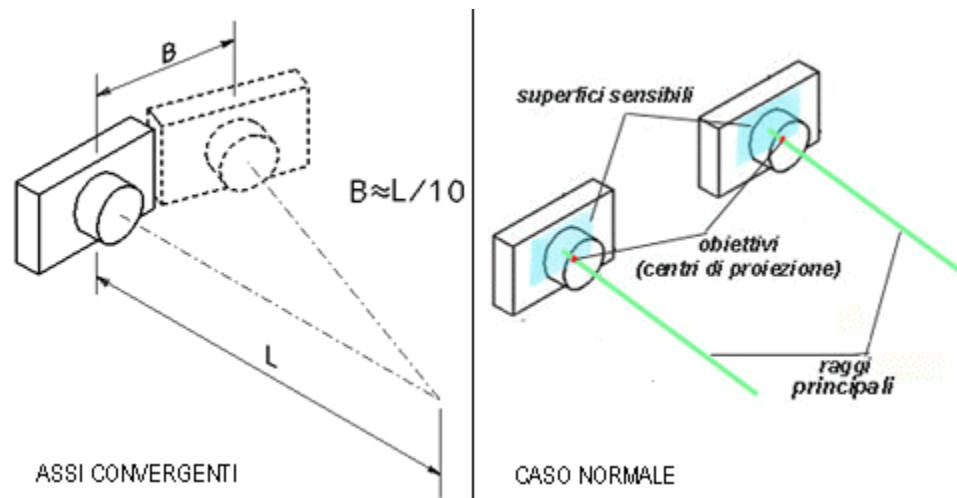
Fig. 105: Camera orientation toward the target

Both methods have been employed, as described in the following paragraphs.

4.2.2 Markers

Both commercial and open source software provide the user with coded targets that can be printed and stuck onto the object to be scanned. Each target is discerned by the software and eases the creation of well known positioned points in the 3D reconstruction. Having such well distinguishable

points enable the user to properly introduce a scale bar for the points cloud starting from the measured positions of the coded target above the object.

4.2.3   Surface texturing

When shooting targets with a gloss finish, non-textured, it is difficult keeping unchanged the lighting condition in each shot. In fact, when shooting, the orientation of the camera with respect to the object must change simply due to the different curvatures of the target surface, and light reflections involve always different intensity of the incident light rays on the camera sensor. As a consequence, points are hardly matched among several shots and very low accuracy is met. A further drawback of glossy surfaces is the low contrast that can be achieved; the higher the contrast is set, the lower the capability to catch details in darkest or lightest areas. In order to introduce more definition during the shooting phase, a structured light was projected onto the target.

The projection of structured light consists into projecting a known pattern of pixels of a scene: the way in which these figures are deformed, encountering the surface, allows vision systems to calculate the depth information (depth) and the surface of the objects present in the scene itself . In principle, it is possible to generate various types of patterns, but the most common method, fast and versatile, involves the projection of a number of stripes of light simultaneously. These last can be generated mainly following two different methods: *interference of laser sources* or *projective method*.
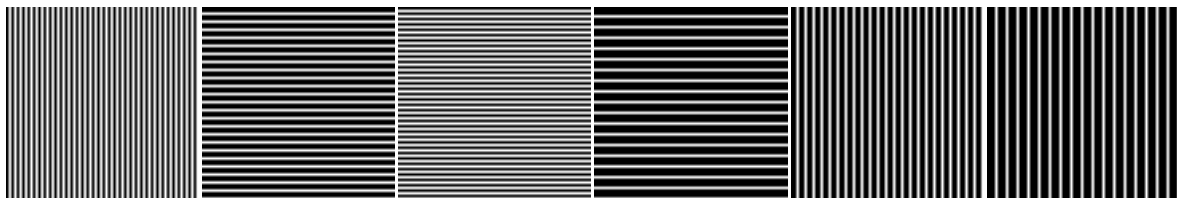
Fig. 106: Examples of patterns

- As regards the *laser solution*, two planar light sources are made to interfere: the result is the creation of regular and equidistant lineas. The size of the fringes can be obtained by changing the angle between the two beams. This method allows you to generate a very precise pattern with a great depth but with high implementation costs, strong reflection problems and defects typical of laser sources (speckle).

- The *projective method*, instead, exploits non-coherent light sources, called *projectors*. In this case, the precision of the instrument is a critical parameter: if on one side there are small discontinuities due to the edges of the pixels themselves that make up the image, on the other side they can be attenuated by the focus lens. A more versatile and fast method consists in the

projection of light patterns, which are composed by several lines (bright fringes): this allows the acquisition of many samples simultaneously. The schemes most used consist, as already mentioned, in parallel lines.
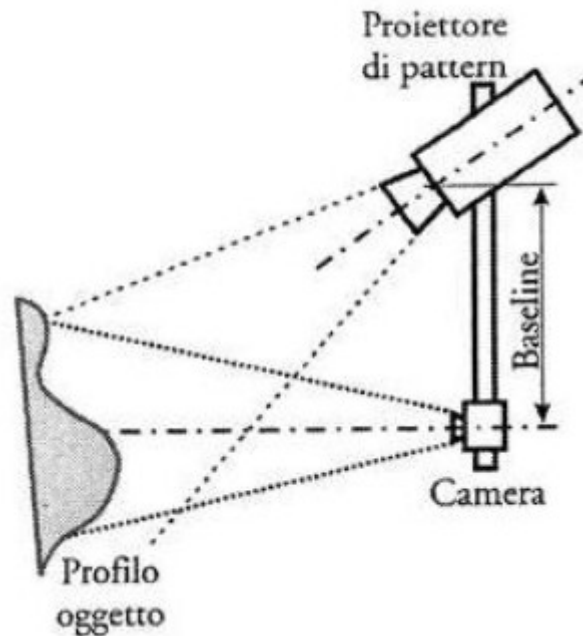

Fig. 107: pattern projection setup scheme

4.2.4   Surface Opacification

Optic approach in photogrammetry presents similar issues to photography in shooting transparent and shiny surfaces; a loss of details is quite common and in our case it might have detrimental impact on the shape reconstruction. For Saristu demonstrator, an opaquing spray was used to prevent the light to go through the transparent top layer and be reflected by the aluminum surface below it.

4.2.5   Preliminary Tuning results

The methodology described so far was tuned to identify the best setup solutions for accuracy maximization.

A set of scan was performed on the 2-bay demonstrator, each time comparing the reconstructed 3D shape with the CAD file and analyzing the deviations and the RMS of the error. In such a way, the best setup could be chosen for the tests in operative conditions.

ATED lower skin 3D reconstruction with markers and no texture

Six markers were applied on the surface; they were numbered and properly spaced. The contour of the deviations between the obtained scanned surface and the CAD file was reported in Fig. 108. The deviation varies between about +2 mm (red part) and - 2mm (blue part). It is trivial to observe that a perfect

reconstruction would have provided an entirely - green contoured map. What emerges is that the reconstructed model does not coincide perfectly with the CAD one. .. The portion of skin made up of foam is not coplanar with that of Aluminum. This leads to the fact that points in that area have not been acquired by the software, which does not provide with a very accurate analysis. This is mainly due to the fact that the silicone foam is uniformly white with glossy surface because of the transparent top layer; thus, details are very difficult to be caught in photography.
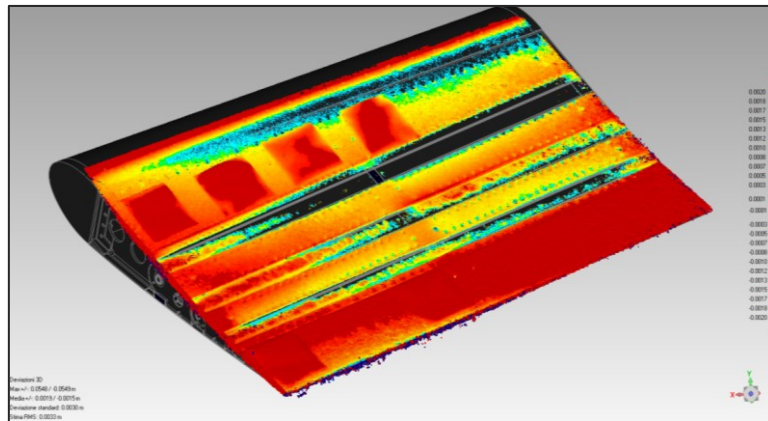
Fig. 108: ATE lower skin 3D shape reconstruction: error deviation.

ATED upper skin 3D shape reconstruction with markers and surface texture

In order to improve the degree of precision of the analysis, a black and white striped pattern was projected on the ATED upper skin, as described in §4.2.3. A rail, as sliding support for the camera, was suitably built. It was kept at a distance of about 170 cm from the demonstrator to simulate the same conditions of shooting during the wind tunnel test campaign. The procedure already set out was repeated, leading this time to a much better estimation of the shape (Fig. 110).

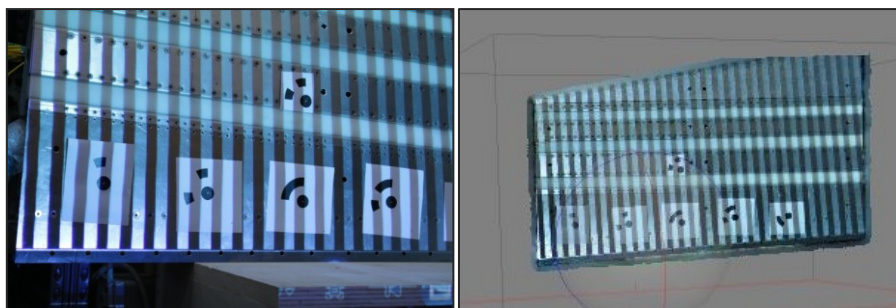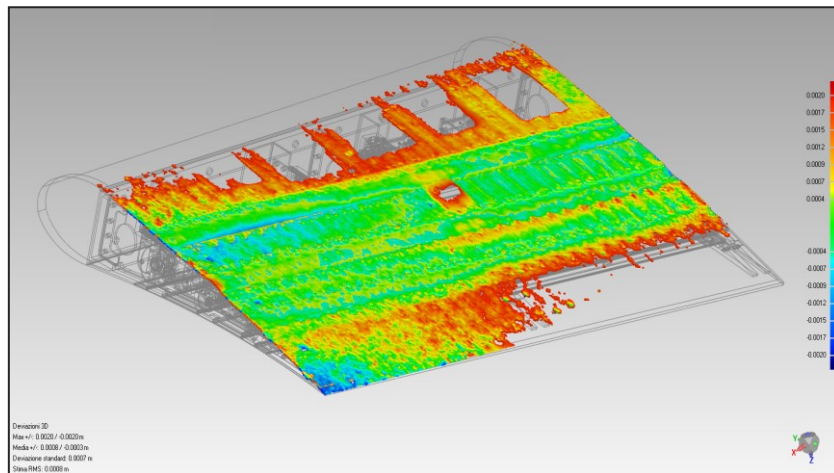**Fig. 109: patterned ATE surface - picture and reconstructed shape**

Fig. 110: ATE skin 3D shape reconstruction: error deviation

A large part of the reconstruction coincides with the CAD model (green area in Fig. 110); the red-colored area, on the contrary, shows a deviation of 0.0020 m. An evident step is present in the color map (green-orange transition), which has the same height of the silicone top layer; this was expectable since the top layer is transparent to the white light and cannot be caught by an optic device. Nevertheless, the RMS of the deviations is about 0.0008 m, already suitable for our convenience.

ATED upper skin 3D reconstruction with markers, surface texture and surface opaquing

Last strategy adopted to increase the reverse engineering accuracy was the use of an opaquing spray on the shiny transparent surface of the top layer. Such strategy had the purpose to simulate the shooting of a solid painted skin instead of a transparent one.
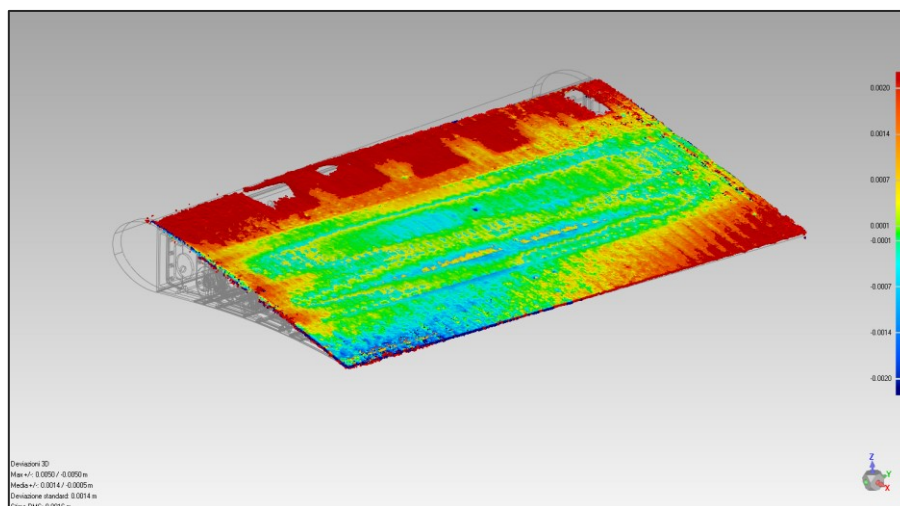
Fig. 111: ATE Upper skin 3D shape reconstruction versus CAD model: deviations analysis.

Deviations analysis shows a better reconstruction of the boundary aluminum-top layer, even though not anywhere perfect. This is mainly due to the hand - made application of the opaquing film, which is not well uniformly distributed. Such strategy further improved the RMS down to 0.0006 m.

As a further result of such a preliminary tuning tests, a misalignment of the edge could be identified; the 2-bay demonstrator seemed to have the tip rib slightly morphed with respect to the root one even in baseline configuration, probably due to a preload applied on the elastic skin during the assembly. Such a deviation from the target shape could be eventually recovered by differentially rotate the servo-actuators.

4.3 EXPERIMENTAL SHAPE RECONSTRUCTION OF THE ATE IN SIMULATED OPERATIVE CONDITIONS

The Wind tunnel test activity aimed at verifying whether the demonstrator foam strips showed curving bubbles above 1 mm thickness caused by the pressure loads arisen during the simulated operative conditions. A photogrammetric optic approach was taken into account, since the presence of the transparent silicone layer does not permit the use of any bonded sensor; moreover such approach gives accurate results overall the model in a "continuous" way (the discrete set of point are the pixels, which are sufficiently small and close each other to provide an accurate interpolation of data), instead of a discrete matrix of acquisition points provided by the classical sensors. For this reason, it was decided to perform the ATE skin shape reconstruction through a photogrammetric approach by using Agisoft PhotoScan Software[3]. The methodologies adopted and the results obtained have been outlined in the following paragraphs.

The activity can be divided into two phases:

- Phase 1) an optic photogrammetric approach was set up and tuned for the Adaptive Trailing Edge shape reconstruction; skin shape was reconstructed at Wind Tunnel off (dry conditions).
- Phase 2) ATED skin shape reconstructed in simulated operative conditions (wet conditions).

<u>Fairing design</u>

In order to verify the effectiveness of the morphing skin in simulated operative conditions, comparable aerodynamic loads to those occurring during the tests campaign in TSAGI Wind Tunnel in Russia, need be obtained. This requirement drove the design of the ATED fairing for the tests to be performed at the University of Naples. SARISTU ATE five bays demonstrator covers the 10% of MAC of the model to be tested in TSAGI at a flow speed of about 90 m/s. On the other hand, the two-bay demonstrator to be tested into the University of Naples "Federico II" Wind Tunnel will face a maximum achievable flow speed of about 50 m/s -considerably lower than the TSAGI W/T one, with a consequent lower dynamic pressure. Aiming at reproducing load levels comparable to the Russian ones, it was necessary to compensate the lower velocity by reaching higher values of the C_p. Therefore, a fairing profile was suitably studied in order to let the ATE extend up to the 50% with respect to the MAC. The modified NACA 4412 was chosen as best compromise between two requirements: on one hand, it well link with the ATE airfoil, considered as a plain flap profile; on the other hand, by providing C_p values 2.3 times

---

[3] Agisoft PhotoScan is an advanced image-based 3D modeling solution aimed at creating professional quality 3D content from still images. Based on the latest multi-view 3D reconstruction technology, it operates with arbitrary images and is efficient in both controlled and uncontrolled conditions. Photos can be taken from any position, providing that the object to be reconstructed is visible on at least two photos. Both image alignment and 3D model reconstruction are fully automated.

greater than the ones expected in TSAGI W/T (Fig. 112). Aerodynamic loads were calculated under the following hypothesis:

- 2D profile;
- In baseline, morphed up and morphed down conditions;
- Hinge position at the 50% of the Mac;
- Morphing angle (β) of $\pm 5^\circ$;
- Adimensionalized respect to the chord length.

Overall, aerodynamic loads at Unina W/T were nearly equal to the 60% of the maximum ones expected in Russia, which will allow to state whether the foam stripes tend to bubble or are sufficiently stiff in out of plane direction.
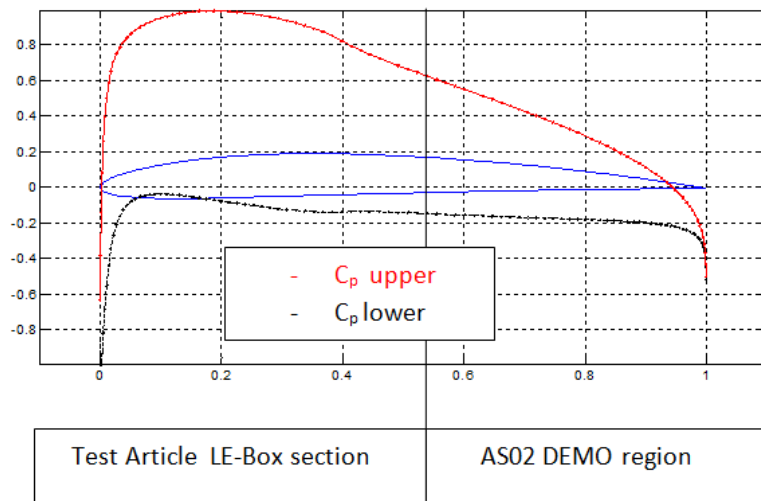

Fig. 112: Pressure Coefficient on NACA 4412 at zero AoA.

Expected loads due to the pressure distributions were properly used for the test article sizing, by means of FEA. Fig. 113 shows the modal shapes of the test article (fairing plus ATE), and makes evidence of the larger stiffness of the fairing with respect to the ATE, object of analysis.
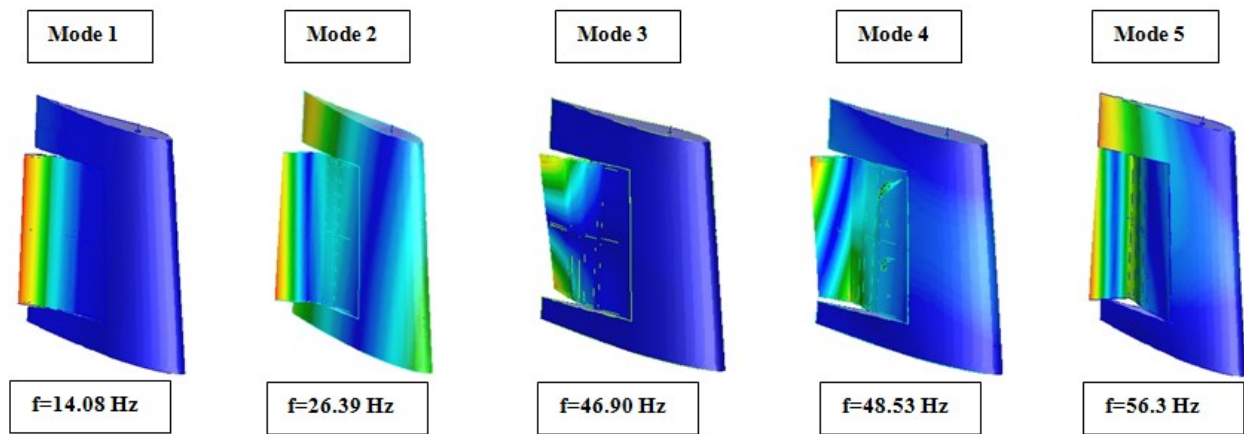
Fig. 113: Modal shapes of W/T test article.

4.3.1 Wind tunnel tests

The experimental setup was properly prepared, as shown in Fig. 114, in order to:

- detect skin bubbles induced by aerodynamic pressure;
- perform functionality checks in wet conditions.

The test article was placed into the wind tunnel. The control panels for the ATE morphing were arranged near the WT control instrumentation, together with the acquisition system. Camera was installed on a trail, supported by a rig properly assembled to have adjustable height, and remote controlled by the laptop. Finally a projector was placed on a tripod and oriented toward the target, for the pattern projection.

The test was performed in unmorphed, morphed down and morphed up configurations, for the upper and lower skin; photogrammetric shape acquisitions were realized at a flow speed of 0 m/s and 30 m/s, in order to overlap wet and dry conditions.

Fig. 114: test setup for Wind Tunnel
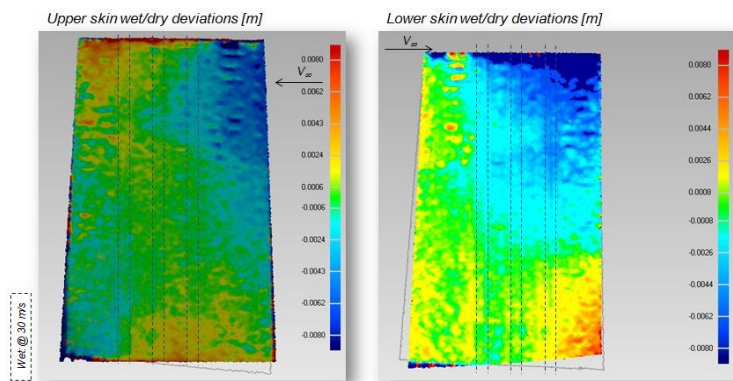
Test results – Baseline conditions

Fig. 115: Upper and lower skin wet/dry deviations in baseline conditions
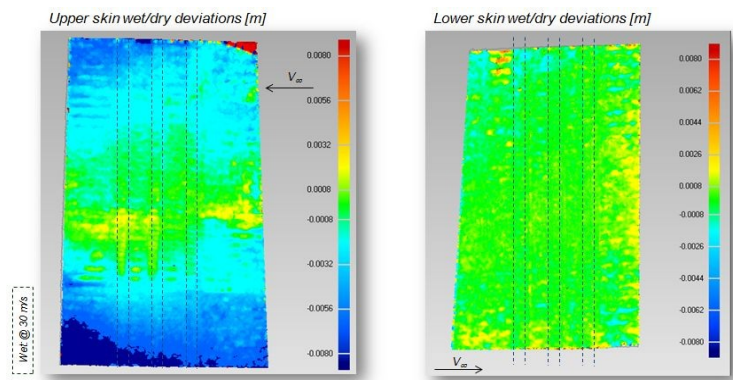
Test results – Morphed up conditions

Fig. 116: Upper and lower skin wet/dry deviations in morphed up conditions
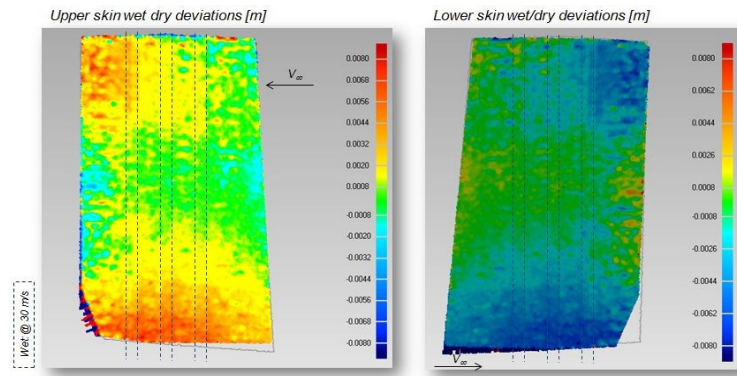
93

Fig. 117: Upper and lower skin wet/dry deviations in morphed down conditions

Results description

Thanks to a non-invasive approach of Reverse Engineering, based on optical devices and rational set up, morphing skin shape was reconstructed under the application of aerodynamic loads pertinent to simulated operative conditions arising at different morphed and unmorphed configurations.
Test outcomes showed that:

- reliable and stable morphing compliant with design requirements is assured by the device both in absence and in presence of applied aerodynamic loads;
- no skin bubbles induced by aerodynamic pressure were detected up to 30 m/s of flow speed;
- no oscillations of the T/A during morphing in the airflow.

Focusing on the lower skin wet/dry deviations in morphed down configuration, it is possible to observe a green central area on the upper skin, which is to be read as the negative of the one on the lower skin.
This simmetry in the deviations suggests how the only difference between wet and dry conditions consisted uniquely in a structural deformation induced by aerodynamic loads.

The conceived (and tested) structural arrangement proved also the ATED to be extremely affordable and ready for the larger W/T test campaign at the Russian aerodynamic research center TsAGI.

4.4 REVERSE ENGINEERING OF THE 5-BAY DEMO

Before the final assembly of the IS12 demonstrator to be tested at TSAGI, the 5-bay ATE was reconstructed to:

- assess the proper manufacture in accordance with the requirements of target shapes to be obtained;
- compare the morphed shapes reconstructed with the target ones to evaluate the actual excursion of the ATE;
- provide the CIRA with preliminary information about ribs deformations to be eventually recovered by means of differential actuations, as detected for the two-bay.

The reconstruction was performed in dry condition, with the same procedure assessed for the two-bay, controlling all the servo-actuators indistinctly. For our intent, only the reconstruction of the upper surface was necessary to provide satisfactory achievement of the goals.Markers were stuck on the upper surface. Being unavailable the CAD of the skin in morphed configurations, the reconstructed shapes were compared to the inner structure. Therefore, a constant offset of the deviations had to be expected due to the distance of the scanned surface from the inner structure equal to the skin thickness. Figures from Fig. 118 to Fig. 121 show the reconstructed scanned surfaces and the deviations contours, where the distance of the inner structure from the scanned shapes is reported.

Several observations can be done.

1. Deviations of the morphed shapes were evaluated by comparing the scan with the internal structure morphed of an equivalent rotation of -4/+4 degrees. By using the target angles of -5/+5 degrees larger errors would have been measured. This meant that the ATE didn't match the target angles, and this was due to the limited stroke of the actuations.
2. Morphed down shape has an almost uniformly light blue colored contour, corresponding to the skin thickness of 2.5 mm. The contour darken at the trailing edge toward the tip, thus the morphing down capability seems less effective for the smaller ribs. Opposite consideration is done for the morphed up shape. At the tip the morphing up is more effective, providing larger displacement than at the root, for same actuators rotation. Such a small deviations could be easily recovered with a differential actuation for each rib.
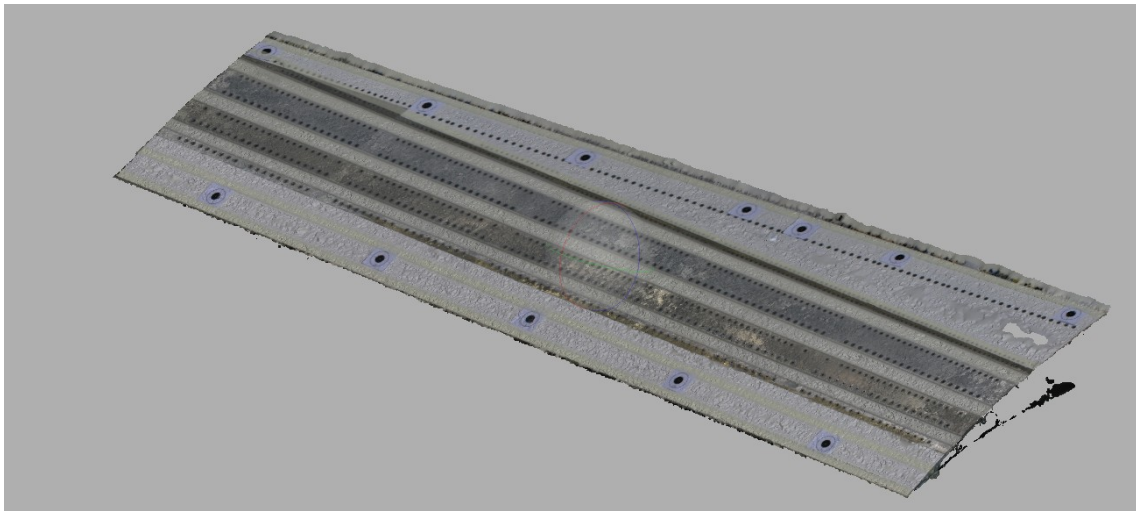
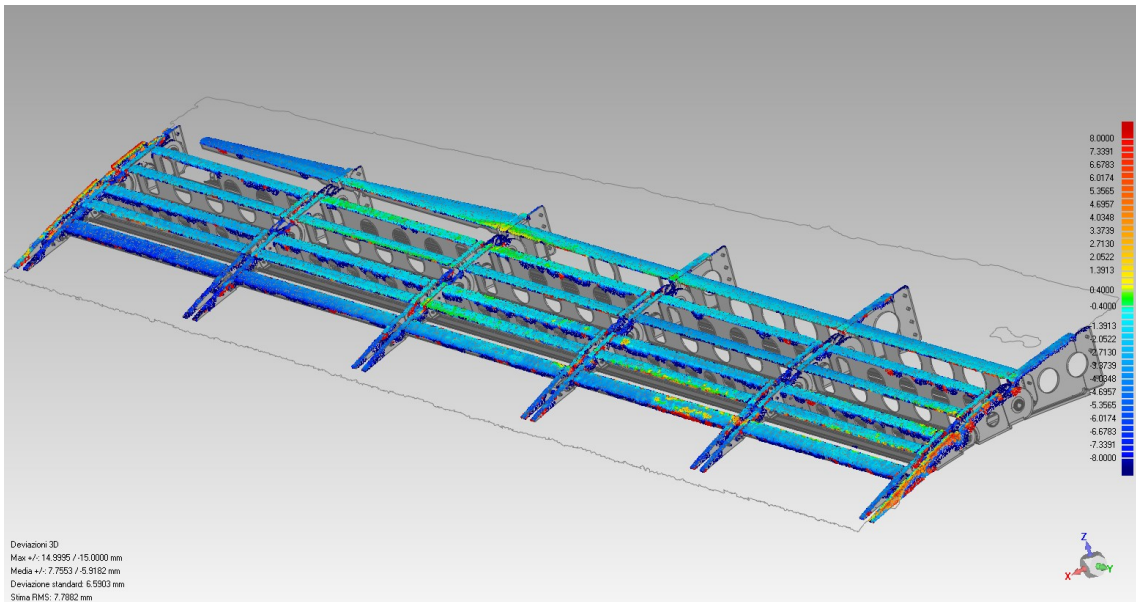**Fig. 118: Scanned morphed down configuration on the ATE**

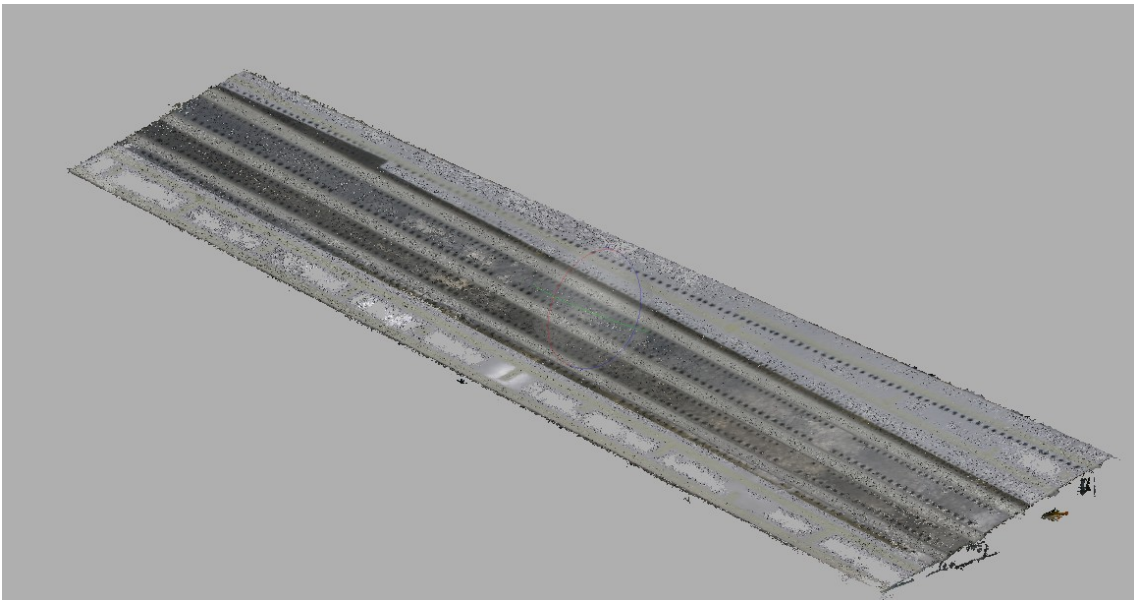**Fig. 119: deviations of scanned morphed down configuration from CAD.**

Fig. 120: Scanned morphed up configuration on the ATE

Deviazioni 3D
Max +/-: 15.0000 / -14.9999 mm
Media +/-: 6.1091 / -6.1367 mm
Deviazione standard: 7.5368 mm
Stima RMS: 7.5720 mm
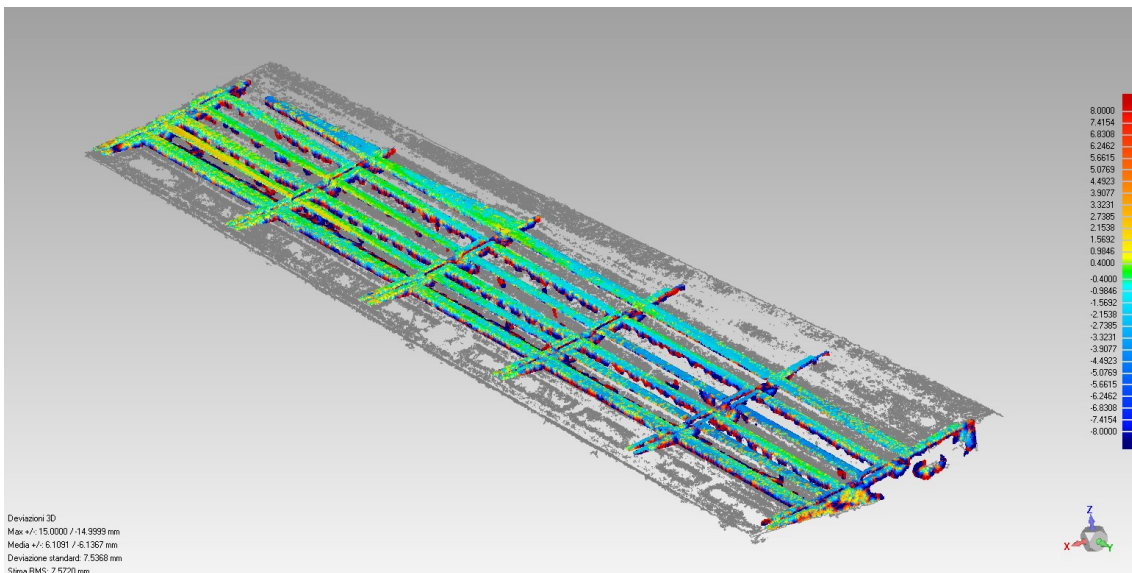
Fig. 121: deviations of scanned morphed up configuration from CAD.

3. All the contours, and with much more evidence the baseline shape deviation contour, showed that the fourth rib (numbered from the root toward the tip) was assembled in a slightly misaligned position, as remarked by the positive deviations in correspondence of the blocks zero and two, corresponding to a "depression" in that area, which was actually detected by contact.

4. Baseline reconstruction also showed that the ATE deviates from the CAD at the tip station, in particular the internal structure results farer than in other areas.
    Such a deviation resulted much more evident during the assembly phase of the IS12 demonstrator, when the ATE took place in between the fairings, as shown in Fig. 124.
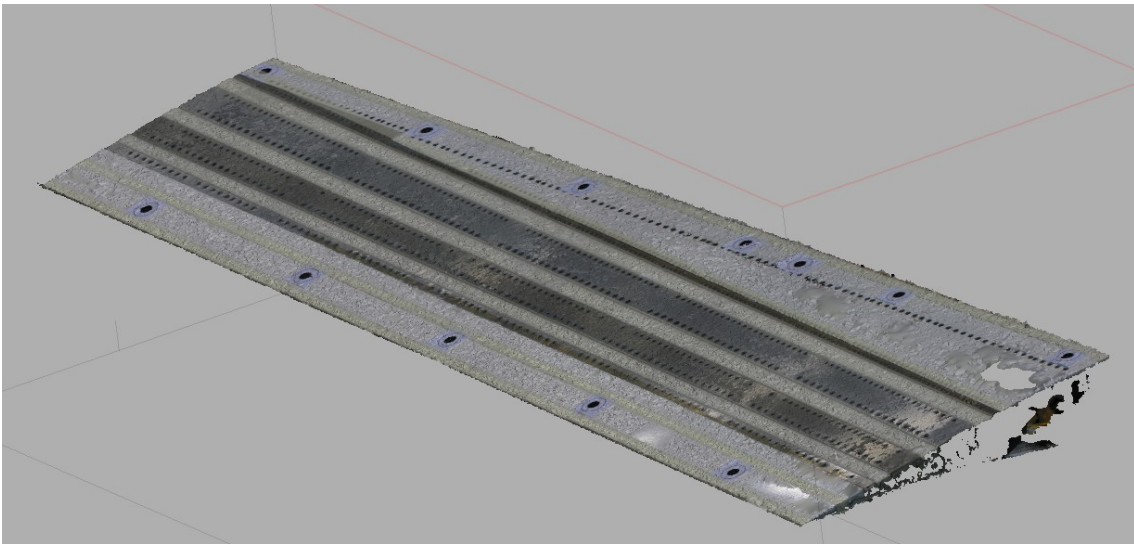
Fig. 122: Scanned baseline configuration on the ATE

Deviazioni 3D
Max +/-: 14.9999 / -15.0000 mm
Media +/-: 8.5217 / -6.7784 mm
Deviazione standard: 8.2356 mm
Stima RMS: 8.6254 mm
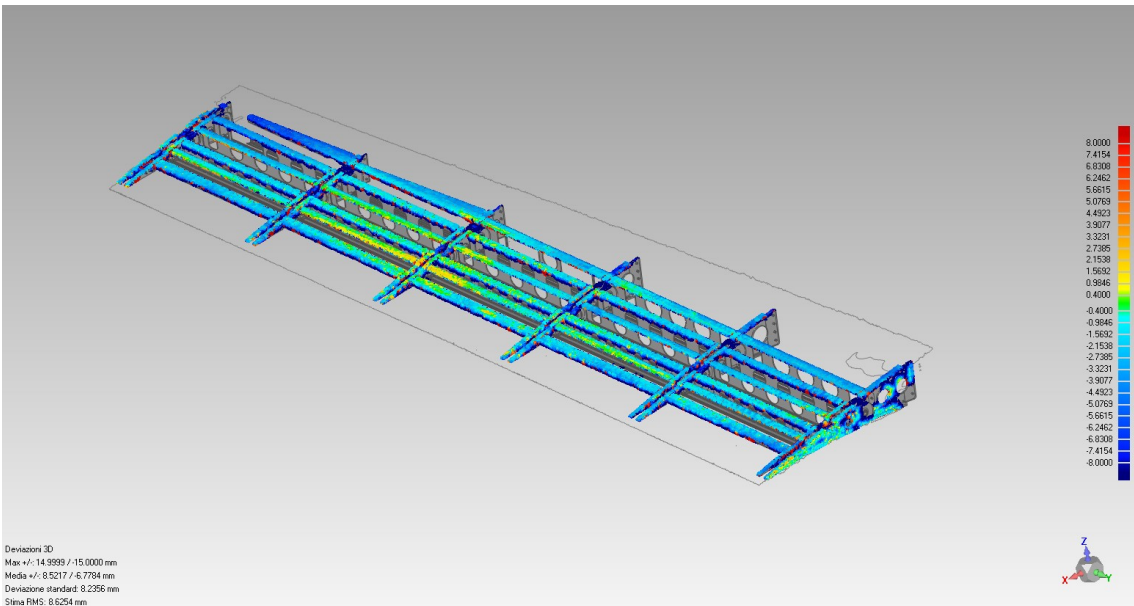
Fig. 123: deviations of scanned baseline configuration from CAD.

Fig. 124: ATE assembled on the IS12 demo.

The application of a low cost photogrammetric approach for the shape reconstruction provided good results in terms of accuracy, repeatability and affordability.

Even if such a technique appeared very user friendly, results are very sensitive to the expertise of the user; therefore, the assessment of the technique is suggested case per case by means of benchmark tests.

Conclusions

In this work, research was conducted to develop an adaptive trailing edge device aiming at maximizing wing aerodynamic performance in cruise condition. Wing shape is controlled during flight in order to compensate the weight reduction following the fuel burning, by allowing the trimmed configuration to remain optimal in terms of efficiency (Lift to Drag ratio) or minimal drag. Trailing edge adaptations were inves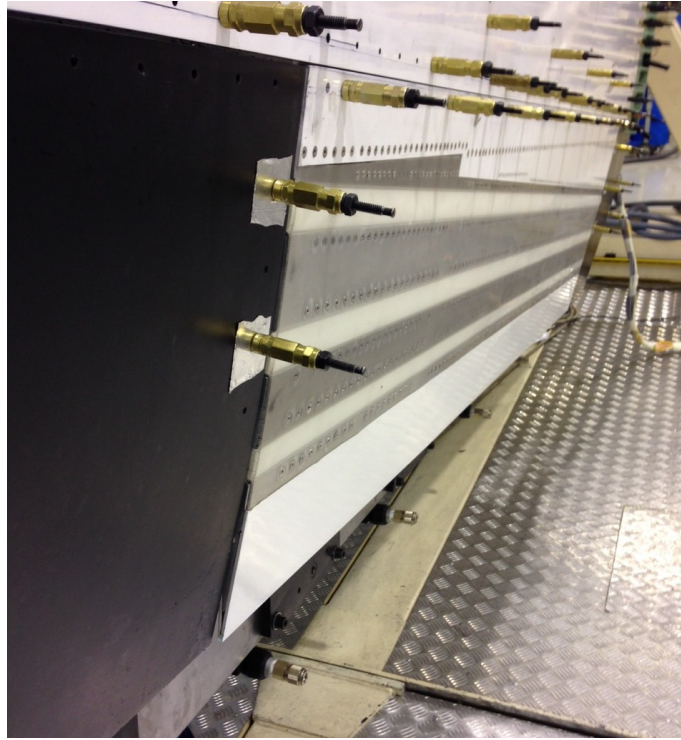tigated to achieve significant benefits in aircraft fuel consumption whose reduction ranges from 3% to 5% depending on flight mission. Target morphed shapes -to be reproduced in flight- were determined through CFD-based optimization analyses; the same applies to the overall dimensions of the morphable trailing edge.

In order to assure the necessary figures for the aerodynamic efficiency of the reference A/C wing, it was found that the morphable trailing edge portion should have spanned 3.0 meters along the inner wing (kink) and 7.3 meters along the outer wing region; the required chordwise extensions should have been equal to the 20% and to the 10% of the wing MAC (nearly 3.5 meters) respectively for the inner and the outer segments. For each cross section of the trailing edge, target morphed shapes were defined by adjusting the airfoil camber such that the airfoil tip was forced to rotate, by an angle β, around a virtual hinge located on airfoil camber line at the most forward chordwise location. Fuel savings per mission resulted well optimized by assuming a $\pm 5°$ excursion for the angle β throughout the entire flight path.

These geometrical parameters were used as input for the definition of the structural concept enabling the transition from the baseline trailing edge configuration to the morphed one. The structural sizing of the concept was addressed while considering the effective operative loads expected in service and the applicable airworthiness requirements; due to the higher complexity of the system with respect to conventional solutions based on hinged flaps, it was believed necessary to take in account aeroelastic issues since the preliminary design phase of the device. To this aim trade off flutter analyses were performed in compliance with CS-25 airworthiness requirements in order to define safety ranges for trailing edge inertial and stiffness distributions as well as for the harmonics of trailing edge's control lines. Reliable aeroelastic models and advanced computational strategies were properly implemented to enable fast flutter analyses covering several configuration cases in terms of structural system failures at A/C level.

Nevertheless, for the economy of the project, detailed design activities were carried out with reference to the installation on wind tunnel demonstrator only.

The wind tunnel demonstrator replicated the last eight bays of the wing in full-scale size; the morphing trailing edge layout pertinent to the outer wing segment of the reference aircraft was then simply relocated along the wing span and supposed to be installed in the region usually occupied by the aileron, thus keeping its overall dimensions unchanged with respect to real aircraft installation.

Numerical and experimental tests were performed using suitable tools and commercial software in order to deeply characterize the mechanical properties of the ATE and assess the goodness of the assumptions and the affordability of the models used in the design phase.

Finally, the manufactured demonstrators were scanned by means of optimized photogrammetric techniques suitably set up for the purposes of dimensional checking and functionality verification of the ATED, performed both statically and in simulated operative conditions in wind tunnel test activities.

REFERENCES

[1] Pecora, R., Magnifico, M., Amoroso, F., Lecce, L., Bellucci, M., Dimino, I., Concilio, A. and Ciminello, M., SARISTU - Smart Intelligent Aircraft Structures, chapter 2.2 "Structural Design of an Adaptive Wing Trailing Edge for Large Aeroplanes", Woelcken, P.C. and Papadopoulos, M. editors, Springer International Publishing AG, Switzerland, 2015.

[2] Barbarino, S., Bilgen, O., Ajaj, R.M., Friswell, M.I., Inman D.J., "A Review of Morphing Aircraft", Journal of Intelligent Material Systems and Structures, Vol. 22, 2011, pp. 823 -877.

[3] Monner, H. P., Bein, T., Hanselka, H., and Breitbach, E., "Design Aspects of the Adaptive Wing -The Elastic Trailing Edge and the Local Spoiler Bump", Proceedings of Royal Aeronautical Society Symposium on Multidisciplinary Design and Optimization, Royal Society Publishing, London, 1998, pp. 15.1–15.9.

[4] Pecora, R., Barbarino, S., Concilio, A., Lecce, L., and Russo, S., "Design and Functional Test of a Morphing High-Lift Device for a Regional Aircraft", Journal of Intelligent Material Systems and Structures, Vol. 22, No. 10, 2011, pp. 1005–1023.

[5] Pecora, R., Amoroso, F., and Lecce, L., "Effectiveness of Wing Twist Morphing in Roll Control", Journal of Aircraft, Vol. 49, issue 6,2012, pp. 1666-1674.

[6] Barbarino, S., Pecora, R., Lecce, L., Concilio, A., Ameduri, S., and De Rosa, L., "Airfoil Structural Morphing Based on S.M.A. Actuator Series: Numerical and Experimental Results", Journal of Intelligent Material Systems and Structures, Vol. 22, 2011, pp. 987–1004.

[7] Ameduri, S., Concilio, A., Pecora, R., "A SMA-based morphing flap: conceptual and advanced design", Smart Structures and Sytems,Vol. 16, No. 3, 2015.

[8] Browman, J., Sanders, B., and Weisshaar, T., "Evaluating the Impact of Morphing Technologies on Aircraft Performance", Proceedings of the Forty-Third AIAA Conference on Structures, Structural Dynamics and Materials, AIAA Paper 2002-1631, April 2002.

[9] Amendola, G., Dimino, I, Concilio, A., Pecora, R., Amoroso, F., "Actuation System Design for a Morphing Aileron", Applied Mechanics and Materials, Vol. 798, 2015, pp. 582-588.

[10] Munday, D., and Jacob, J., "Active Control of Separation on a Wing with Conformal Camber", Proceedings of the Thirty-Ninth AIAA Aerospace Science Meeting and Exhibit, AIAA Paper 2001-293, January 2001.

[11] Perkins, D. A., Reed, J. L., and Havens, E., "Morphing Wing Structures for Loitering Air Vehicles", Proceedings of the Forty-Fifth AIAA Conference on Structures, Structural Dynamics and Materials, AIAA Paper 2004-1888, April 2004.

[12] Blondeau, J., and Pines, D., "Pneumatic Morphing Aspect Ratio Wing", Proceedings of the Forty-Fifth AIAA Conference on Structures, Structural Dynamics and Materials, AIAA Paper 2004-1808, April 2004.

[13] www.saristu.eu (web site of the SARISTU project)

[14] Dimino, I., Flauto, D., Diodati, G., Concilio, A., Pecora, R., "Actuation system design for a morphing wing trailing edge", Recent Patents on Mechanical Engineering, Vol. 7, Issue 2, 2014, pp. 138-148.

[15] Schorsch, O., Luhring, A., Nagel, C., Pecora, R., Dimino, I., "Polymer based morphing skin for adaptive wings", 7th ECCOMAS Thematic Conference on Smart Structures and Materials SMART 2015, Azores (Portugal) 3-6 June, 2015.

[16] Bruhn, E. F., Analysis & Design of Flight Vehicle Structures, chapter A19, Tri-State Offset Company, Cincinnati, OH, 1969.

[17] Pecora, R., Concilio, A., Dimino, I., Amoroso, F., Ciminello, M., "Structuraò design of an adaptive wing trailing edge for enhanced cruise performances", 24th AIAA/AHS Adaptive Structures Conference, AIAA SciTech, San Diego(CA) 4-8 January 2106 (paper ID: AIAA 2016-1317).

[18] MSC-MD NASTRAN®, Software Package, Ver. R1-2012, MSC Software Corporation, Santa Ana, CA, 2012.

[19] Pecora, R., Magnifico, M., Amoroso, F., Monaco, E., "Multi-parametric flutter analysis of a morphing wing trailing edge", Aeronautical Journal, Vol. 118, Issue 1207, 2014, pp. 1063-1078.

[20] Broadbent, E. G., Flutter and Response Calculations in Practice, AGARD Manual on Aeroelasticity, Vol. 3, NASA, February 1963.

[21] A_DEU_121_1_R2 – Reference baseline wing and morphing wing aeromechanical requirements

[22] D22.1 – Reference Aerodynamics of Standard Trailing Edge

[23] FEM of the LH wing, MSC-NASTRAN® bulk data file, SARISTU_wing_REV.03.dat 29/05/2012

[24] D22.4 – Actuator System Design: Integrated actuator system for Trailing Edge morphing

[25] D22.3 – Skin concepts for conformally morphing Trailing Edge

[26] D41.1 – Monitoring system specifications

[27] European Aviation Safety Agency, Certification Specifications and Acceptable Means of Compliance for Large Aeroplanes – CS-25, Amendment 11, July 2011.

[28] Verrastro M, Metge S., SARISTU - Smart Intelligent Aircraft Structures, chapter 1.2 "Morphing Wing Integrated Safety Approach and Results" ", Woelcken, P.C. and Papadopoulos, M. editors, Springer International Publishing AG, Switzerland, 2015.